TRANSPORT AND DEPOSITION OF NANOPARTICLES IN MICROVASCULAR NETWORKS

by

HASSAN MUDHAFAR AL-SIRAJ

A dissertation submitted to the

School of Graduate Studies

Rutgers, The State University of New Jersey

In partial fulfillment of the requirements

For the degree of

Doctor of Philosophy

Graduate Program in Mechanical and Aerospace Engineering

Written under the direction of

Dr. Prosenjit Bagchi

And approved by

_____

_____

_____

_____

New Brunswick, New Jersey

January, 2019

ABSTRACT OF THE DISSERTATION

Transport and Deposition of Nanoparticles in Microvascular Networks

By HASSAN MUDHAFAR AL-SIRAJ

Dissertation Director:

Dr. Prosenjit Bagchi

Targeted delivery of therapeutic drugs to specific sites in the body is becoming a norm for treating many diseases, such as cancer. Engineered nanoparticles have emerged as the most suitable carriers for this purpose. Often times, these particles are directly injected into the bloodstream and carried by the circulation to the targeted sites. The efficiency of the nanoparticle delivery depends on how many of them eventually reach the target sites before being removed by kidney filtration or by phagocytosis. Two hydrodynamic processes that are critical in the efficient delivery are margination of these particles from the core of a blood vessel towards the vessel wall, and adhesion of the particles on to the endothelial cell surface lining the vessel wall. Previous studies have considered

margination and adhesion of nanoparticles in simple geometry, such as parallel plate flow chambers, and bifurcating channels. These studies have shown that the particle size and shape significantly affect their margination. However, blood vessels in the microcirculation form complex networks known as microvascular networks that are characterized by highly tortuous vessels, and frequent and hierarchical bifurcations and mergers. A detailed quantitative analysis of particle margination and adhesion under such complex geometry is missing. Towards that end, in this thesis we utilize a high-fidelity computational model of cellular-scale blood flow in physiologically-realistic microvascular networks to study the margination and adhesion of nano- and micro-particles. The objective is to understand the simultaneous effects of the flowing red blood cells and the complex geometry of the vasculatures on the margination and adhesion of particles. In the first part of the work, we model nanoparticles as volume-less point particles that are simply advected by the streamlines. We find that margination and adhesion are highly non-uniform across the networks. Specifically, we find that adhesion is significantly high in the bifurcation regions, while margination is high in the venular segments. In the second part of this work, we modeled particles as rigid finite-size spheres. Similar heterogeneity is observed herein, and the margination area density is also correlated to the CFL thickness. Arterioles and venules have high levels of margination and adhesion likelihood, while capillaries have the lowest. Our simulations show that irrespective of hematocrit levels and network topology, the accumulation of the marginated particles and the likelihood of adhesion increase with increasing particle size. In the last part of this work, we study shape effect of particles by considering oblate and prolate shapes. Similar heterogeneity is observed, and the margination area density is also

correlated to the CFL thickness. Irrespective of hematocrit levels and network topology, margination of ellipsoidal particles was observed to be higher, with the oblate particles showing the maximum margination compared to other shapes. Our work underscores the importance of network topology on the distribution of the therapeutic drug within the targeted tissue.

Acknowledgments

Praise is to Allah for everything.

Sincere gratitude to my father, mother, and all my big family members for their invaluable support, prayer, and encouragement during the journey of my work.

Also, I would like to set special gratitude to my wife, Zaynab Ayad for her support, emotions, and endurance through these challenging times.

Special thanks and appreciation to my advisor Dr. Prosenjit Bagchi for his invaluable and generous efforts in supervision and support.

The story of my time in this study should not end without mentioning some unforgettable names. Dr. Ayad Al-Dabbagh, Omer Thanoon, Omar Alabdlkareem, Arab Hammadi, Mustafa Mozael, Dr. Peter Balogh, Dr. Omer Hamdoon, and all friends.

Thanks also to all kinds of support and funding for the Ministry of Higher Education and Scientific research of Iraq, the Iraqi Cultural Office in Washington D.C., and the University of Mosul.

Hassan M. Al-Siraj

Mechanical and Aerospace Engineering

Rutgers, The State University of New Jersey

December 01, 2018

Table of Contents

List of Tables

List of Illustrations

Chapter 1

Nanoparticles as Drug Carriers

1.1 Introduction

1.1.1 Nanoparticles as drug carriers

Drug delivery is the science of nanometer-scale complex systems built from at least two constituents. One of these constituents is a pharmaceutically active ingredient forming the shell of such systems, and the other is the drug inside this shell, figure 1.1. These systems are sometimes called smart drugs, Nano-carriers (NCs), or drug delivery systems (DDSs). The task of NCs is to transport the therapeutic drug to the disease sites in the most efficient way. More specifically, the primary goals of research in this field are [1-3]:

- Reduction in the harmful effect of the drug to non-target normal organs while maintaining therapeutic effects to the disease locations. This is done by covering the surface of these NCs with specific targeting ligands. Cancer is a significant disease requiring this goal for drug delivery [4].
- Biocompatibility with the disease sites to reduce harmful effects on body tissue.
- Controllability of drug release over time of these NCs to the targeted sites.

Four steps need to be done by these carrier systems in order to complete their functions efficiently: (1) design these systems, (2) delivery of the drug carriers to the blood, (3) adhesion of these nanoparticles (NPs) at the targeted sites, and (4) endocytosis and

exocytosis of the NPs [5]. Through these steps, several challenges arise in microfluidics, microphysics/chemistry, microfabrication, bio-sensing, actuation, and control fields, and these challenges have to be met. Some of the relevant challenges are [3]:

- Lack of accurate characterization of hydrodynamics.
- Insufficient characterizing of nanoparticle-cell membrane interaction and its influence on particle motion.
- The uptake of NCs by physicochemical barriers, and their loss while they are in transit for drug delivery.
- Complexity of targeting environment especially in vivo.

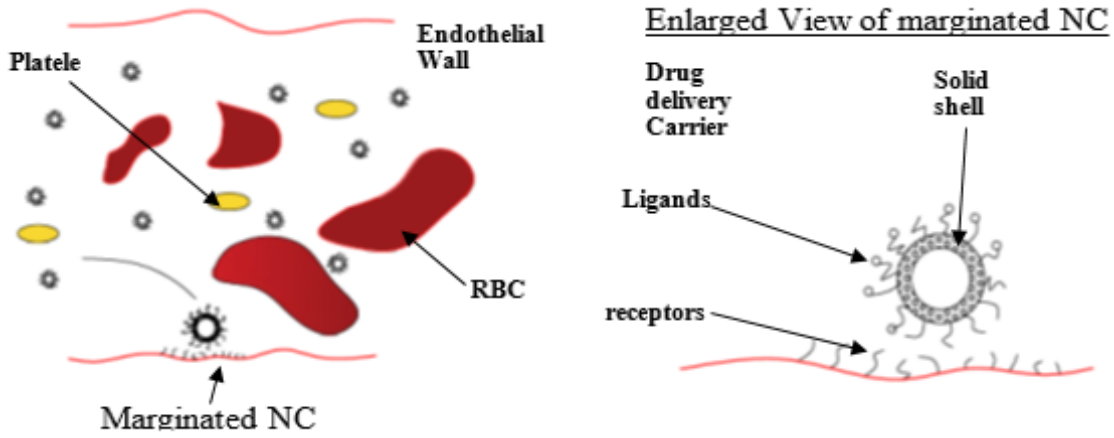

Figure 1.1: Schematic views of various drug delivery systems as given in [6].

1.1.2 Types of NCs used in drug delivery

Several generations of these NCs have appeared during their development. The first generation of the NCs was developed with essential surface characteristics (charge and/or ligands) and with controlled toxicity and biocompatibility. However, there is no control over the targeting process of the NCs to the disease sites, and they can be uptaken by the

immune cells while circulating with the blood. This drawback was overcome in the second generation, where polymer chains are added to their surface to improve the water solubility and compatibility with the immune system. On the other hand, biological barriers still lower the targeting efficiency of NPs to the disease locations. This leads to the third generation, where NCs are improved to have longer circulation time, functionality to meet the above goals, and site-specific delivery. Table 1.1 summarizes some of the used NCs. The efficiency of site-specific targeting of these DDSs is improved by modifying the size, shape, stiffness, and density of the 1st and 2nd generation particles and giving them specific surface characteristics [7-9].

Table 1.1: Definitions of various drug delivery carriers.

#	Composition	Size, Shape, Rigidity
1	**Liposomes:** Spherical vesicles shells of single or multiple concentric bilayer membranes composed of natural or synthetic lipids enclose aqueous core [10].	10s nm – micrometers, sphere, deformable
2	**Polymeric Nanoparticles:** These are copolymers configured from a core and shell in an aqueous environment. The shell consists of hydrophilic blocks to stabilize the core which consists of hydrophobic blocks to minimize their exposure to aqueous surroundings. Therapeutics are placed on the core side [6, 10, 11].	20~400 nm, capsules, and spheres, cylinders, rigid and deformable
3	**Dendrimers:** These are the smallest of NCs and represent polymer chains bifurcating at regular branching intervals to provide fast spreading in the number of end groups with increasing molecular mass. They tend to have a spherical shape that provides dendrimers with minimum viscosity, as compared to linear polymers of the same molecular weight [12].	1.1 – 12.4 nm, sphere
4	**Inorganic NPs:** Encompass a broad range of nanoparticle synthesized from metals, metal oxides, and metal sulfides such as gold, and used for controlled delivery. These types of metal NPs can convert energy into heat at levels up to 70 °C through near-infrared light excitation or oscillating magnetic field [6, 10, 11].	Produced with a plethora of different designs varying in size, shape, and porosity, solid
5	**Biological NPs:** Such as bacteria are unicellular microorganisms that encapsulate hydrophobic, hydrophilic molecules, together with the primary constituents of the cytoplasm [6].	different shapes and sizes (e.g., 400 nm), deformable

1.2 Blood microcirculation

1.2.1 Circulatory system components

The cardiovascular system consists of three parts: the heart, the network of blood vessels, and the blood pumped by the heart to flow into this network.

This vasculature (network) is responsible for distributing the blood to all body organs. Depending on their size, vessels can be classified into five parts: arteries, arterioles, capillaries, venules, and veins, see figure 1.2. Arteries continue to branch to make tubes small enough to be arterioles. The arterioles of small sizes have an average diameter of 5~300 μm, capillaries have smaller diameters than arterioles, and then enlarging to venules which have higher diameters than capillaries [13, 14]. The last arteriole that leads to the capillaries is called meta-/terminal arteriole. In capillaries, red blood cells (RBCs) need to be squeezed to pass through these capillary sizes, which are lower than the typical size of the RBC. Blood is collected into the venules and then back to the veins. It is interesting to mention here that venules are more permeable than arterioles, and even, the smallest venules are more permeable than capillaries. As a result, the transport of gases and other nutrients between blood and tissues is mainly occurred in these venules and capillaries [13, 15].

The roles of the blood are to transport O_2, CO_2, nutrients, proteins, and other materials to the tissue and remove waste from the cells to maintain their normal functions. Blood also transport immune particulates and balances the heat transport inside the body. It constitutes from two main parts, aqueous solution named plasma, and cells. These parts have about 55% and 45% volume fractions of the blood, respectively [14].

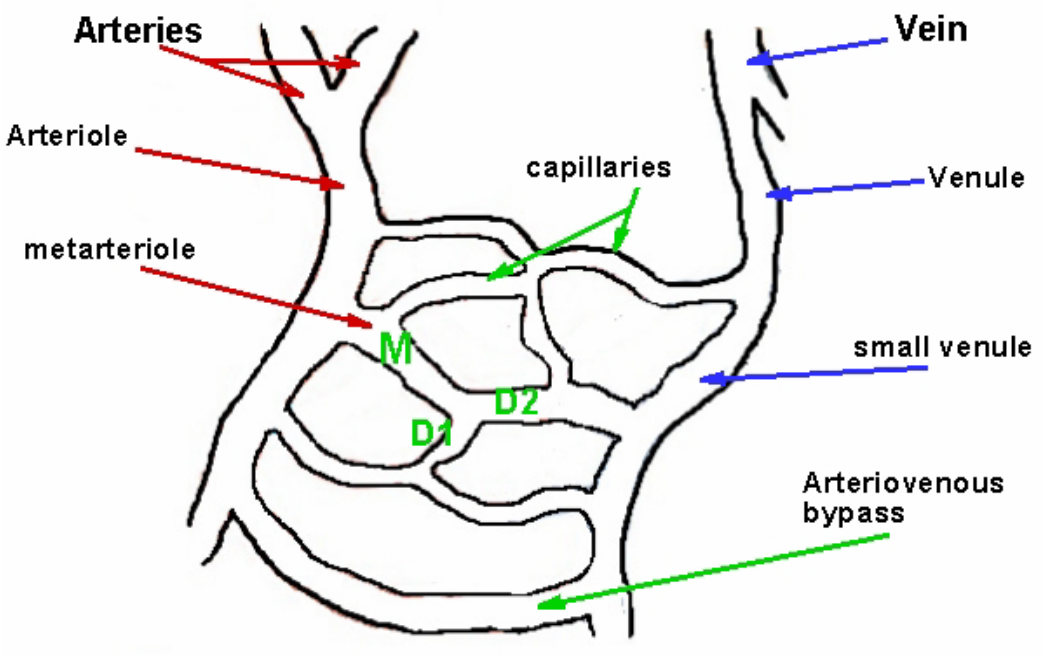

Figure 1.2: Schematic of the microcirculatory system vessels. Figure from reference [16] with modification. Green M-labeled vessel indicated a mother arteriole bifurcating to two daughter vessels D1, and D2.

1.2.2 Blood contents and rheology

1.2.2.1 Plasma

Plasma is the suspending media of the blood, and it consists of 91% water by weight, and 9% of proteins, organic, and inorganic materials. The density of the plasma is 1030 kg/m^3, which is slightly higher than that of water; this excess is due to the existence of proteins and other materials suspended in the plasma. The typical value of the plasma viscosity at 37 °C is 1.2 cP (1.2×10^{-3} $N.s/m^2$.) Diseases and temperature variation lead to change the viscosity of the plasma. It is common to consider the plasma as a Newtonian fluid [16-19].

1.2.2.2 Cellular content of the blood

The cellular content of blood is composed of red blood cells (RBCs) or erythrocytes with around 5×10^6 /mm^3, white blood cells (WBCs) or leucocytes with an average count of 5000 to 8000/mm^3, and platelets which average count of 250,000 to 300,000/mm^3 [18]. In other words, RBCs have 95% of the cellular constituent, while WBCs and platelets have 0.13% and 4.9%, respectively. Because the WBCs and platelets have such low fractions of blood, their effect on the blood microcirculatory and rheology is small compared to the RBCs; however, this is not true for some disease cases. WBCs are rough spherical cells with a diameter ranging from 7 to 22 μm, and they play an essential role in the immune system. Platelets have a diameter range 2~4 μm, and a volume of 5~10 μm^3. Platelets aggregate in the process of clotting and vascular constriction, where they operate to stopping the bleeding. The volume ratio of RBCs out of whole blood is 40~45% and it is referred to as **Hematocrit** (Ht). Due to the dominant fraction of RBCs, their mechanical behavior affects the mechanical properties of the whole blood [16, 17, 19, 20]. In the following, we will present the RBC content and its effect on the microcirculation of the blood flow.

Red blood cell: RBC is a non-nucleated cell which composed of a hemoglobin solution bounded by a thin (~ 0.02 μm thickness) flexible bilayer membrane. This gives the RBC the ability to deform without rupturing the membrane and pass through small capillaries. The shape of the un-deformed RBC is a biconcave discoid which is the equilibrium configuration that minimizes the curvature energy of a closed surface and gives the RBC 40% more surface area of a sphere having the same volume. This excess area helps in the ability of the red blood cell to transport more oxygen. Figure 1.3, shows RBC

configuration. Mechanically, the shear modulus of the red blood cell is equal to 4~10 μN/m. Hemoglobin has a viscosity of 6.0 cP, which is five times higher than the plasma viscosity. The density of the RBC is 1100 kg/m^3 which is slightly higher than the plasma density [13, 14, 19, 21].

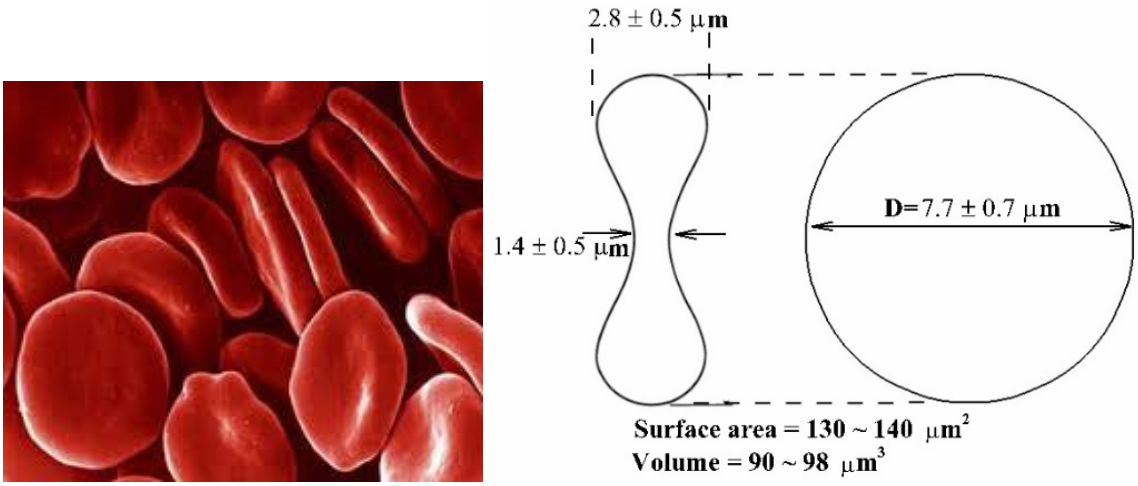

Figure 1.3: Normal RBC configuration.

1.2.3 The viscosity of the blood and the effect of the shear rate

Blood viscosity depends on several parameters; these are, Ht, shear rate, vessel diameter, in addition to temperature. However, under standard conditions of 37 °C, the temperature variation is not significant and does not affect the blood viscosity. The slope of the stress-shear rate curve of the blood is called the **apparent viscosity**. Above a shear rate value of 100 s^{-1}, where RBCs appear individually in the suspension, the apparent viscosity is constant, so that, the blood can be considered Newtonian [13, 14]. However, when the shear rate is lower than the above value, the viscosity increases as long as the shear rate is decreased, and the blood behaves as a non-Newtonian fluid. This behavior of the apparent viscosity with shear rate is called **shear thinning** of the blood [19].

1.2.4 Effect of hematocrit on the apparent viscosity of the blood

Hematocrit has a significant influence on the apparent viscosity of the blood. The viscosity becomes 3 to 4 times more than that of plasma at the normal hematocrit level of 45% [14]. However, the deformability of the RBCs limits the increase of the blood viscosity. This is proved by many researchers who compared the effect of RBC with similar rigid particles and observed a higher increase of viscosity for these particles in the same suspending media [16].

1.2.5 Cell-Free-Layer (CFL)

In the small vessel, RBCs try to move toward the centerline and form a marginal, cell-free layer of plasma. This layer thickness increases with increasing the shear rate [18]. There are two explanations for the existence of this phenomenon. First explanation is that there is a net hydrodynamic force that tends to push the deformable RBCs toward the centerline. The second reasoning states that since the cells are not able to pass through the wall of the vessel, then, the center of red cells must lie at not less than one half of the RBC thickness far from the wall. This means that there will be more RBCs around the vessel core compared to the region near the wall [22].

1.2.6 Plasma skimming

Due to the highly bifurcating nature of the circulatory system, and as a result of the occurrence of the cell-free-layer, another phenomenon exists, namely, **plasma skimming**. In this phenomenon, the peripheral daughter vessel takes most of its flow

from the near wall region of the feeding arteriole, vessel **D1** in figure 1.2, which is a plasma rich location. This results in an uneven distribution of the Ht on the daughter segments (**D1** and **D2**) in figure 1.2 originating from the mother segment **M**.

1.3 NCs characteristics

The modeling of the NCs must cover the essential processes governing their transport such as diffusion, dissolution, erosion, swelling, deformation, and convection. Properties of NCs such as size, shape, stiffness, density, surface chemistry and charge, and composition play an essential role in the above processes [1, 2, 4]. Therefore, there has been an increasing interest in identifying nanoparticle characteristics that are best suited for oncology applications. In this section, we will present some of the relevant works to our interest in this study, which will be the size and shape. We will also present a brief discussion about other mechanical parameters which are stiffness and density of the DDSs.

1.3.1 Size effect

Many studies have demonstrated that NP size is a significant factor which affects its dispersion to, margination, adhesion dynamics near the vessel wall, and its accumulation and distribution efficiency into tumors [4, 10, 23]. Li et al. [24], and Muller et al. [25] used multiscale modeling of flow with RBC in a tube. They found that Large sizes of NPs and micro sizes particles can migrate into the CFL near the endothelium; whereas smaller sizes of NPs probably penetrating the targeted locations . Based on these

observations, a multistage delivery systems are found to have more compatible silicon shell particles those carry nano-sized quantum dots or nanotubes. During the microcirculation, these silicon particles more easily accumulate at the tumor sites. Then, the contents of NCs can be gradually released, diffused, and internalized into the tumor cells.

In general, the size range of drug carrier is from few nanometers to 10 μm; however, according to our best knowledge, the most interesting range for drug carriers in the literature is from 500 nm to 3 μm. This range is decided by many factors such as the targeted location, aim of usage, the material used for fabrication, margination, adhesion, uptake, and other factors that affect targeting efficacy.

One of the experimentally and numerically proved observation, is that increasing the particle size reduces adhesion of all size ranges and increases the margination tendency, especially for the particles > 500 nm. Accordingly, it is recommended to use the smallest possible particles with in vivo imaging and use the most significant possible particles in multistage drug delivery [24, 26, 27]. Lee et al. [28], Li et al. [24], and also Muller et al. [25] made experimental and numerical works on blood flow and found that the dispersion of 1 μm particle is better than that of 100 nm and 200 nm. The smaller NPs localized within the spaces between RBCs. This slows the diffusion of NPs toward the vascular wall, and suggests that smaller NPs may not always be better. Charoenphol and coworkers [29] found with experimentation on flow of RBCs between parallel plates that the level of particle adhesion per unit area on an endothelial cell (EC) decreased when the particle diameter decreased from 10 μm to 0.1 μm. A minimal amount of binding occurred for particles smaller than 2 μm in size. The adhesion densities of 2 μm spheres

are higher than that of 0.5 μm found in simulation by Li et al. [30]; however, this work did not include the effect of RBCs. Moreover, Muller et al. [25] proved this computationally. Müller et al. [31] made numerical 2D, and 3D simulations in tube, and a similar trend of particles between 0.25 μm and 1 μm in a 20 μm in width channel is observed. Simulations demonstrated that the margination is significantly worse for sub-micrometer particles in comparison to larger carriers in agreement with experimental findings.

In the following paragraphs, we try to summarize the effects of specific ranges of spherical particle sizes on dispersion, margination, and adhesion of these particles.

1.3.1.1 Particles of diameter < 100 nm

NPs smaller than 10 nm is removed within the kidney or the tumor [2, 24]. Wang et al. [10] and numerical work by Muller et al. [25] showed that the sub-20-nm particles have rapid permeation into tumors, but they have poor accumulation and rapid clearance through kidneys. Particles of few tens of nanometers (<50 nm) have the advantages of penetrating deep into highly fenestrated tumor tissue in organs like liver, lungs, spleen, and bone marrow [28]. Tullio and coworkers [32] found computationally from 2D channel flow and 3D models of a segment in a network that an increase in shear rate and a decrease in diffusion coefficient are associated with a weak accumulation of particles on the vessel walls with most of the released NCs being redistributed in the blood stream. Also, a decrease in wall filtration velocity is responsible for a reduction in wall accumulation. In the tumor microvasculature, which characterized by low shear rates and higher vessel permeability, the deposition of molecules and small nanoparticles (∼1nm)

is up to 70 % of the total released dose. The analysis of de Tullio et al. [32] of zero Ht shows that as the size of the injected agent increases, the adsorbed dose reduces and falls to about 30 % of the total released dose for nanoparticles of 50 nm in diameter. In Jong and Borm [1], the reason why these NPs (<100 nm) are attractive for medical purposes is based on their unique features; such as their surface to mass ratio, which is much larger than that of other particles. Also, these NPs quantum properties and their ability to adsorb and carry other compounds are other attractive advantages. The analysis in [28] shows that small NPs (<100 nm) tend to localize with RBCs and interact with the vessel walls only in a small fraction. This less frequent interaction and the lower surface of adhesion of small NPs could explain the low enhancement in the observed tumor targeting. In the study of Wang et al. [10], the recommended optimal NP size is approximately 60 nm to 80 nm for the tumor-targeting particles.

1.3.1.2 Particles of size 100 nm ~ 500 nm

Relatively large (> 100 nm) nanoparticles may be needed for carrying a sufficient amount of drug. Also, for drug delivery purposes, not only engineered particles may be used as a carrier, but also the drug itself may be formulated at the nanoscale and function as its own carrier [1]; however, particles larger than 100 nm tend to have low permeation into tumors [10]. As stated in [24], particles < 200 nm still trapped between RBCs in the core region. NPs of 200 nm and higher can be removed by the liver, spleen, or bone marrow. As a general conclusion, particles of 100~500 nm still flow in the core of the domain with the RBCs (mostly co-localized with the RBC rich core), and surprisingly, RBCs prevent them from dispersing [4, 24, 28, 33, 34].

1.3.1.3 Particles of size 0.5 μm ~ 1 μm

The analysis in [28] shows that sub-micron NPs (0.5–1.0 μm) are efficiently pushed laterally by the higher velocity RBCs to localize near the vessel walls so that they can efficiently seek for tumors. When the diameter of NPs is higher than 500 nm, they have pushed away from the core of the blood vessel, due to the tumbling motion of RBCs. Thus, the vast NPs migrate into the CFL and tend to accumulate near the vessel wall. Such margination mechanism large NPs is also followed by WBCs and platelets during circulation [24]. Charoenphol and coworkers [29] showed that the adhesion of sLea-coated spheres is increased as their diameter increased from 0.5 to 10 μm at 200 s^{-1} in the geometry. Workers in [28] concluded that sub-micron NPs should be preferred for vascular targeting in that they would interact more efficiently with the vessel walls seeking for particular disease cells. On the other hand, NPs of a few tens of nanometers and smaller should be used for the direct, passive targeting of diseased tissues of permeable blood vessels. The researchers in [31] found that the margination is significantly worse for submicrometer particles 0.25 μm in comparison to larger carriers 1 μm in agreement with experimental findings. In the experimental portion, fluorescent nanoparticles were tracked in the microvasculature of a mouse with the aid of internal video microscopy and 1 μm particles were found to exhibit margination [4, 28], whereas 200 nm particles were found to distribute randomly in the blood vessel, with no apparent tendency to marginate [28].

1.3.1.4 Particles of size > 1 μm

As the size of the injected agent increases beyond 1μm, the adsorbed dose reduces and falls to about 30 % of the total released dose for nanoparticles of 50 nm in diameter. Note that the portion of the released agent not adsorbed onto the wall is redistributed in the circulation [32]. Experimental observation for flow between parallel plates with the pulsatile flow [29] shows that minimal amount of binding occurred for particles smaller than 2 μm in size. Micro-particles of sizes greater than 2 μm have less margination in capillaries, arterioles, and venules of diameters range 10~50 micron as CFL height is not large enough and the RBCs interaction works to prevent margination [4]. In vivo and in vitro experimentations show that 3 μm spheres marginate more efficiently than 1 μm spheres. A diameter of about 2 to 3 μm would be advantageous for drug carriers [31]. In the work of [35], experimental and numerical findings confirm that the optimal dimension for the best margination is 2~3 μm; this work is done in tube including the RBCs effects. On the other hand, recent experiments [25] suggest that large particles with diameter ≥ 3 μm are subjected to enhanced phagocytosis. A study by Charoenphol et al. [29] on spheres with diameters in the range of 2 to 5 μm displays significant enhancement in margination at intermediate or high wall shear rates than smaller nanometer particles. However, Muller, Fedosov, and Gompper [25] referenced that particles of diameters > 4 μm become captured in the very small capillaries. Muro et al. [36] confirms this also through in vivo work on blood flow.

1.3.2 Shape effect

1.3.2.1 Introduction

There are various shapes used with drug carriers under investigation, see [37]. Many studies try to regulate several characteristics of these carriers and improve their efficacy. The objectives are to regulate cellular uptake, to accumulate in a specific organ, to increase circulation time, to target specific tissues according to their kind and tumor size, see the Blanco et al. [38], and Toy and coworkers [37]. Some of the reviewed studies focused on margination and distribution in the vasculature, while others are interested in their adhesion to endothelial cells and internalization. In the next paragraphs, we will review some of these works.

Recently, varied non-spherical shapes have been getting attention. This is due to the net force and torque formed on these shapes leading them to drift laterally away from the core of the blood flow which enhances their margination [37]. This observation was mentioned in many studies such as the in vivo work of Godin et al. [39]. More specifically, in the review of Sobczynski et al. [4], and theoretical prediction by Lee et al. for shear flow on a wall with zero Ht [40], this drift movement depends on the Stokes number (St), and proportional to the aspect ratio, particle volume, density, shear rate, and buoyancy. In our work, we are interested in the effect of hydrodynamics on particle margination without the inclusion of an external action to help particles margination, e.g., magnetic field. Lee and coworkers [41] showed numerically, for the flow of particles in unidirectional shear flow with Ht=0, that an increase of the Stokes number increases the drifting velocity; however, when the particle is still away from the wall, there is no net drift toward the wall, and the particle is kept oscillating around an equilibrium position.

The work done in [23] concluded that particle rotation encourages the lateral drift which leads to higher margination.

1.3.2.2 Discoidal particles

Discoidal particles and platelets are shown to flow close to the wall mainly due to the hydrodynamic forces rather than collisional forces or volumetric exclusion by the RBCs [40]. Toy and coworkers [37] reported that the drift velocity of the discoidal particles increases with aspect ratio. Several studies have reported the superiority of the disc-like particles over the same volume spherical ones [23, 28, 39, 42]. Carboni et al. [23] mentioned that the critical factor that aids margination of discoidal particles is their rotation. The unique tumbling dynamics improves the closeness to vessel boundaries [38]. The experimental work on the flow inside a tube with Ht = 0 by Gentile and coworkers [43] shows the advantages of discoidal particles over spherical and hemispherical particles in margination and sedimentation at a given shear rate. However, they point that margination efficacy is lowered with shear rate. Experimental work by Decuzzi and his group [27] found that the discoidal particles have more prolonged circulation time and targeting efficiency than spherical counterparts. Also, superiority of these discoidal particles exists even without the use of specific targeting ligands [35]. This superiority is also supported experimentally by [25].

Many studies have reported the superiority of discoidal particles over the equivalent volume spherical one [7, 25, 39, 44]. However, the relationship between the discoidal particle size and adhesion is not monotonic. Adriani and coworkers [45] had found that (1000×400) nm particle is better than (600 × 200) nm and (1800 × 600) nm. The former

experience lower adhesion force to the targeted cells, while the latter experience increased detachment forces.

1.3.2.3 Rod-like shape particles

Several studies have shown that rod-shaped particles also have an advantage over spherical particles [24, 37, 42]. The experimental investigation done by Thompson et al. [46] on blood flow in tubes shows that the margination efficiency is reduced for vessels larger than capillaries. The study in [35] concluded that small discoidal and spherical particles had similar margination probability, while rods significantly had lower probability of margination. This finding is also suported by their in vitro study.

Studies also indicate the advantage of rod-like particles over spherical ones on enhancing adhesion [37, 46]. Similar to the discoid particles, rod-shaped particles with higher aspect ratios have higher adhesion due to both increase of adhesion area and lower drag force experienced at low shear rates [47, 48]. However, at higher shear rates, the drag force depends on the initial adhesion orientation; if the initial contact with the endothelial cells is pointwise, then the drag force will be higher than the adhesion force and detachment happens. On the other hand, if the initial contact with the targeted cell on the wall is along the primary diameter, then the adhesion force will overcome the drag force [23]. What helps the rod-like particles to adhere to the endothelial cells along their long side is their dynamic tumbling motion toward these cells [49].

1.3.2.4 Spheroidal particles

The experimental and numerical work done in [28] suggested using the spheroidal shaped particles to enhance the ligand-receptor interaction with the wall and also the drift toward it. Gentile and coworkers [43] had found that the number of quasi-hemispherical particles is lowered when the shear rate is increased regardless of their size and density. Regarding specific tissue targeting, there is no one conclusion that can be drawn for the superiority of one shape over the other; various tissues have their specific favored shape; see the in vivo study by Venkataraman et al. [50].

1.3.2.5 Ellipsoidal particles

All studies underhand refer to the increase of adhesion when ellipsoidal and non-spherical particles are used instead of spherical shape, and this increase is related to several reasons. One reason is that ellipsoidal particles adjacent to walls have a lower rotational motion which helps them to stabilize and gives them an opportunity to get adhered [25]. Another cause is that ellipsoidal shapes have higher contact surface area with the target surface to adhere than the same volume spherical shape [4, 25, 37]. The increased surface area leads to increased adhesive force between ligand-receptors combination. Another advantage of the ellipsoidal shape over the spherical one is the reduced drag force [25].

It is always shown that the disk-like shape has better adhesion than the rod-like ones. The differences in the drag force and the contact area available for adhesion can partially explained the differences in adhesion. More interestingly, the shape dependent dynamics near the wall has more influence on adhesion; namely, the rotational inertia and the

immediate area available for adhesion. The rotational inertia for disks and rods are 1/16m d^2 and 1/12m L^2 , where m, d, and L are the mass, diameter, and length of the particles, respectively. Then, the rotational inertia of the disks will be lower which reduces the hydrodynamic detachment force. Also, the expected immediate area available for adhesion is higher in the disk. Thus disks are superior in terms of margination and adhesion [45]. However, as in the margination, specific tissue favors specific shape over the other [51].

1.3.3 Rigidity effect

It is worth to mention here that the deformability of the drug carrier has received much less attention compared to the effect of size and shape [30]. Anchordoquy et al. [52] mentioned that deformable particles have longer circulation time than hard particles; however, they have less accumulation in the liver, lungs, and spleen compared to the rigid ones. On the other hand, several studies have shown that deformable particles have a lower margination rate than rigid particles [23, 24, 31]. More specifically, Müller and coworkers [31] showed that at low shear rates deformable particles might have slightly better margination; however, at higher shear rates rigid particles very clearly have better margination. They attributed this behavior to the increase in the deformation of the particles due to increased shear rates, which in turn, elevate the lift force pushing these particles away from the wall. Therefore, they suggested that the deformable particles are better than rigid ones at high hematocrit and low shear rates. The density of the drug delivery particles also has less interest and need more investigation [53].

1.3.4 Particles behavior in bifurcating and merging vessels

Bifurcations disturb flow considerably even without the existence of RBCs, and this enhances the adhesion at these locations. Several studies have shown higher adhesion at bifurcations than any other part of the network [4, 47, 48, 54, 55]. However, most of these studies deal with single bifurcation only. Bächer, Schrack, and Gekle [56] studied the flow of particles and RBCs into a bifurcation or out of a merger. They found that the bifurcation disturbs the flow, but it does not affect the margination distribution that exists in the mother segment before the bifurcation. However, with the merger, the flow behaves differently where the margination distribution in the daughter segments is disturbed. As a result, margination is reduced in the collecting segment. The other finding in this work is the formation of the central CFL after the merger and that many particles are following the streamlines on this layer.

Lamberti et al. [54] have made an in vitro work for active nanoparticle adhesion at the bifurcation. Their findings showed that the adhesion is significantly enhanced at bifurcations. Also, they found that some bifurcation angle ratios cause higher particle adhesion than others. Prabhakarpandian et al. [57] also studied the particle adhesion at bifurcations both in vitro and with CFD modeling. They found that in these locations, the adhesion is very heterogeneous and it is shear rate dependent. More adhesion is observed at the locations of low shear rate.

1.4 Effect of microvascular network complexities on blood hydrodynamics and NCs transport

There are various complexities associated with blood flow in networks which are not seen in simple straight tubes. These complexities result from different topologies of these networks from one organ to another. For example, planar networks exist in muscles, while treelike configurations exist in kidney and retina [58]. Vessels are bifurcating, merging, winding, and even can have trifurcating and short shunts in tumors [59, 60]. Many levels of bifurcations and mergers exist in the arterial side and venular side [61]. Additionally, vessel sizes and lengths vary significantly [62, 63].

Such complexities are reflected on the hemodynamics of blood flow inside these networks and make it vary from simple flow in straight tubes. Some of these variations are the asymmetric profiles of Ht and velocity [64]. Also, blood viscosity considerably varies between in vivo and in vitro measurements [65]. In addition to these differences, the flow can have an oscillations inside these networks [66-70]. Other network related flow phenomena are discussed in section 1.2 like plasma skimming.

The hematocrit distribution in the microvascular network is heterogeneous. This is because the mother arteriole distributes its hematocrit unequally to its daughter capillaries. The topology of the bifurcation may favor one capillary over the other, see figure 1.2 with the mother arteriole (**M**) and two daughters **D1** and **D2**. As such, the vessel **D1** receives higher fraction of RBCs than **D2** [71]. Furthermore, if one daughter vessel gets a higher fraction of blood flow, then it would get an even higher fraction of RBCs [18].

Because of these complexities of microvascular blood flow, the transport and deposition of NPs are expected to be more complicated in the vascular networks than in tubes or channels. There has not been any work that considered flow of NPs in physiologically realistic microvascular networks. The only relevant work is the one by Hossain and coworkers [72, 73] that studied the adhesion of NPs on a patient-specific left coronary artery network. Despite that this flow type differs from the microcirculation, they found that larger particles of 2 μm adhered more in the downstream branches, while smaller particles of 0.1μm adhered more in the mother branch. They concluded that this behavior could help for rational design of NPs for patient-specific delivery.

1.5 Objectives and the scope of the thesis

As stated above, there has been no study on the transport, margination, and adhesion of NPs in blood flow in physiologically realistic microvascular networks. In this thesis we employ a high fidelity 3D numerical modeling to study flow, margination, and adhesion of NPs and micron size particles through in vivo like microvascular networks. Unique feature of our model is that it resolves the 3D deformation and dynamics of every single RBC with high accuracy while simultaneously retaining geometric complexity of the capillary networks. NPs are modeled as tracer particles as well as finite sized particles. The effect of particle shape is also studied. The influence of RBCs and network topology are illustrated. Figure 1.4 summarizes our interest out of the drug delivery process.

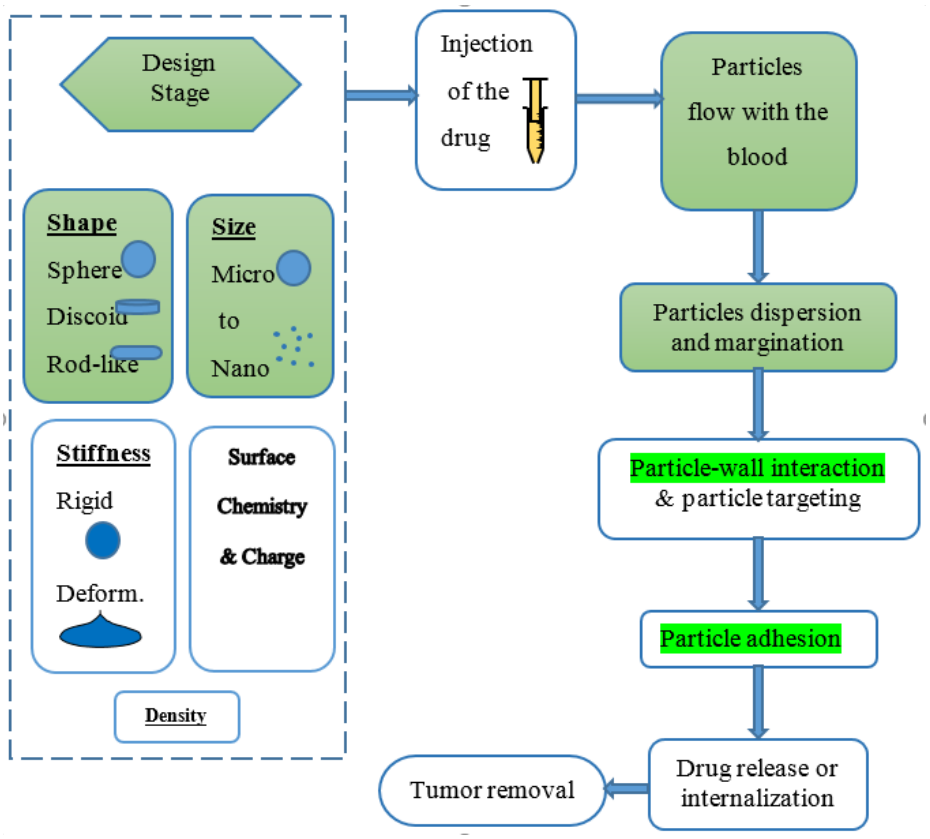

Figure 1.4: Drug delivery stages. Green filled boxes, and highlighted text is included in the current study.

The specific objectives that will be addressed are outlined below for each chapter.

1. **Numerical modeling (Chapter 2):** We employ an accurate and well-validated three-dimensional numerical simulation model for blood flow. This model can be applied in various complex geometries with various boundary conditions. The numerical method is based on immersed boundary method. The rigid vascular walls are treated using sharp interface immersed boundary method, while the deformable cellular interfaces are treated by a continuous forcing immersed boundary method. The cells are modeled as viscous drops surrounded by elastic membrane. A finite element method

is used to compute the membrane stresses. The flow is governed by the Stokes equation is solved by a finite-volume-spectral solver.

2. **Tracer particles margination and adhesion in the microcirculatory networks (Chapter 3):** In this chapter, we will model NPs as tracer particles, and investigate their margination and adhesion in various networks. the following questions will be addressed: is the distribution of marginated and adhered NPs homogeneous across a network? Are there specific locations in a network that are favored by NPs for adhesion and margination? Do margination and adhesion follow the same trend? Are their hydrodynamic parameters that can be correlated with NPs margination and adhesion in the context of an entire vascular network?

3. **Effect of particle size on margination (Chapter 4)**: Then we extend our simulation to consider finite size of NPs. Here we focus our attention on spherical particles only, and vary their size as 500 nm, 1.0 μm, and 2.0 μm. these sizes are chosen because of higher margination rate observed in straight tubes and channels as discussed before. Specifically, we will address how finite sized particles behave differently from tracer particles, or the later can be used to understand the margination and adhesion behaviors of the finite size particle also.

4. **Effect of particle shape on margination (Chapter 5)**: In this chapter, we will consider the shape effect on the particle margination. Ellipsoids are the most commonly used shapes for in vivo applications. Discoidal and prolate shapes are

included in this study to understand how the deviation from the spherical shape affects their margination behavior. The questions raised above will also be addressed here in the context of particle shape.

5. **Conclusion and future work recommendation (Chapter 6):** In this chapter, we will summarize the results of this work. Specifically, the tracer particles, finite-size spherical particles, and finite-size ellipsoidal particles. We also will make our conclusions about how the size of a particle and its shape enhances its margination and adhesion/likelihood mechanisms. Also, we will conclude on how these mechanisms are influenced by the network geometry. Finally, we will discuss on to what extent that the simulations of volume-less tracer particles particle can estimate finite-size spherical and non-spherical particles. In the end, we will make some suggestions for future works.

Chapter 2

Numerical Modeling

2.1 Introduction

As mentioned in chapter 1, most previous studies have considered straight tubes of uniform circular or rectangular cross-sections. No study is available for flow of NPs in blood flow in microvascular networks. We consider the direct numerical simulation of particle transport through physiologically realistic microvascular networks. Four different network configurations are used in this study as shown in figure 2.1. Details of these networks are given in the next section. In our modeling, the high deformation of RBC and complex configurations of vascular networks can be resolved accurately.

2.2 Details of the networks used in this study

Four different microvascular networks are digitally constructed following published in vivo images [74-76], and data [59, 77], as shown in figure 2.1. Starting from the general topology, they range from the most complex topology geometry (A) to the simplest one (D.) All of these networks have the properties of bifurcating, merging, and winding vessels, and there are one inlet and one outlet in each of these networks. In between the inlet and outlet, there are several levels of arterioles which reduce in size before leading to capillaries of the smallest diameters. Then, the blood flows out of these capillaries and

collected into higher diameters venules. Table 2.1 summarizes the characteristics of these networks. The networks vary in terms of the number of segments, and segments length and size. These networks also have significant differences in their total volume and surface area.

Each geometry was built using CAD software, and their surface mesh is generated using the freeware Gmesh [78], see figure 2.2. The suspension of RBCs is then flown inside these boundaries. See [79] for details. Horton's law is used to capture the fractal nature of the topology at bifurcations and mergers [76]. Vessels are rigid with a circular cross-section; however, the cross-section is vessel length dependent.

2.3 Modeling of the RBC

2.3.1 Geometrical modeling

RBC is modeled as a drop enclosed by zero thickness two-dimensional hyper-elastic membrane. When there is no flow, the biconcave resting shape is prescribed as by mapping it from the surface of a sphere [80]:

$$x = R\eta, \quad z = R\zeta, \quad y = \frac{R}{2}\sqrt{1 - r^2}(C_o + C_2 r^2 + C_4 r^4) \tag{2.1}$$

where x, y, z are the coordinates on the RBC surface, while ζ, η are coordinates on the sphere surface. Also, ($r^2 = \eta^2 + \zeta^2$), R is adjusted to control the RBC volume, and the values C_0, C_2 ,C_4, are taken as 0.207, 2.003, and -1.123, respectively. We select the surface area and volume of the RBC to be 134.1 μm^2 and 94.1 μm^3 [18], respectively, see figure 2.3. Then, this surface is discretized by the use of the tools in the GNU triangulation surface (GTS) library [81].

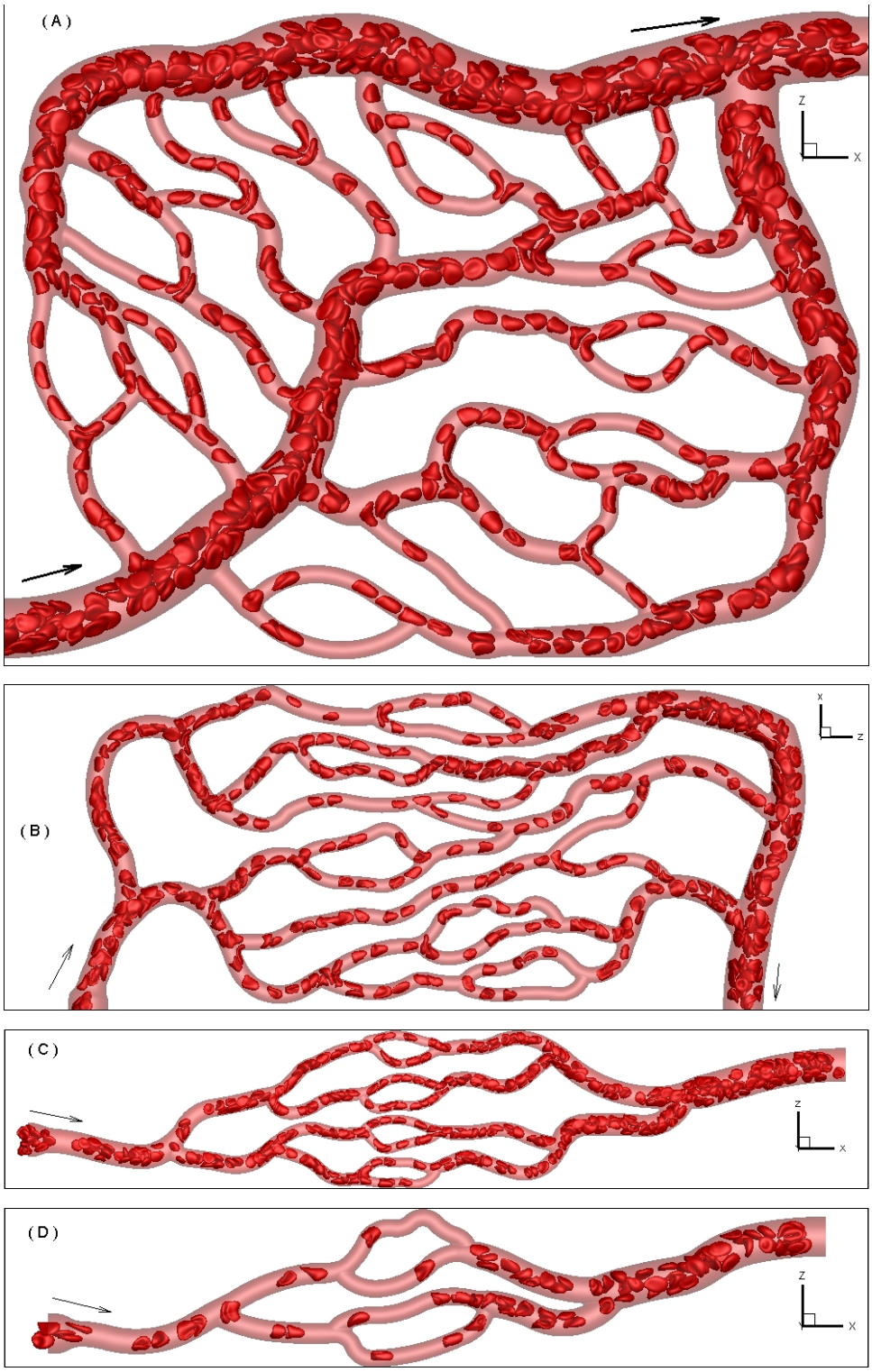

Figure 2.1: Networks used in this work. Arrows show the blood flow direction. The y-direction is along the normal to the page.

Table 2.1: Characteristics of the networks used in this work and presented in figure 2.1.

Property		**Geometry**			
		A	**B**	**C**	**D**
Vessel Diameter (μm)	Maximum	23.0	20.0	21.94	15.75
	Minimum	6.0	6.0	6.5	7.0
Total length (μm)		2976.3	2585.9	1600.7	616.1
Total surface area (μm^2)		93691.4	75923.7	53226.7	18241.6
Total volume (μm^3)		278615.0	200392.6	161470.9	47033.4
Dimensions (μm)	Lx	283.2	165.0	535.3	304.7
	Ly	24.5	22.3	23.4	17.7
	Lz	222.2	385.5	105.6	66.6
Number of branching	Total	50	26	14	6
	Bifurcations	25	13	7	3
	Mergers	25	13	7	3
Number of vessels	Total	76	40	22	10
	Arterioles	25	13	7	3
	Capillaries	26	14	8	4
	Venules	25	13	7	3
Finite Element Mesh	Vertices	1465205	1325505	889683	316154
	Elements	2930038	2651058	1778862	631936
Generation number	Arterioles	12	5	3	2
	Venules	12	5	3	2
	Bifurcations	12	5	3	2
	Mergers	12	5	3	2

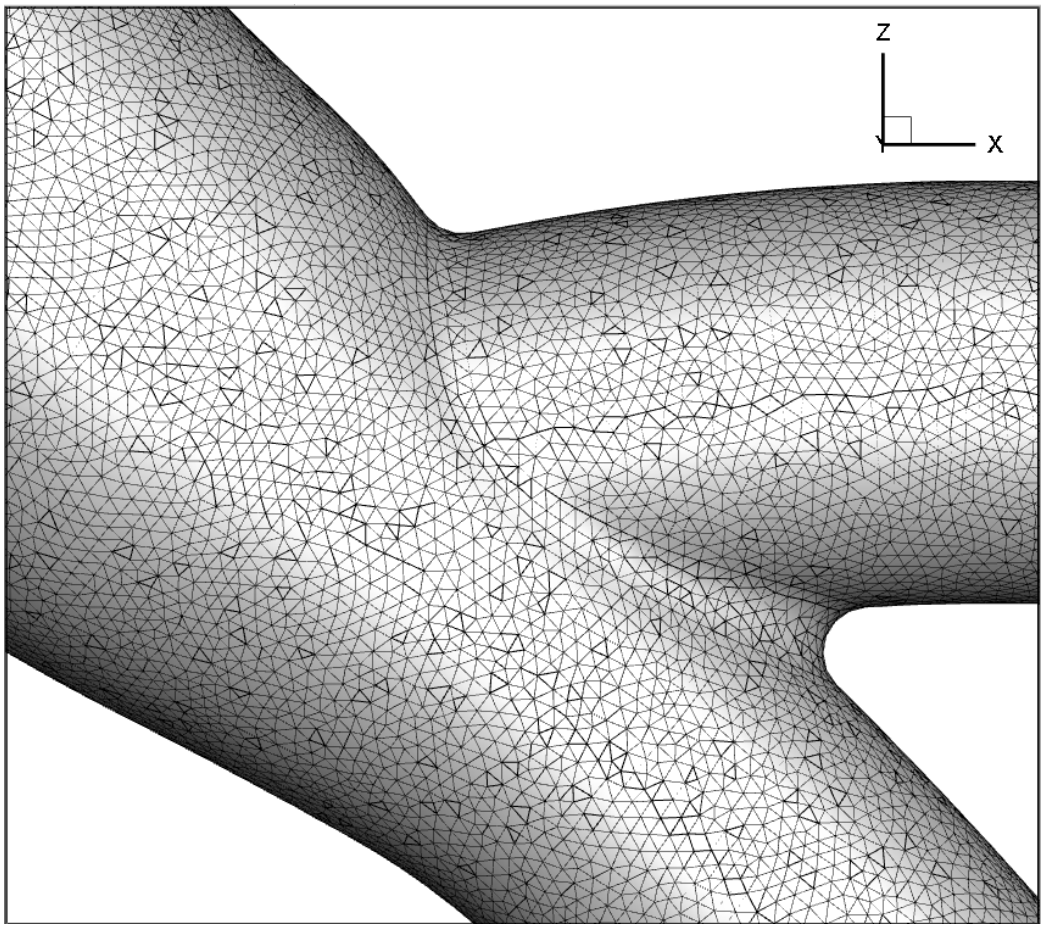

Figure 2.2: Meshed image for the solid boundary of the network.

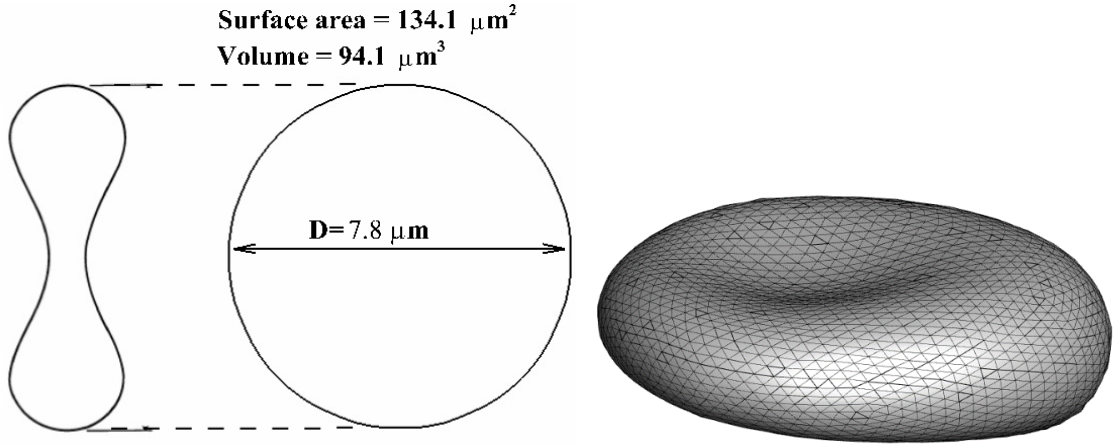

Figure 2.3: RBC model used in this work.

2.3.2 Constitutive laws of the RBC membrane

As stated in chapter one, the viscosity ratio between inside to the outside of the RBC is about 5 [18]. The coupling between RBC membrane and surrounding fluid is obtained through the use of a body force in the Stokes equation. Once this is calculated, it is distributed over the adjacent Eulerian grid region using three-dimensional Dirac delta function. This force $\mathbf{f}(\mathbf{x}')$ in equation (2.18) is calculated for each Lagrangian node (finite element node to be discussed in the next section) on the elastic membrane using the principle of virtual work. The RBC membrane resists against shear deformation, area dilatation, and bending. Skalak [82] developed the following strain energy function for the RBC membrane which includes the shear deformation and area dilatation:

$$W_e = \frac{E_s}{4}\left[\left(\frac{1}{2}I_1^2 + I_1 - + I_2\right) + \frac{C}{2}I_2^2\right] \tag{2.2}$$

Where

$$I_1 = \epsilon_1^2 + \epsilon_2^2 - 2 \tag{2.3}$$

$$I_2 = \epsilon_1^2\,\epsilon_2^2 - 1 \tag{2.4}$$

and ϵ_1 and ϵ_2 are the principal stretches ratios, E_S is the Young surface modulus, and it is equal to:

$$E_S = 2.0\, G_S\, (\, 2 + C\,) / (\, 1 + C\,) \tag{2.5}$$

G_S is the surface shear modulus, and $(C \cdot E_S)$ is the surface area dilatation modulus. To restrict the area dilatation, the value of C is selected to be large enough to reflect the nearly incompressible character of the RBC. The shear modulus is taken as 5×10^{-6} N/m.

The bending resistance is obtained by Helfrich's [83] formulation as:

$$W_b = \frac{E_b}{2}\int_S (2\alpha - c_o)^2 dS + E_g \int_S \alpha_g dS \tag{2.6}$$

Where E_b is the bending modulus associated with the mean curvature α, E_g is the bending modulus associated with the Gaussian curvature α_g, and c_o is the spontaneous curvature which reflects the initial or intrinsic curvature of the membrane. Then, the bending force is obtained as:

$$\mathbf{f}_b = E_b\left[(2\alpha + c_o)\left(2\alpha^2 - 2\alpha_g - c_o\alpha\right) + 2\Delta_{LB}\alpha\right]\mathbf{n} \tag{2.7}$$

Where Δ_{LB} is the Laplace-Beltrami operator, and the bending modulus is taken as 5×10^{-19} J. Note that, we use a high bending modulus as it prevents Lagrangian mesh break down especially when the cell is going through high deformation and squeezing while passing through vessels of sizes lower than the RBC size. This helps to improve numerical stability.

2.3.3 Finite element discretization of the RBC membrane

In the membrane discretization, it is assumed that the triangular elements keep their flatness after deformation. Therefore, the forces acting on the three vertices of the triangular element can be calculated from the displacements of the vertices of the deformed element with respect to its un-deformed state. To do this, rigid body rotation is used to lay the deformed and un-deformed elements into common plane P with local

system coordinates x^P and y^P, and the three vertices are denoted as l, m, and n. Now, the elastic force $\mathbf{f}_e$ is calculated from the principle of virtual work as:

$$\mathbf{f}_e = \frac{\partial W_e}{\partial \mathbf{v}} \tag{2.8}$$

where $\mathbf{v}$ is the vertex displacement. Then, for vertex l, we obtain using the equation of $\mathbf{W}_e$:

$$\mathbf{f}_l^P = \frac{\partial W_e}{\partial \boldsymbol{\epsilon_1}} \frac{\partial \boldsymbol{\epsilon_1}}{\partial \mathbf{v_l}} + \frac{\partial W_e}{\partial \boldsymbol{\epsilon_2}} \frac{\partial \boldsymbol{\epsilon_2}}{\partial \mathbf{v_l}} \tag{2.9}$$

and similarly for other vertices m, and n. The force $\mathbf{f}^P$ is in the common plane and still to be transferred to the global coordinates. It is assumed that the displacement $\mathbf{v}$ is linearly varying within the triangular element as:

$$\mathbf{v} = N_l\, v_l + N_m\, v_m + N_n\, v_n \tag{2.10}$$

Where N's are the following shape functions:

$$N_i = a_i\, x^P + b_i\, y^P + c_i \tag{2.11}$$

Where the index i=l, m, n, and the coefficients (a, b, and c) are found by letting N_i=1 at the specific i-vertex and zero at the other two vertices, this completes the information needed to find the displacement derivatives in equation (2.9).

2.4 Fluid-structure interaction

The fluid motion inside and outside the cells and particles are governed by the continuity and unsteady Stokes equations with variable viscosity:

$$\nabla \cdot \mathbf{u} = 0 \tag{2.12}$$

$$\rho \frac{\partial \mathbf{u}}{\partial t} = -\nabla p + \nabla \cdot \mu \, (\nabla \mathbf{u} + (\nabla \mathbf{u})^{T}) + \mathbf{F} \tag{2.13}$$

where (ρ) is the density of the fluid, (p) is the pressure, ($\mathbf{u}$) is the velocity vector, ($\mathbf{F}$) is the force vector, and (μ) is the viscosity.

The coupling between the fluid flow, the solid boundaries, the membrane of the cells, and particles is done by the immersed boundary method implemented in the framework of finite volume/spectral flow solver. In this method, information is interpolated between the flow field and the membrane [84-86]; the velocity of the flow is interpolated to the membrane to update its new location, and membrane force is interpolated to the flow field and used through the source term in the Stokes equation. The fluid domain is discretized with finite difference method for both fluids inside and outside, so that, one set of equations are being solved by the use of the projection-based method as will be briefly described later.

The viscosity is equal to μ_i for fluid inside the cells and equal to μ_o for fluid outside the cells. The viscosity difference is implemented by the indicator function as:

$$\mu(\mathbf{x}) = \mu_o + (\mu_i - \mu_o)\, I(\mathbf{x}) \tag{2.14}$$

where the indicator function I(**x**) is equal to one inside the cells and zero on the outside. As the cells and particles move and deform, the viscosity in equation (2.14) is updated by solving the following Poisson equation for the indicator function:

$$\nabla^2 \mathrm{I} = \nabla \cdot \mathrm{G} \tag{2.15}$$

where

$$\mathrm{G} = \int_{\mathrm{S}} \delta(\mathbf{x} - \mathbf{x}')\, \mathbf{n}\, \mathrm{d}\mathbf{x} \tag{2.16}$$

and δ is the three-dimensional Dirac-Delta function, **x**′ is a location on the cell/particle membrane (finite element node), **x** is a location in the flow field (Eulerian side), and **n** is the outward unit normal vector on the membrane.

The term **F** is added in the immersed boundary method as a source term, and it is related to the membrane force **f** (**x**′, t) by the following equation:

$$\mathbf{F}(\mathbf{x}, \mathrm{t}) = \int_{\partial \mathrm{S}} \mathbf{f}(\mathbf{x}', \mathrm{t})\ \delta(\mathbf{x} - \mathbf{x}')\, \mathrm{d}\mathbf{x}' \tag{2.17}$$

which in discrete form becomes:

$$\mathbf{F}(\mathbf{x_j}) = \sum_{\mathrm{i}} \mathrm{D}(\mathbf{x_j} - \mathbf{x_i'})\, \mathbf{f}(\mathbf{x_i'}) \tag{2.18}$$

Here, (i) and (j) indices are Lagrangian and Eulerian grid points, respectively. D is the discrete form of the δ function which is constructed from the multiplication of its three-dimensional components as:

$$\mathrm{D}\left(\mathbf{x_j}-\mathbf{x_i'}\right)=\frac{1}{64\,\Delta^3}\prod_{\mathrm{i}=1}^{3}\left[1+\cos\frac{\pi}{2\Delta}\left(\mathbf{x_i}-\mathbf{x_i'}\right)\right]$$

$$\text{for } |\mathbf{x_i}-\mathbf{x_i'}|\le 2\Delta,\mathrm{i}=1,2,3 \qquad (2.19)$$

$$\mathrm{D}\left(\mathbf{x_j}-\mathbf{x_i'}\right)=0 \qquad \text{otherwise}$$

2.5 Interface tracking

The cells and particles are advected based on the Lagrangian method after the flow field is known. The velocity of each membrane node is updated by interpolation as:

$$\mathbf{u_S}(\mathbf{x'},\mathrm{t})=\int_{\mathrm{S}}\mathbf{u}(\mathbf{x},\mathrm{t})\;\delta(\mathbf{x}-\mathbf{x'})\,\mathrm{d}\mathbf{x} \qquad (2.20)$$

Though the summation is over the entire Eulerian nodes, only the local nodes close to the Lagrangian membrane point are considered. Then the Lagrangian points of the membrane are advected by:

$$\frac{d\boldsymbol{x'}}{dt}=\boldsymbol{u}_S(\boldsymbol{x'}) \qquad (2.21)$$

which after discretization with Adams-Bashforth [87] method becomes:

$$\mathbf{x'_{n+1}}=\mathbf{x'_n}+\Delta\mathrm{t}\left[\frac{3}{2}\mathbf{u}(\mathbf{x'_n})-\frac{1}{2}\mathbf{u}(\mathbf{x'_{n-1}})\right] \qquad (2.22)$$

2.6 Flow solver

The domain is discretized using a fixed (Eulerian) rectangular uniform grid, and all of the geometry, cells, and particles are immersed in this domain. The no-slip condition is satisfied on the vascular wall through ghost node immersed boundary method which will be introduced later. The Eulerian mesh size is equal to ($2\pi/120$). while the Lagrangian resolution for the RBC membrane is of 5120 triangular elements. The Lagrangian resolution for particles is varied and will be discussed later.

The flow of empty domain is started until it reaches the steady state; then the RBCs are injected to get to the desired Ht in the main feeding vessel. RBCs are distributed naturally until the flow reaches to the quasi-steady state. Number of RBCs injected in the domain depends on the network volume, and Ht required. We allow sufficient time for cells and particles to flow before starting to collect data for analysis.

An overall pressure difference is supplied at the inlet and outlet sections to drive the flow such that the pressure drop per unit length (μm) is in accordance with the in vivo data [59, 77].

A combined second-order finite-difference scheme is used for the spatial discretization with the staggered distribution of the flow variables. A second-order time-split scheme is used for the time discretization of the Stokes equations. In this method, the momentum equation is split into an advection-diffusion equation (including the body-force) to solve the velocity field and a Poisson equation for the pressure field. Viscous terms are treated semi-implicitly using the second-order Crank-Nicholson scheme. The resulting linear equations are inverted using an ADI (alternating direction implicit) scheme to yield a predicted velocity field. The Poisson equation is then solved to ensure the

incompressibility condition. The Poisson equation is solved implicitly with periodic boundary condition and the use of fast Fourier expansion. Details of the method can be found in [79, 88-92].

After the flow field solution is done, the cells and/ particles are advected. First, the forces on these cells membranes are calculated the under the new velocity, and pressure field and the new location of each membrane node is updated as detailed before. The particles model is then solved to update the position and orientation of these particles.

2.7 Sharp-Interface Immersed Boundary Method for complex geometries

The networks shown in figure 2.1, are developed using CAD software as detailed in [88]. To deal with such complex boundaries, Balogh and Bagchi [88] used a sharp-interface immersed boundary methodology. The basic idea of this method is to enforce a constraint on the ghost nodes (GN), figure 2.4, such that the desired boundary conditions on the vascular walls are satisfied. The boundary points where the conditions are satisfied are called boundary intercepts (BI). An image point (IP) represents the mirror of the ghost node across the boundary. The velocity field at the BI point is the average of those at GN and IP, so that,

$$\mathbf{u}_{GN} = 2.0\ \mathbf{u}_{BI} - \mathbf{u}_{IP} \tag{2.23}$$

Details on this methodology are in [93].

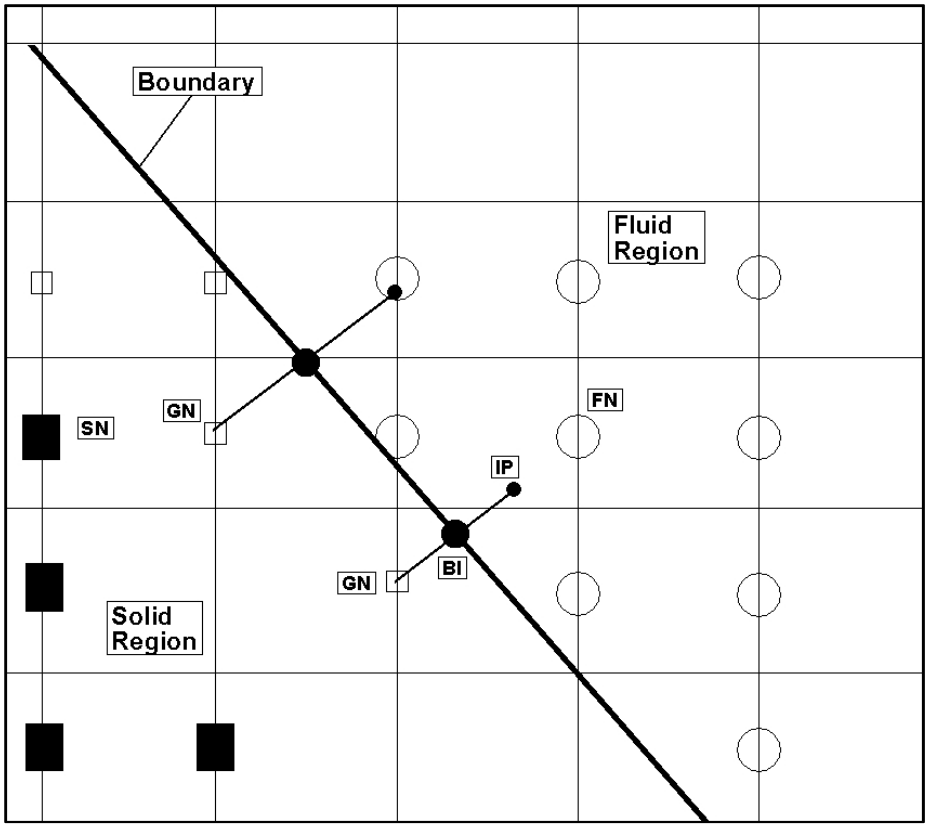

Figure 2.4: Computational stencil (for one velocity component) showing various grid points of the sharp-interface method.

2.8 Modeling of the rigid particle

For a rigid particle of arbitrary shape, the position and orientation are calculated as follows. Forces and torques exerted by the fluid on the particle are calculated after the new flow field is updated [88]. Force is used in Newton's second low to find the location and velocity of the particle, while the torque is used to find the new particle orientation through the law of conservation of angular momentum. The surface of the rigid particle is discretized into triangular finite element mesh, and the fluid stress tensor is calculated for each of these elements from the known velocity and pressure fields of the fluid surrounding each element. The pressure on the specific element is interpolated from the

surrounding fluid grids, while for velocity derivatives used in the viscous stresses, a three-point second order differencing is used, with one of these points being on the surface.

From the calculated net forces on the particle $\mathbf{F}_o$, the translational acceleration of the object is calculated as $\mathbf{a}=\mathbf{F}_o/m$, where m is the mass of the particle. Given the new acceleration, the modified Verlet algorithm [94] is used to find the new position and translational velocity of the particle as:

$$\mathbf{x}_0\,(t+\Delta t) = \mathbf{x}_0\,(\Delta t) + \Delta t\,\mathbf{U}(t) + 0.5\,\mathbf{a}(t)\,\Delta t^2 \tag{2.24}$$

$$\mathbf{U}\,(t+\Delta t) = \mathbf{U}\,(\Delta t) + 0.5\,\Delta t\,[\,\mathbf{a}(t) + \mathbf{a}(t+\Delta t)] \tag{2.25}$$

For the orientation, Euler parameters are used as generalized coordinates to follow the particle orientation with time [95]. The angular momentum is related to exerted torque by:

$$\mathbf{T}_o = d\mathbf{H}/dt \tag{2.26}$$

Given the moment of inertia I_0, the angular velocity is then related to the angular momentum through:

$$\boldsymbol{\omega} = \mathbf{I}_0^{-1} \cdot \mathbf{H} \tag{2.27}$$

A rotation matrix composed of the Euler parameters is used to connect the space-fixed coordinates system defining equation (2.26) and particle local coordinates in which equation (2.27) is defined. Therefore, equation (2.27) becomes:

$$\boldsymbol{\omega} = \mathbf{I}_0^{-1} \cdot (\mathbf{R}_e \cdot \mathbf{H}) \tag{2.28}$$

Then the rotation equation of motion which relates the angular velocities to the rotation of the Eulerian parameters generalized axes is defined as:

$$\begin{bmatrix} \dot{e_0} \\ \dot{e_1} \\ \dot{e_2} \\ \dot{e_3} \end{bmatrix} = \frac{1}{2} \begin{bmatrix} e_0 & -e_1 & -e_2 & -e_3 \\ e_1 & e_0 & -e_3 & e_2 \\ e_2 & e_3 & e_0 & -e_1 \\ e_3 & -e_2 & e_1 & e_0 \end{bmatrix} \begin{bmatrix} 0 \\ \omega_1 \\ \omega_2 \\ \omega_3 \end{bmatrix} \tag{2.29}$$

Then, the new orientation and angular velocities are found using the leap-frog integration algorithm:

$$\mathbf{H}(t) = \mathbf{H}(t - 0.5\Delta t) + 0.5\Delta t\, \mathbf{T_0}(t) \tag{2.30}$$

$$\mathbf{e}(t + 0.5\Delta t) = \mathbf{e}(t) + 0.5\Delta t\, \dot{\mathbf{e}}(t) \tag{2.31}$$

$$\mathbf{H}(t + 0.5\Delta t) = \mathbf{H}(t - 0.5\Delta t) + \Delta t\, \mathbf{T_0}(t) \tag{2.32}$$

$$\boldsymbol{\omega}(t + 0.5\Delta t) = \mathbf{I_0^{-1}}[\mathbf{R_e}(t + 0.5\Delta t)\, \mathbf{H}(t + 0.5\Delta t)] \tag{2.33}$$

$$\mathbf{e}(t + \Delta t) = \mathbf{e}(t) + \Delta t\, \dot{\mathbf{e}}(t + 0.5\Delta t) \tag{2.34}$$

$$\boldsymbol{\omega}(t + \Delta t) = \mathbf{I_0^{-1}}[\mathbf{R_e}(t + \Delta t)\, \mathbf{H}(t + \Delta t)] \tag{2.35}$$

2.9 Comments on computational cost

There are 52 simulations done in total for different networks and different NP characteristics. These simulations are time and data intensive. The time cost of these simulations can reach up to 10 wall clock hours/1 dimensionless time unit in network A where the simulations had performed on processor Intel® Xeon® CPU E5-2689 v4 @ 2.4GHz of 28 CPU(s). The simulations are often run for about 540 dimensionless times. The data from simulations take storage of about 110 TB. In addition, efficient post-processing routines have been developed to deal with these large data.

2.10 Some validations

2.10.1 The effect of the Eulerian resolution on the simulation accuracy

We use the Poiseuille flow in the tube to validate the accuracy of the sharp-interface immersed boundary method used in our modeling, where geometry is not necessarily aligned with the Eulerian grid, see the left side of figure 2.5. The dimensionless tube radius used for the presented data here is equal to 2.8, and this tube is placed in $2\pi^3$ domain. Periodic boundary conditions are applied between the inlet and outlet boundaries. Euler resolution used for the presented tests are 60^3, 90^3, 120^3, 150^3, and 180^3, so as to have a similar grid size in all of the three directions. Figure 2.5 on the right, shows the velocity profiles obtained after the steady-state conditions for selected grid resolutions tests. It is clear that all the resolutions represent the analytical solution very well.

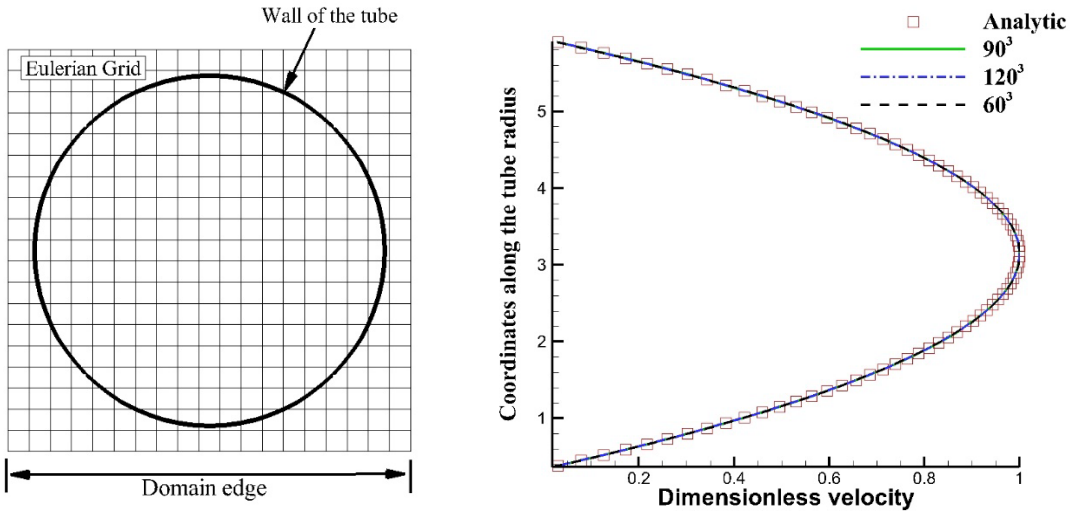

Figure 2.5: Left: side view showing the straight tube boundaries in the Euler grid domain. right: Velocity profile of selected tests of different Eulerian resolution.

The velocity field obtained from the numerical solution is compared with that obtained by analytical solution. Error norms [96, 97] are used to validate the accuracy of the numerical solution velocity field.

$$L_1 = \sum_{n=1}^{N} |dU| \Big/ \sum_{n=1}^{N} U_{analytic} \tag{2.36}$$

$$L_2 = \sqrt{\sum_{n=1}^{N} |dU|^2 \Big/ \sum_{n=1}^{N} U_{analytical}^2} \tag{2.37}$$

$$L_\infty = MAX\,|dU| \tag{2.38}$$

where N is the total number of Eulerian grid nodes, and $dU=U_{analytical} - U_{numerical}$. Figure 2.6 shows the trends of these norms with grid size change. A second-order behavior is observed from these plots where the decrease of the grid size reduces the norm by approximately to half. This behavior confirms the theoretical expected global accuracy of our numerical algorithm.

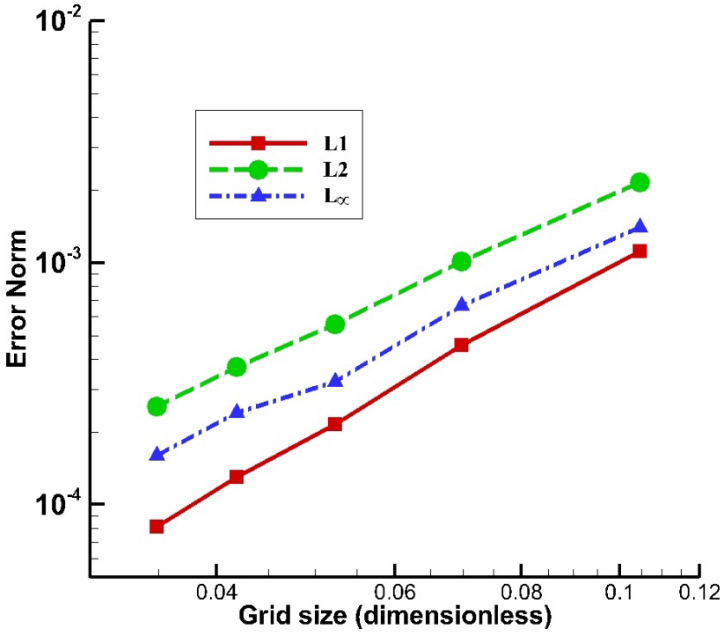

Figure 2.6: Error norms L_1, L_2, L_∞, dependence on the grid size for the current simulation model in Poiseuille flow.

2.10.2 Validation of the non-spherical particle modeling

In this section, we consider the unsteady motion of a rigid oblate particle placed in a shear flow. Solid boundaries are at the minimum and the maximum y-coordinates, and the boundaries in x-direction and z-direction are periodic, figure 2.7. The ratio of the domain edge length to particle equivalent spherical diameter is equal to 2π. The aspect ratio (AR) of the long to short diameters of the particle is chosen to be three, which is the AR used in our simulations as will be discussed in chapter five. The Euler resolution used here is 120^3 which is sufficient as discussed in the previous section. The shear flow is applied according to:

$$u^{\infty} = [\dot{\gamma}y, 0, 0] \tag{2.39}$$

The fluid applies a torque on the particle and makes it tumble. The numerical results are validated by comparing with the Jefferys' analytical solution [98], where the tumbling period is given by:

$$T_{Jeff} = \frac{2\pi}{\dot{\gamma}}\left(AR + \frac{1}{AR}\right) \tag{2.40}$$

and the instantaneous tumbling angle is:

$$\theta_{Jeff} = tan^{-1}[AR \cdot tan(2\pi t/T)] + C \tag{2.41}$$

where C is the constant of integration which depends on the initial orientation of the particle. Five Lagrangian resolutions are used as indicated in figure 2.8. Except for the lowest resolution of 80 triangular elements, all other resolutions show very good agreement with Jefferys' result of instantaneous angular orientation. In the current work, we choose the 1280 element resolution.

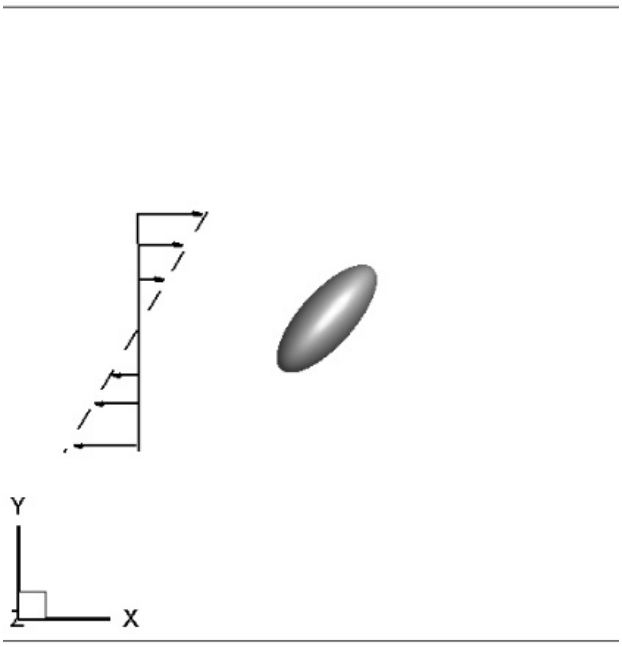

Figure 2.7: Ellipsoidal particle in shear flow.

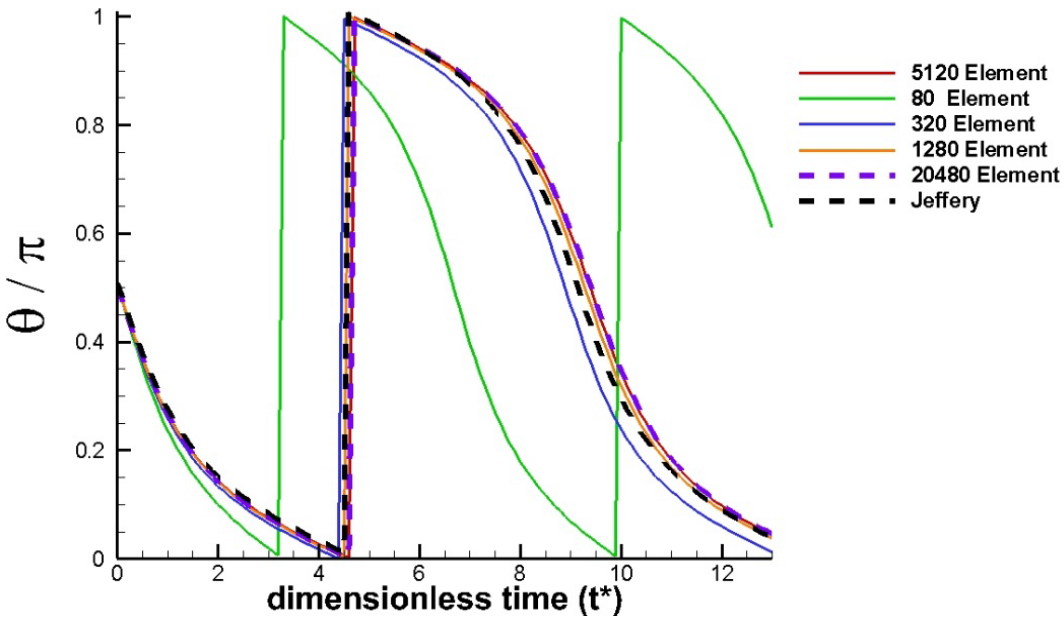

Figure 2.8: Effect of Lagrangian resolution on the instantaneous rotation angle of an ellipsoidal particle (Comparisons with Jeffery's formula).

In figure 2.9, the effect of time step on the accuracy of the rotation angle of the particle is presented. Three time step sizes are investigated as: 0.002, 0.001, and 0.0005. The agreement with the analytical solution is enhanced when time size is reduced. In general, the excellent agreement between numerical and analytical results is observed for all the time step sizes.

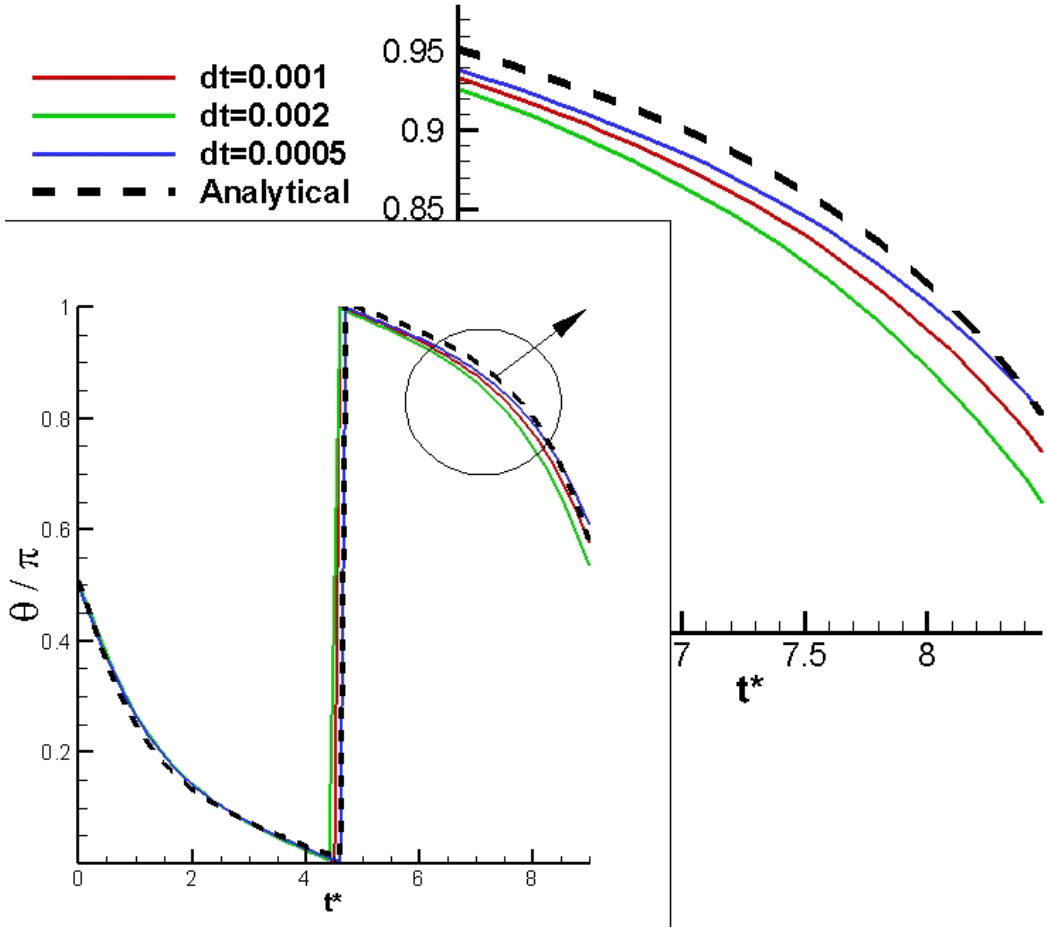

Figure 2.9: Effect of time step size on the behavior of orientation angle of the particle.

Chapter 3

Adhesion and Margination of Nanoparticles Modeled as Passive Tracers

3.1 Introduction

3.1.1 Objectives and justifications

In this chapter, we will simulate and analyze the margination and adhesion of nanoparticles (NPs) modeled as volume-less fluid particles (passive tracers) within blood flow in capillary networks. The objective is to understand the simultaneous role of the geometry of the vasculature and the presence of the red blood cells (RBC) on the margination and adhesion of tracers. The effect of hematocrit is also included in this analysis by varying hematocrit levels as 0%, 10%, and 25%. The passive tracers are modeled as volume-less fluid particles and are simply advected by the fluid flow. They are not assumed to affect the surrounding fluid. Although these are point-particles, in principle they represent nanoparticles of any size less than one Eulerian mesh size used to discretize the fluid domain. As such, these particles have a size of 0.27 μm or less. The justification for modeling such nanoparticles as fluid particles can be obtained by considering some non-dimensional numbers. As already stated before, the flow regime is in Stokes flow ($Re \approx 0$) as capillary networks are considered [99]. Another parameter of

interest is the Stokes number, defined as $St = \rho_p d^2 u/18\mu L$, where ρ_p is particle density, d is particle diameter, μ is fluid viscosity, and u (~ 1mm/s) and L (a few micrometers) are some characteristic velocity and length scales of the fluid. For neutrally buoyant particles of the size range considered, $St \sim 10^{-6}$ so that NPs response time is much faster than fluid response time. Hence NPs can be assumed to be in equilibrium with the fluid, and act like passive tracers advected with the local fluid velocity. Brownian motion of these passive nanoparticles is also not considered. The Peclet number defined as Pe = u L / D, where D can be taken as the NP diffusion coefficient in water (~ 0.2 – 2 $\mu m^2/s$ [100]) is of the order of 10^2 and implies that Brownian effects are small.

3.1.2 Simulation setup

Before advection of fluid particles is started, a quasi-steady solution is first obtained. Then the fluid particles are randomly selected in the plasma. After that, the flow field, RBCs, and the particles are simultaneously evolved in time. The total number of NPs considered varies from 5000 to nearly 30,000 in different networks, but their number density (by volume) is kept constant at 0.1. The instantaneous velocity for the particles is obtained by interpolating the fluid velocity from the surrounding Eulerian nodes using trilinear interpolation. Once the particle velocity is known, each particle is advected using the second-order accurate Adams-Bashforth scheme [87]. In total, there are 12 simulations done for the analyses in this chapter.

3.1.3 Margination and adhesion of the particles

A few comments should be made about margination of the fluid particles. Since they follow fluid streamlines, they would not marginate in a straight tube in the absence of any RBC and Brownian diffusion as there is no lateral movement. When RBCs are present, the particles can marginate by the volume exclusion effect. Also, in the presence of RBCs, the flow becomes unsteady due to RBC-RBC interaction and their dynamics. Then the instantaneous streamlines can come close to the wall of the vessel. However, since streamlines cannot terminate at the wall, the particles following these streamlines could subsequently leave the near-wall region, and they are no longer considered marginated. When the vessels are not simply straight tubes, and repeated bifurcations and mergers are present, flow from a mother vessel is divided in the daughter's vessels and can cause margination of tracers simply by such geometric effects, as will be shown in this study. Following the above, two types of simulations are considered as follows:

Margination simulation: Here particles are advected without adhesion to the vascular wall. A particle is considered *marginated* if it is inside the cell-free layer (CFL) in a vessel. The accurate calculation of the CFL was already described in the previous chapter. It may be noted that in general, the CFL could evolve in time. For the present work, we use time-averaged CFL to evaluate NP margination. Also, the time-averaged CFL varies spatially across the same vasculature, and even over the length of a vessel.

Adhesion simulation: Here a particle is considered *adhered* as soon as it comes within one Eulerian mesh size (~ 270 nm) from the wall. Using this value is justified as the minimum distance between carrier's surface and the wall is controlled by the receptor-ligand interaction distance which can range up to several hundreds of nanometers for tethered molecules, and proteins such as the von Willebrand factor [31].

These two simulations represent two extreme situations when actual drug delivery condition is considered. Once a particle is marginated near the wall, it takes a certain amount of time for it to fully adhere, depending on the rate of bond formation and bond strength. During this process, particles may slowly roll along the vessel wall under the action of bond formation and breakage and the hydrodynamic drag. If the bond formation rate is slow or the bonds are weak, and the vessels are of short length, the particles may not eventually adhere and can leave the near-wall region. The 'margination' simulation corresponds to this situation. On the other hand, if the bond formation rate is very high and bonds are strong, particles may immediately stop as soon as they come within a small distance from the wall. The second set, namely, 'adhesion' simulation, corresponds to this situation of infinitely fast bond formation and strong adhesion.

3.2 Results

3.2.1 The behavior of margination and adhesion of the NCs through various segments of the network

Figures 3.1 to 3.4 present snapshots showing the distribution of RBCs and particles at the end of each simulation. Care must be taken while comparing the results from margination and adhesion simulations. For the margination simulations, figures show the instantaneous particle distribution at the end of the simulations only. As noted before, particles can marginate, but later leave the near-wall region. Therefore, the instantaneous image shows only the particles that are within the CFL at the last instant and not those that were within the CFL at previous times but migrated away from the walls. For the adhesion simulations, on the other hand, the images show total accumulated particles over the entire simulation time.

One important observation from these figures is that the NP distribution is non-uniform across different regions within the same network. This is particularly so for adhesion simulations, where NPs are observed to adhere mostly in the capillary and pre-capillary bifurcations. Many fewer particles adhere in the outlet venules. For margination simulations, on the other hand, relatively higher margination is observed in the venular regions while much less margination is observed in the capillary and pre-capillary bifurcations.

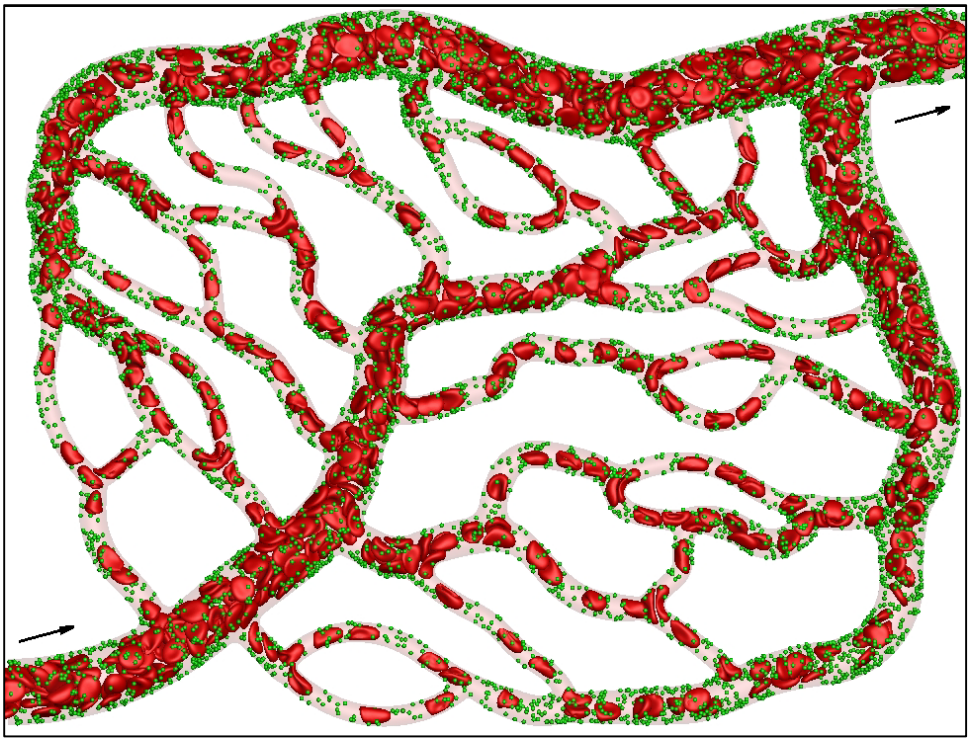

(a) Margination

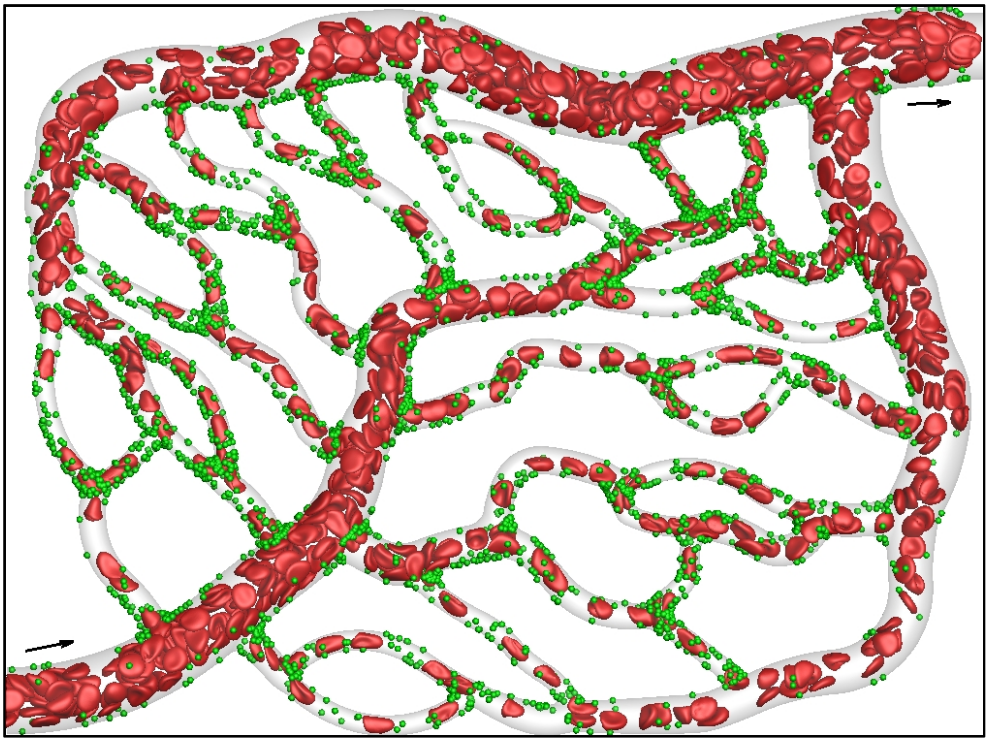

(b) Adhesion

Figure 3.1: Snapshots of the final time instant for (a) margination and (b) adhesion simulations in network A at Ht = 25%. Hereafter NPs are shown in green, and RBCs in red.

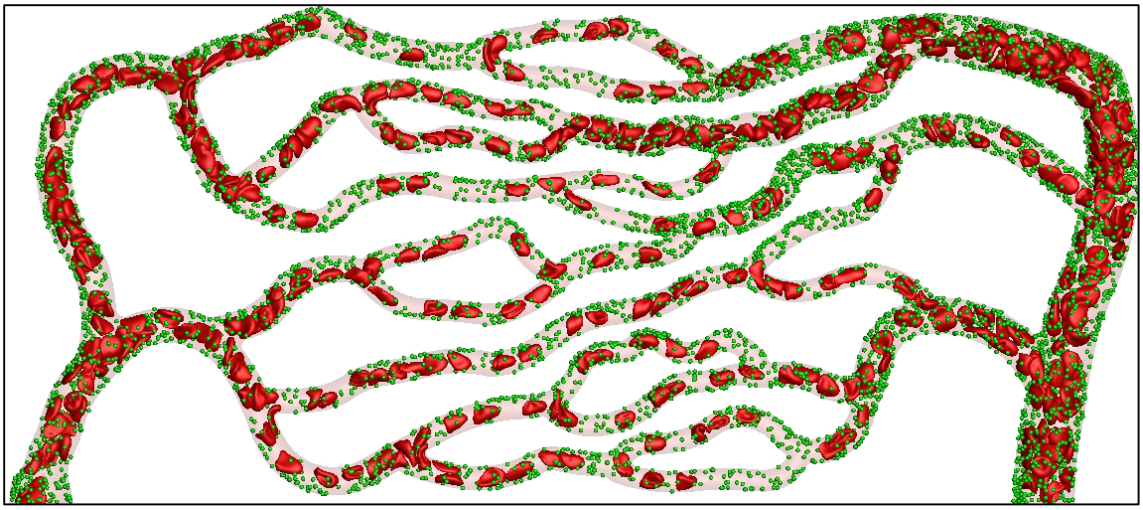

(a) Margination

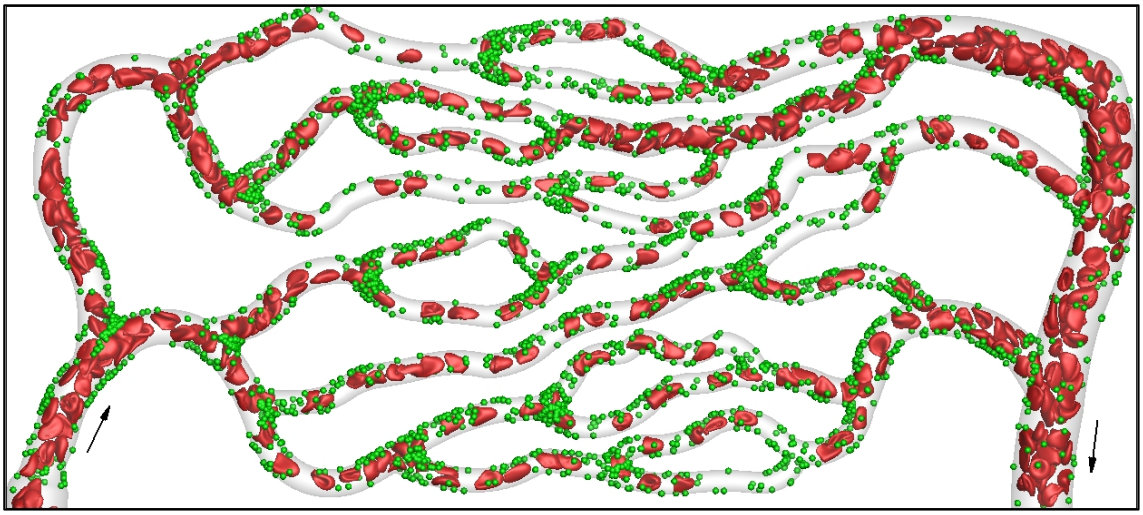

(b) Adhesion

Figure 3.2: Snapshot of the final time instant for nanoparticles margination in network B at Ht = 25%.

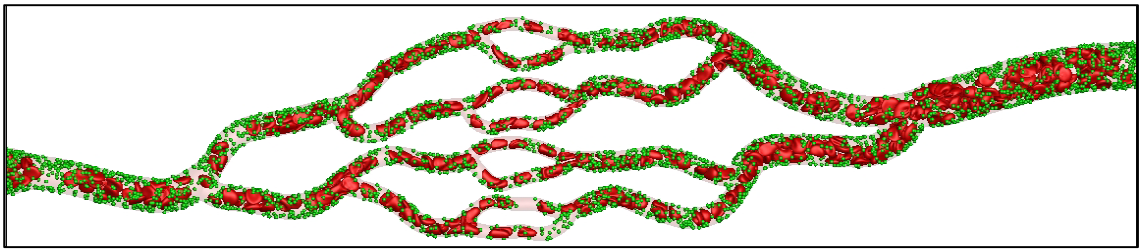

(a) Margination

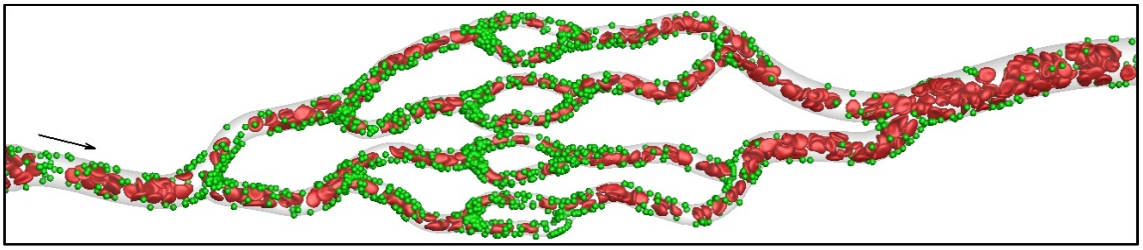

(b) Adhesion

Figure 3.3: Snapshot of the final time instant for nanoparticles margination in network C at Ht = 25%.

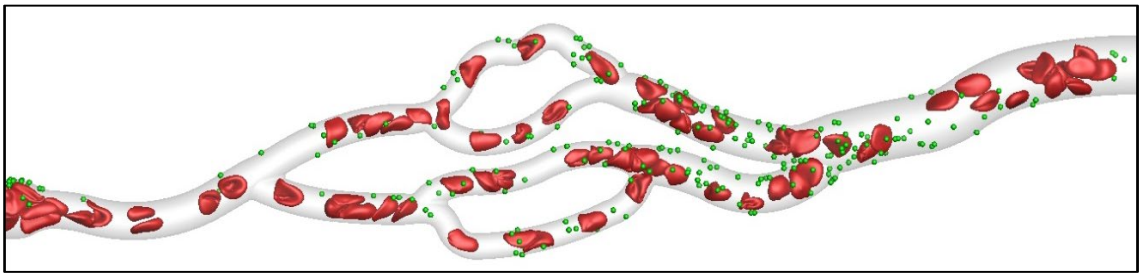

(a) Margination

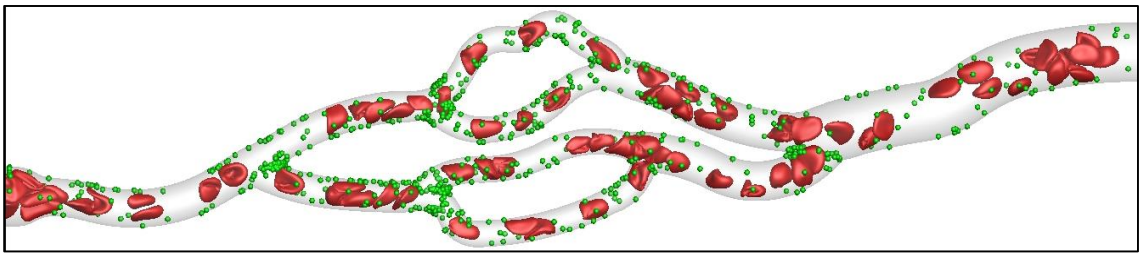

(b) Adhesion

Figure 3.4: Snapshot of the final time instant for nanoparticles margination in network D at Ht = 25%.

Quantitative information on the distribution marginated and adhered particles across the networks is presented in figure 3.5. Here particle distribution is shown in five different segments of the vasculatures, namely, arterioles, capillaries, venules, bifurcations, and mergers. In particular, capillaries are defined as the terminal arteries which do not bifurcate any further. Also, while presenting the data in this figure, we consider two ratios: (i) the ratio of the number of adhered or marginated particles in each segment to that of the total number of particles supplied in the entire vasculature, $\mathbf{N_a/N_s}$ or $\mathbf{N_m/N_s}$, and (ii) the ratio of the number of adhered or marginated particles in each segment to the total number of adhered or marginated particles in the entire networks, $\mathbf{N_a/N_{ta}}$ or $\mathbf{N_m/N_{tm}}$. Note that in this plot, we do not distinguish between different generations of vessels.

The non-uniformity in particle accumulation across each network is readily evident from figure 3.5. The general trends in the data show that for adhered particles, the bifurcation segments exhibit the highest accumulation, while the venular segments exhibit the least. In contrast, for margination simulations, the highest accumulation is in the venular segments, while the least accumulation is either in the bifurcation segments or the capillaries. These general and apparently opposite trends for marginated versus adhered particles are valid for all four vasculatures simulated. Since these networks have different architectures, we conclude that the predicted non-uniformity in particle accumulation would occur in any microvasculature in vivo.

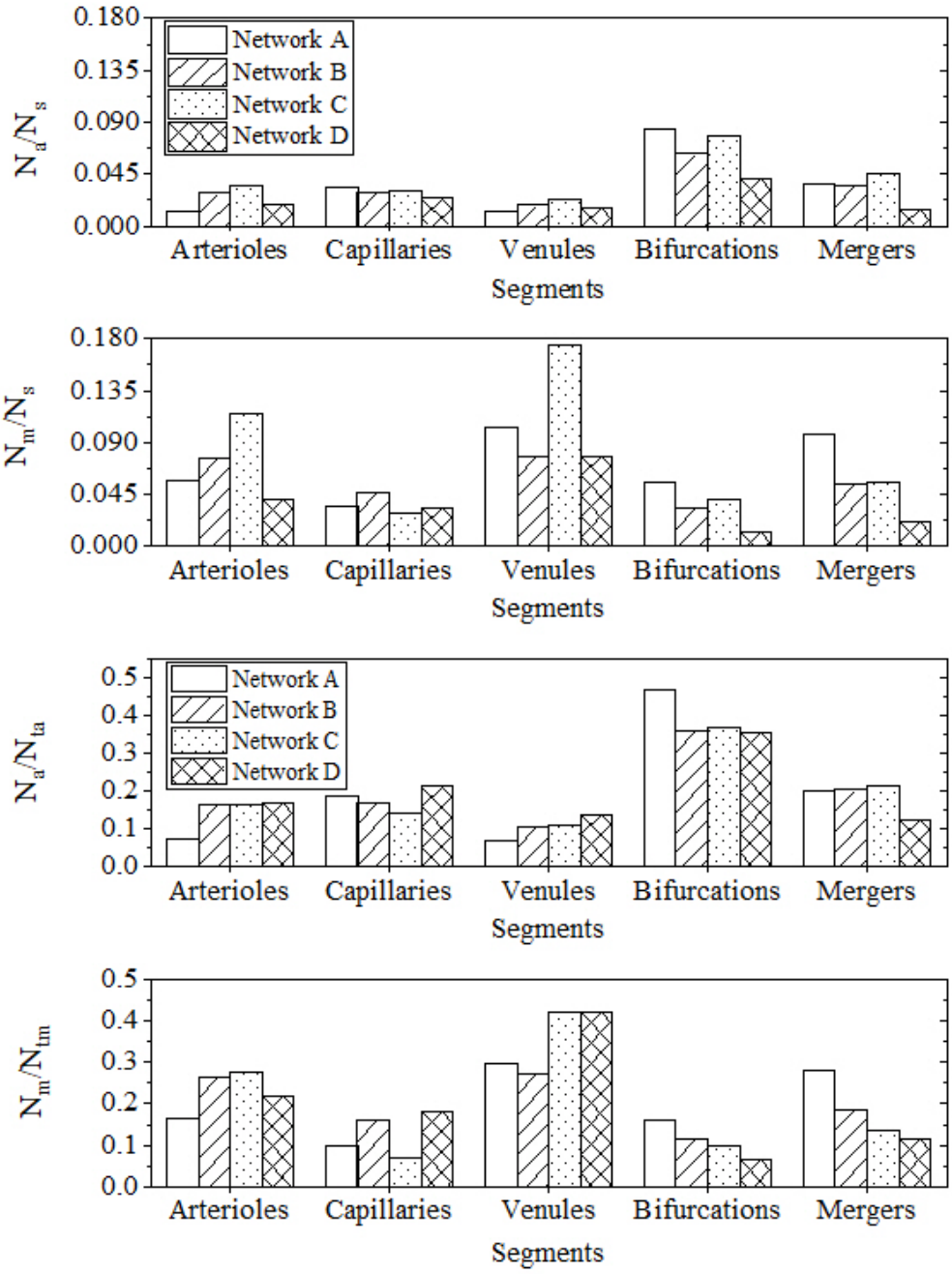

Figure 3.5: NP distribution in different segment groups for Ht = 25%. Top two rows show the ratio of adhered or marginated NPs to the total number of supplied NPs, that is, N_a/N_s or N_m/N_s. Bottom rows show the ratio of the number of adhered or marginated particles in each segment to the total number of adhered or marginated particles in the entire networks, N_a/N_{ta} or N_m/N_{tm}.

In general, different segments of a network, as defined here, have different surface areas. The actual number of particles adhered or marginated will depend on the vessel or segment surface area. In figure 3.6 we scale the number of particles adhered or marginated by the surface area of each segment (i.e., N_a/A_s and N_m/A_s, where A_s is the area of each segment group). For the adhesion simulations, the highest accumulation per area is noted in the bifurcation segments and the lowest in the venule segments. For the margination simulations, the accumulation per area is more uniform, with the capillary segments relatively less margination.

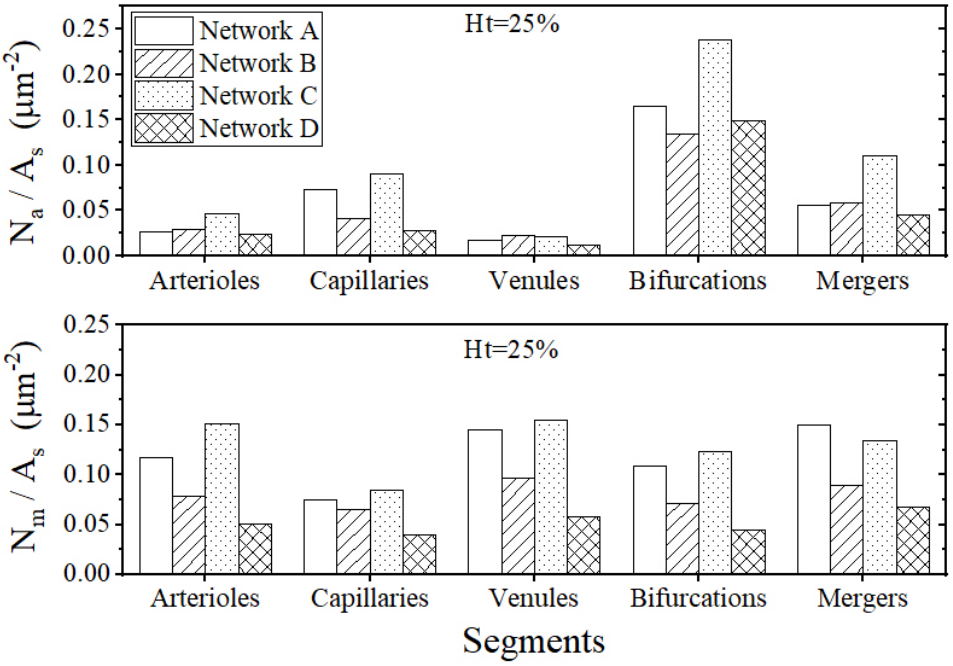

Figure 3.6: NP accumulation per segment area for adhesion (N_a/A_s) and margination (N_m/A_s) simulations for Ht = 25%.

Interestingly, for a specific vascular segment, N_a/N_s or N_m/N_s shows greater variation from one network to another than N_a/N_{ta} or N_m/N_{tm}. This is due to the different vascular surface area for the four networks.

3.2.2 Effect of geometry and Ht on the margination and adhesion of the NCs

We now investigate the reasons behind the observed non-uniform accumulation of NPs. As noted before, NPs in a straight tube are marginated by the action of the RBCs. In contrast, the geometry of the network as characterized by bifurcations, vessel curvature, and mergers, may affect NPs accumulation in a network.

To isolate the influence of the network geometry and that of the RBCs on the NP accumulation, we simulated the flow of NPs in the four networks in the absence of any RBC (Ht = 0), and also with Ht = 10%. The total marginated or adhered NPs as a fraction of supplied NPs (N_{ta}/N_s and N_{tm}/N_s) over an entire network for every four cases and three Ht are shown in figure 3.7. Also shown in figure 3.8 is the total marginated or adhered NPs scaled by the total surface area of an entire network (N_{ta}/A_t and N_{tm}/A_t).

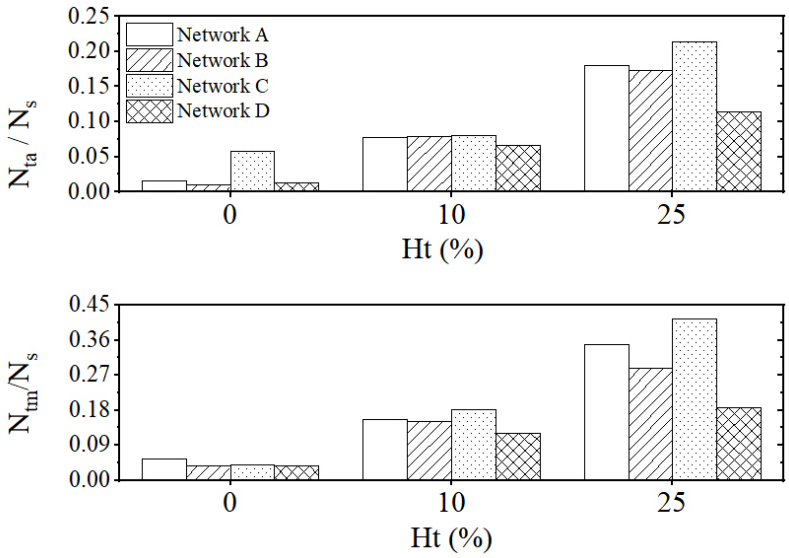

Figure 3.7: Ratio of total adhered or marginated NPs to supplied NPs (N_{ta}/N_s and N_{tm}/N_s) for different Ht = 0, 10, and 25%.

Both figures show that the presence of the RBCs significantly enhances the number of marginated and adhered NPs, although some amount of margination and adhesion is

observed even in the absence of RBCs. Hence, without the presence of the RBCs, the effects of the network geometry alone are significantly weak. On the other hand, this geometry effect is considered an advantage that enhances the margination and adhesion compared to the straight tube configuration.

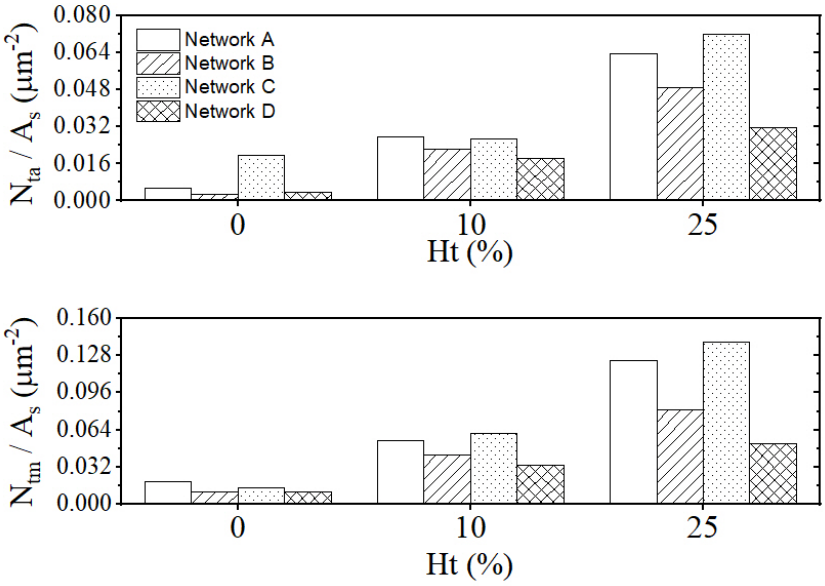

Figure 3.8: Ratio of total adhered or marginated NPs to network surface area (N_{ta}/A_t and N_{tm}/A_t) for different Ht = 0, 10, and 25%.

Nonetheless, we further elaborate the geometry effect in the absence of RBCs by considering the NP distribution in different segments of a network as shown in figure 3.9, where the ratio N_a/N_{ta} and N_m/N_{tm} is plotted for Ht = 0. This figure shows that even in the absence of the RBCs, there is a strong non-uniformity in the distribution of adhered NPs: the highest accumulation is in the bifurcation segments and the least in the venular segments; this is similar to the higher Ht levels adhesion distribution. For the marginated NPs, the distribution is less non-uniform with the capillaries and bifurcating segments being much less favorable.

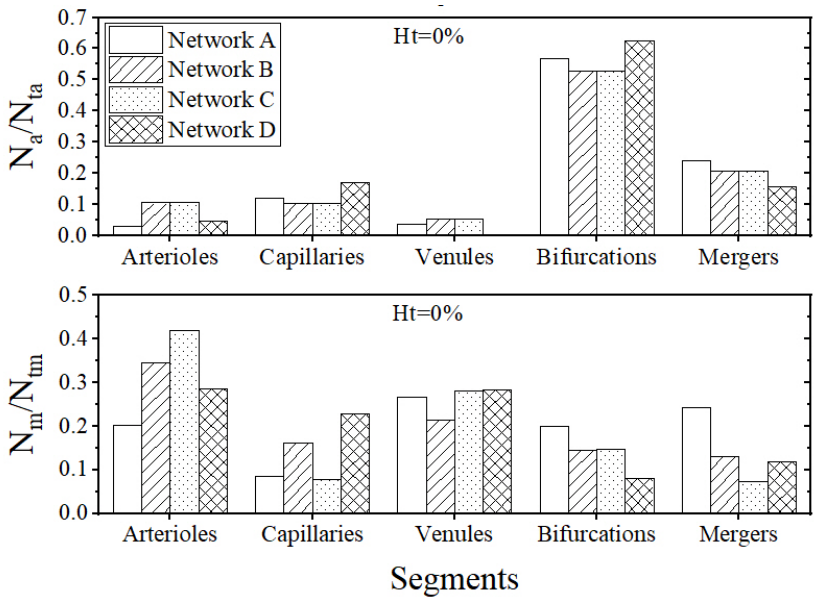

Figure 3.9: Segment-wise distribution of NPs at Ht = 0 to isolate the geometry effect. Shown are N_a/N_{ta} and N_m/N_{tm}.

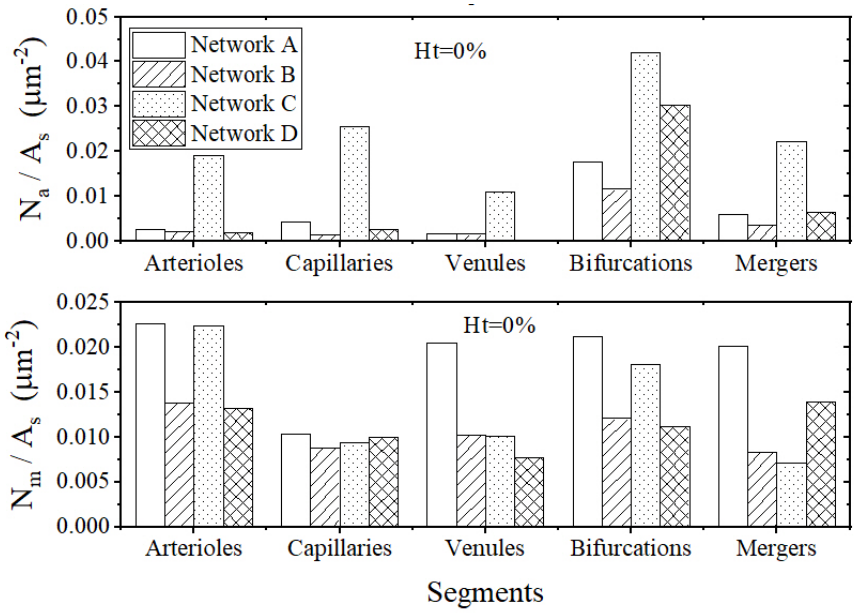

Figure 3.10: Segment-wise distribution of NPs at Ht = 0 to isolate the geometry effect. Shown are N_a/A_s and N_m/A_s.

Furthermore, in figure 3.10 we present adhered or marginated particles in each segment scaled by the area of that segment for Ht = 0. This further confirms the aforementioned observation that even in the absence of the RBCs, particle accumulation is very non-

uniform for adhesion simulation, with the highest accumulation in the bifurcations, while more uniform accumulation is observed for margination cases, with a slightly lower margination in the capillary segments.

The mechanism of higher NP adhesion at bifurcations for Ht = 0 case is shown in figure 3.11 for an example bifurcation. The streamlines from the center of the feeding vessels bring the NPs flowing in the middle of the vessel close to the divider at the bifurcation. If these NPs are within the limits of adhesion region from the wall, they will accumulate at the inside edge of the bifurcation as shown.

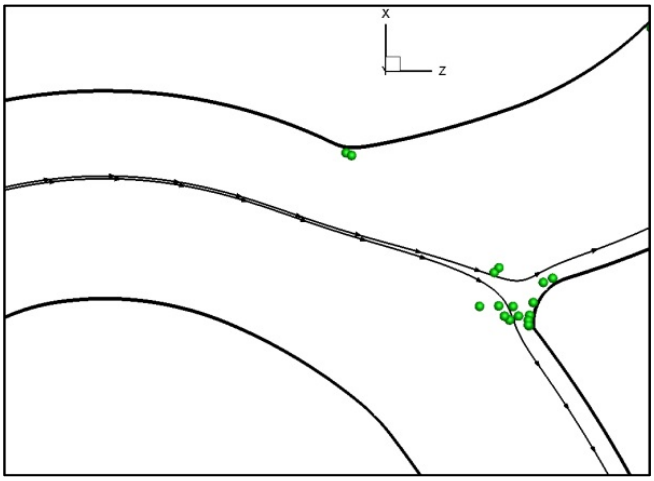

Figure 3.11: Mechanism for higher adhesion in bifurcation at Ht = 0%. Streamlines (hence, NP trajectories) from the central region of the feeding vessel arrive close to the inside edge of a bifurcation leading to higher adhesion there.

Next, we investigate how the presence of the RBCs significantly enhances the adhesion of NPs at bifurcations. We focus at a selected bifurcation and plot the number of particles adhered over time comparing 0% and 25% Ht cases, figure 3.12. The rate of NP adhesion is higher for 25% Ht case. The N_a versus time plot for 25% Ht shows three behaviors as marked by A, B, and C, corresponding to high adhesion rate, very low adhesion rate, and

moderate adhesion rate. These three stages are illustrated in figure 3.13 and related to how RBCs flow in a vessel in the networks. The flow of the RBCs is, in general, not continuous over time. Instead, they flow intermittently. As such, the 'local' hematocrit at a bifurcation strongly varies with time. The stage 'A' corresponds to a time window when a cluster of RBCs flows through the bifurcation, momentarily increasing the local hematocrit. As the cluster has to squeeze through the smaller daughter vessels, it fills nearly the entire cross sections, forcing many NPs to come within the adhesion limit, and causing a rapid increase in the number of adhered NPs. The low adhesion rate corresponds to the window of time when no RBC flows through the bifurcation, and hence, similar to the situation of 0% Ht. The moderate rate of adhesion occurs when the RBCs flow with a reduced hematocrit C this often results in a single-file motion of the cells so that a fewer number of NPs are pushed to the adhesion region.

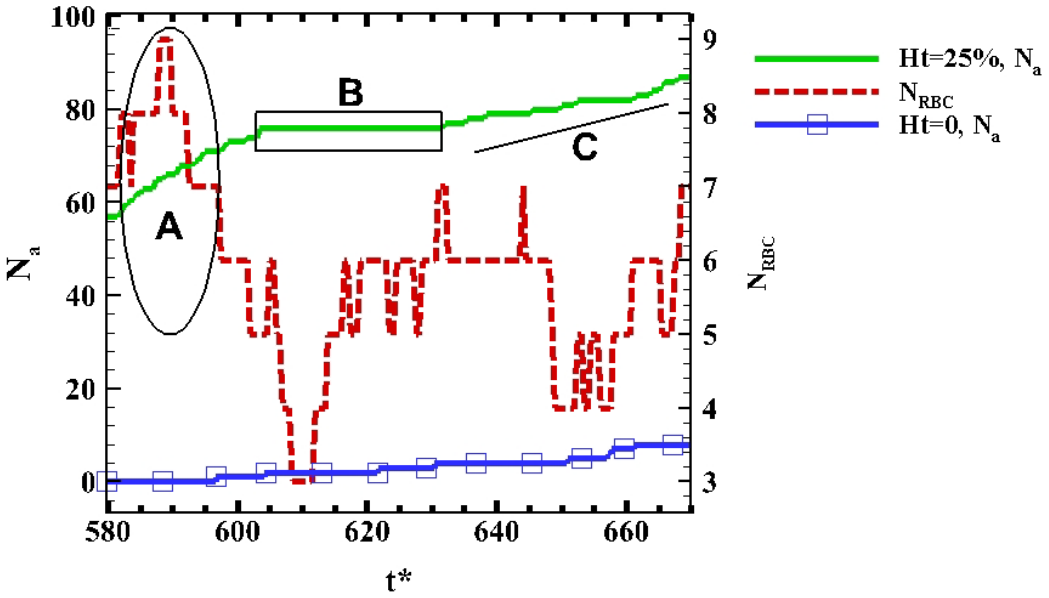

Figure 3.12: Mechanism of highest adhesion in bifurcations: Number of NP adhered versus dimensionless time for Ht = 25% (green line, left axis), and Ht = 0% (blue line, left axis), and number of RBCs flowing through the bifurcation (red dash, right axis).

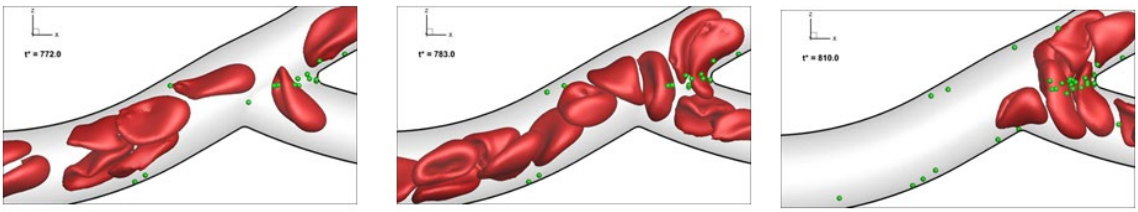

Figure 3.13: Mechanism of RBC-induced higher NP adhesion at a bifurcation. The sequence illustrates the time window 'A' in figure 3.12 when the rate of adhesion is high. The cluster of RBCs forces the NPs to come within the adhesion region as it traverses the bifurcation.

Figure 3.14 shows N_a versus time for selected arterial, capillary and venule. The rate of adhesion decreases sequentially. As noted before, NP adhesion and its rate is the lowest in the venule segments. This is because the cell-free layer has a higher thickness in these segments compared to others, as shown in figure 3.15. As the RBCs come out of two feeding vessels into a venule, they usually do not fill the entire cross-section causing an increase in the cell-free layer. While an increased CFL thickness results in many NPs being within the CFL, they are not forced by the RBCs further towards the wall to come within the adhesion limit. This results in the lowest adhesion of NPs in the venule segment. The N_a versus time curve for the venule segments shows longer window of time with nearly zero slopes.

The same mechanism is the reason for the highest margination of NPs in the venular segments. Since the CFL thickness is higher in this segment group, there is more number of NPs happen to be flowing through the CFL, resulting in an increase in the marginated NPs in the venule segment. Similarly, the dependence of margination on the CFL thickness exists in arterioles and capillaries. In addition to vessels, we found that this dependence is also exists within bifurcations and mergers. In general, it is observed that

mergers have higher thickness of the CFL than bifurcations, so that, the margination in mergers is expected to be higher than that of bifurcations as shown in figure 3.5.

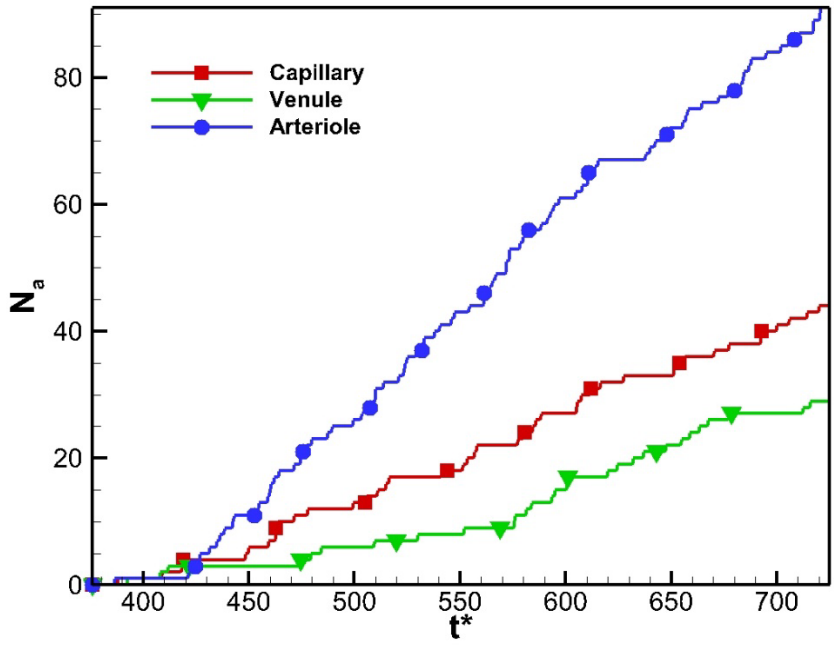

Figure 3.14: Number of adhered NPs versus time for a selected arteriole (blue), capillary (red) and venule (green).

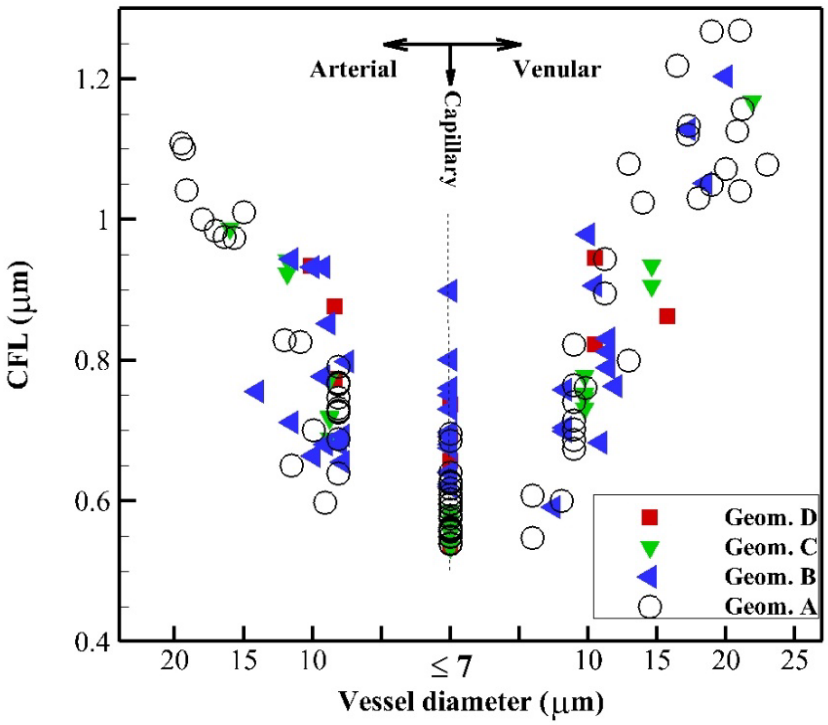

Figure 3.15: Average thickness of the cell-free layer in the simulated networks.

3.2.3 Heterogeneity of margination and adhesion of NCs throughout various vessels and bifurcations generations

In the above analysis, we divided each network into five segment groups, namely, arteriole, capillaries, venules, bifurcations, and mergers. The overall picture that arises is that both adhesion and margination are highly non-uniform, with the highest adhesion being in the bifurcations, and relatively higher margination in the venular segments. Within each group, there is also a strong heterogeneity when different locations are considered. This is shown in figure 3.16 (top) for marginated particles using color contours showing the number of marginated particles scaled by the area for each segment. The heterogeneous distribution is evident here: some venules have noticeably higher marginated particles than others. Similar heterogeneity exists within the other segments, namely, arterioles, capillaries, bifurcations, and mergers.

As before, heterogeneity at the segment-level is also correlated to the CFL thickness. To show this, we also plot the CFL thickness in each segment as color contours in figure 3.16 (bottom). When compared to N_m/A_s contours, it can be said that in general margination increases in a vessel with larger CFL.

To quantitatively show the correlation between the CFL thickness and margination, we plot these two quantities in figure 3.17 (top) for different vessels (artery, capillary, and venule) in network B. Also, in figure 3.17 we plot N_m/A_s versus CFL thickness (bottom). In general, N_m/A_s increases with increasing CFL thickness, thereby suggesting a positive correlation between the two.

The similar positive correlation between the CFL thickness and marginated NP area density is also observed for bifurcations and mergers as shown in figure 3.18. In this

figure, the top figure shows the dependence of a segment margination area density on the CFL thickness, and the lower figure shows the positive trend between margination area density and CFL thickness.

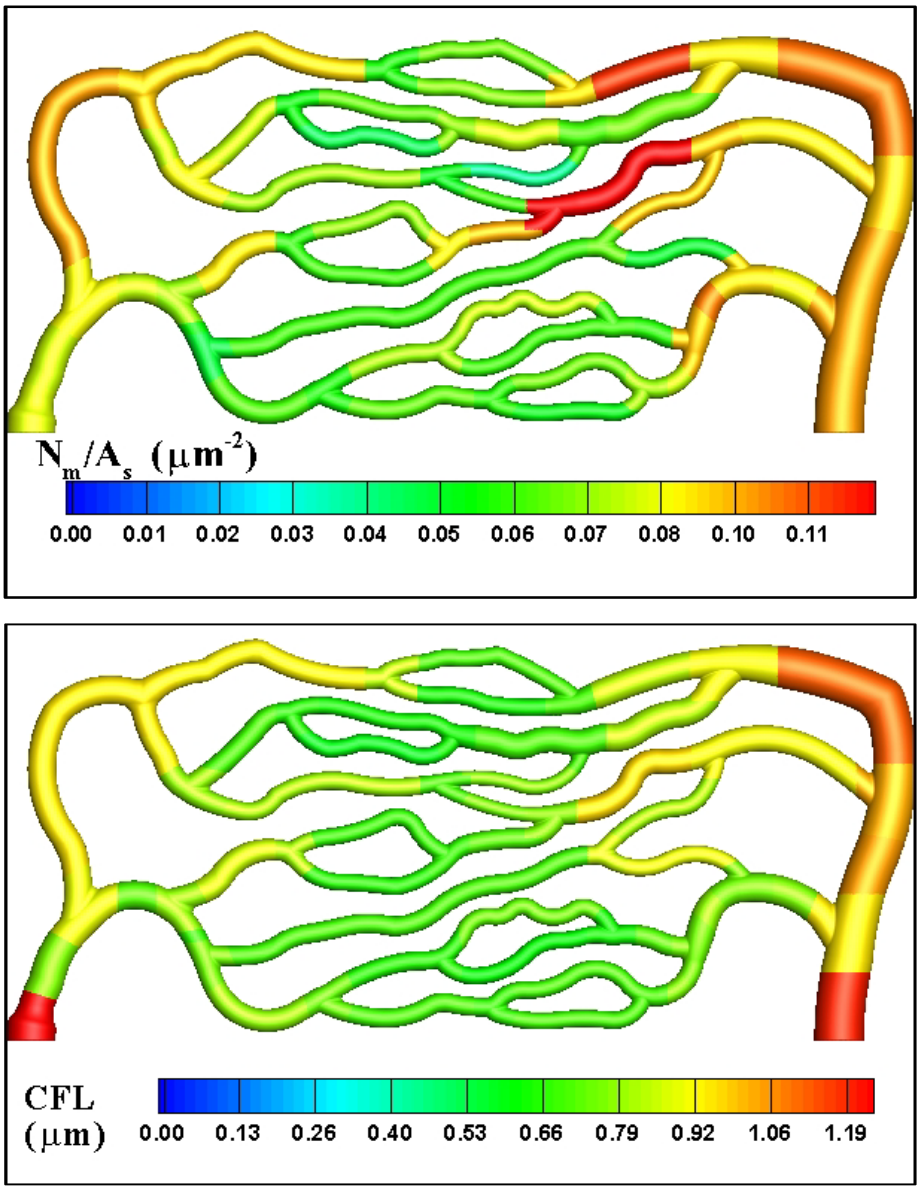

Figure 3.16: Number density (scaled by vessel surface area) of marginated particles in each segment (top) and the mean CFL thickness (bottom; in micrometer) shown as contours.

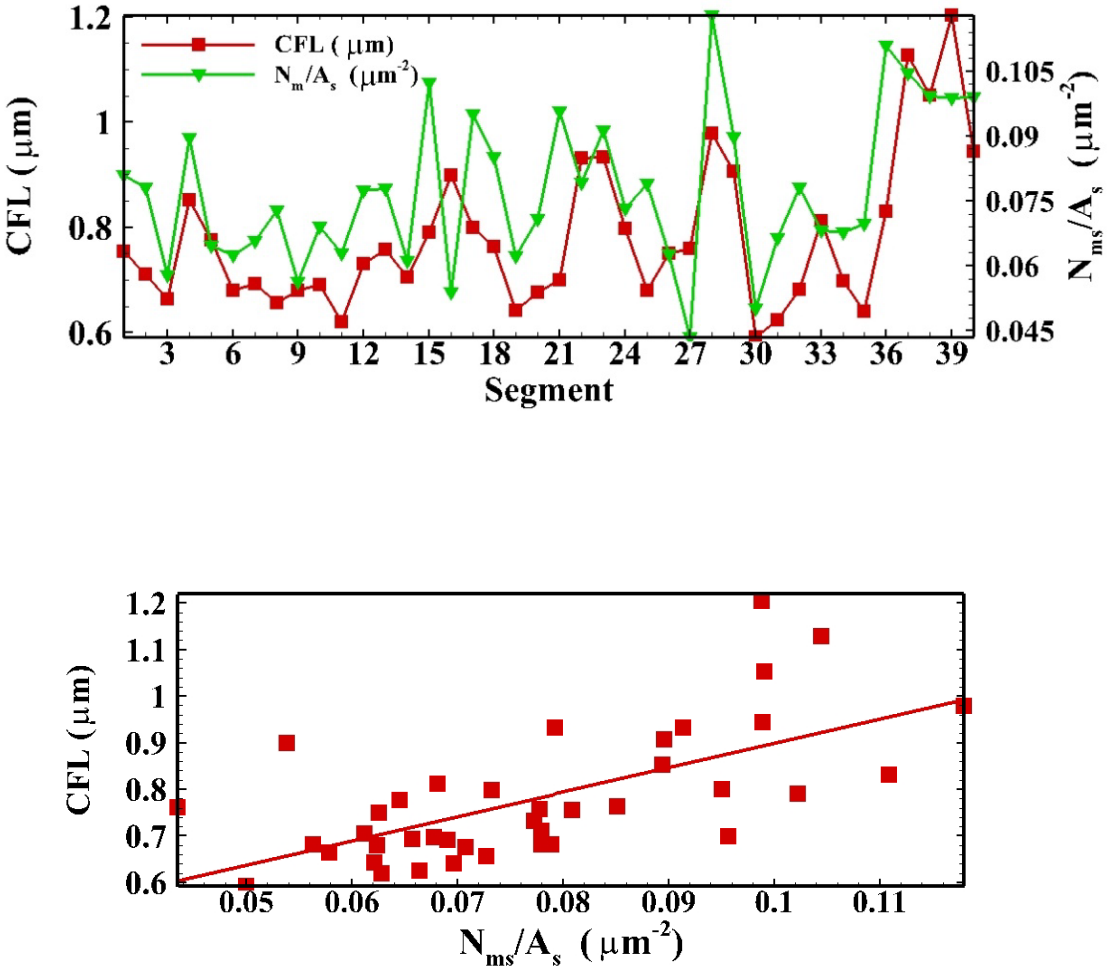

Figure 3.17: CFL thickness and margination number density (scaled by vessel surface area) of marginated NPs are shown for different vessel segments for Network B (top). Also, shown CFL thickness versus margination number density for the same network (bottom). The straight line is a linear fit through the data.

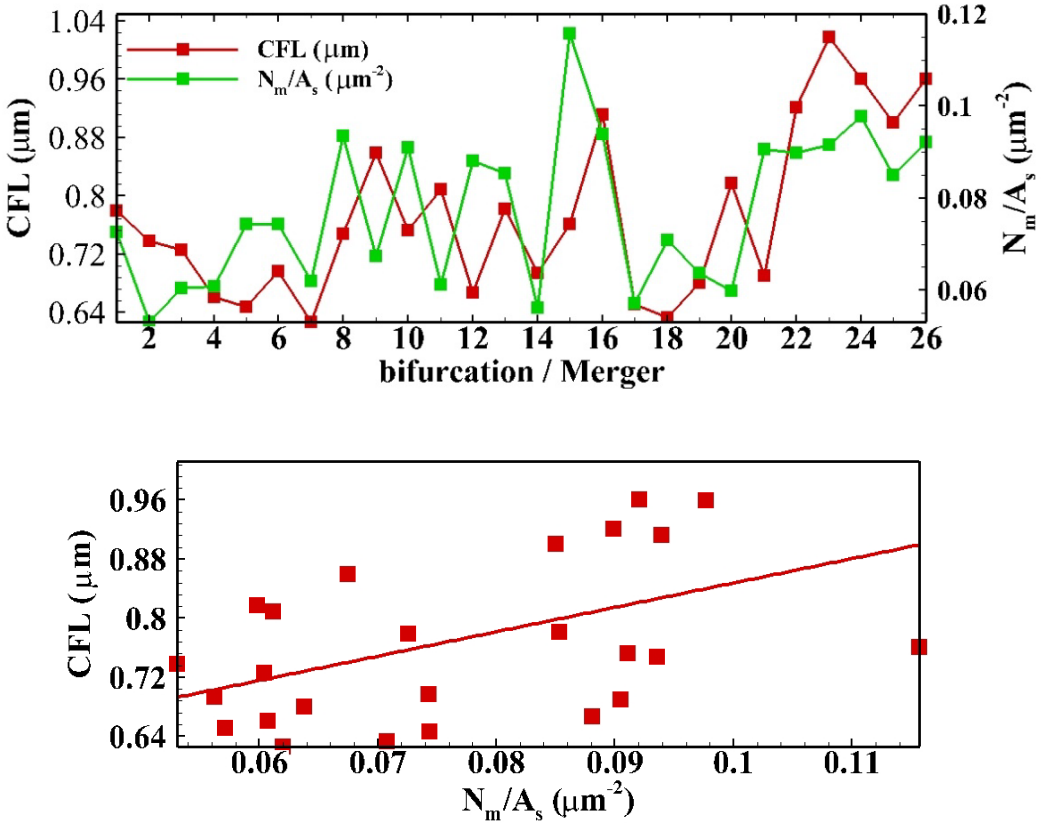

Figure 3.18: CFL thickness and margination number density (scaled by vessel surface area) of marginated NPs are shown for different bifurcation and merger segments for Network B (top). Also shown CFL thickness versus margination number density for the same network (bottom). The straight line is a linear fit through the data.

A similar heterogeneity within a specific group of segments is also present for the adhered NPs. In figure 3.19 we show the surface area density of the adhered NPs over an entire network (left). It is readily apparent that not all bifurcations have a similar amount of accumulation. It appears that the adhesion is somewhat positively correlated to the Ht distribution which is also shown in the figure (right). To more quantitatively establish the correlation, we also plot adhered NP density versus hematocrit for different vessels in figure 3.20. The general trend of the data suggests that NP adhesion increases with increasing Ht. While a weakly positive trend is observed when all vessels and segments

in a network are considered, a stronger correlation exists when only bifurcations are considered.

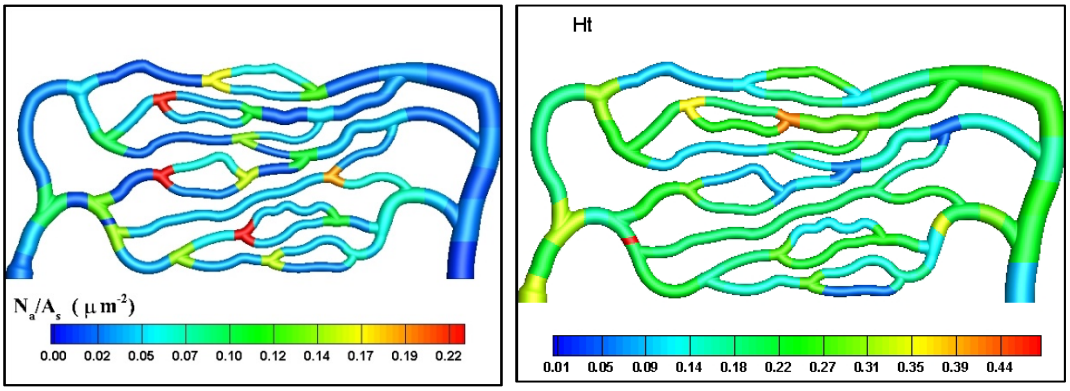

Figure 3.19: Surface area density of adhered NPs (left) and Ht (right) in each segment of network B shown by color contours.

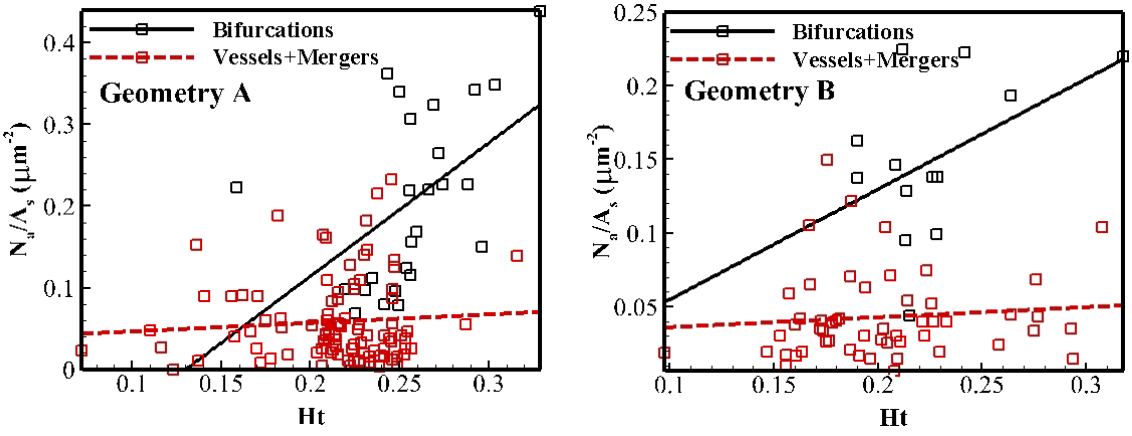

Figure 3.20: Surface area density of adhered NPs versus Ht in all segments of networks A (left) and B (right). The black symbols and line are for bifurcations only, and red symbols and line are for vessel segments and mergers.

Another way of quantifying the heterogeneity is to consider the NP accumulation in different generations (hierarchy) of segments. For each segment type in arterioles and bifurcations, the first segment is defined as of generation 1. That is, the feeding artery in any network would be generation 1 artery, and subsequent (hierarchically) arteries would be generation 2, 3 and so on. Similarly, the first bifurcation in the network would be generation 1 bifurcation, and next bifurcations in the hierarchy would be termed as generation 2, 3, etc. For the venular side, the final collecting venule is marked as generation 1 venule, and the generation number increases opposite to the flow towards the capillary vessels. Figure 3.21 shows the surface area density of marginated and adhered NPs for network C. NP accumulation increases with increasing generation. Network D behaves similarly to network C. Nevertheless, figure 3.22 gives the same accumulation along levels of segments in networks B. Here, the most accumulation exists in the middle levels, and we see less accumulation on the beginning and end levels. Network A behaves similarly.

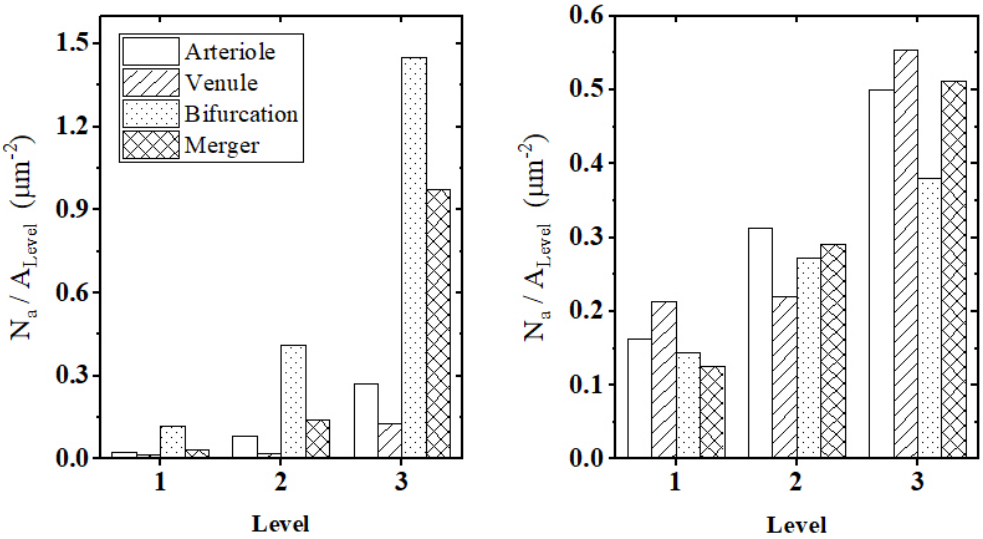

Figure 3.21: NP accumulation (per unit surface area for each segment group) presented as a function of segment generation level in network C.

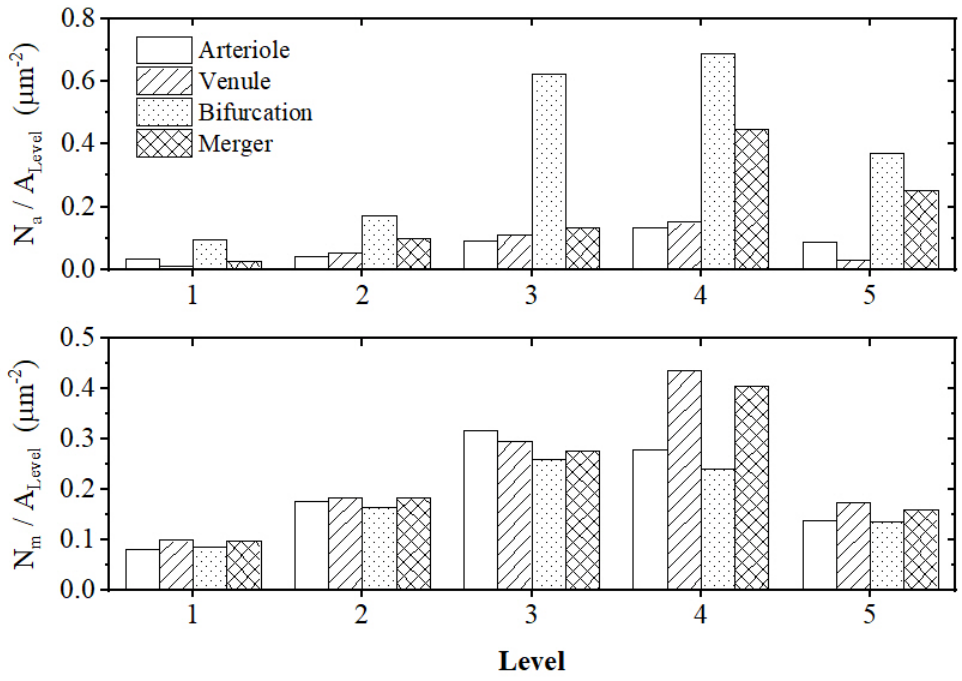

Figure 3.22: NP accumulation (per unit surface area for each segment group) presented as a function of segment generation level in network B.

3.3 Conclusions

Transport and deposition of nanoparticles modeled as volume-less fluid particles are simulated in physiologically realistic microvascular networks with fully resolved flow dynamics of many red blood cells. Two types of simulations are performed. In margination simulations, a particle is considered marginated when it is within the RBC-free layer; it is, however, allowed to move by the flow and can get out of the CFL. In adhesion simulations, the tracer permanently adheres when it comes within about 270 nm from the vessel walls. Overall, our results show that the NP distribution is highly non-uniform across a network. Specifically, for the adhesion simulations, the bifurcations regions show a significantly enhanced NP accumulation. In contrast, for the margination simulations, the non-uniformity is less severe, with the venular segments showing the highest accumulation. Even within each type of vascular segments, a strong heterogeneity

is observed. In general, the area density of the adhered NPs is observed to correlate with the segment hematocrit. Specifically, at the bifurcations, the dynamics of the RBCs as they flow intermittently in clusters is shown to enhance the adhesion. As for the margination, NP accumulation is shown to correlate with the CFL thickness. Taken together, these results underscore the role of vascular network topology in NP deposition.

Chapter 4

Effect of Particles Finite Size on their Margination and Adhesion Likelihood

4.1 Introduction

4.1.1 Objectives

In this chapter, we will simulate and analyze the margination and adhesion likelihood of finite size nanoparticles (NPs) modeled as rigid spherical particles flowing with the blood in the microvascular networks. The main objective here is to understand the effect of NP size on its margination and adhesion likelihood behaviors in various regions of a vascular network. Three sizes of a spherical particle are considered: **0.5 μm**, **1.0 μm**, and **2.0 μm**. The effect of the hematocrit is also included in these analyses where two levels are considered: **0%** and **25%**. Also, as we did in chapter three for the tracer particles, it is important to understand the effect of microvascular network geometry on the margination of finite size NPs. Additional questions that will also be addressed are as follows. How does the heterogeneity in particles accumulation alter when the finite size effect is included? The motivation follows previous works which suggest that particles in the range of ~ 1 μm in diameter show elevated margination. This finding was based on simple geometries such as straight tubes or channels. We will investigate whether the same holds for the complex geometry of the vascular networks.

4.1.2 Simulation setup

The finite-sized particles considered here are in two-way interaction with the surrounding fluid. The flow regime is in Stokes flow (Re ≈ 0) as capillary networks are considered [99]. Following the definition of the Stokes number, St, in chapter three, it is clear that this value is very small ~ 10^{-5} so that NPs response time is still much faster than fluid response time. It also implies that Brownian effects are small compared with the convective effects. As found by [101] viscosity will become independent on Pe of ≥ 10^3 whence, Brownian motion is over-controlled by the advective motion. They also show that the inertia effect on the viscosity is important when Re ≥ 10^{-3} which is not the case in our simulations. The only expected effect that will influence the effective viscosity is the solid-fluid interaction at very low St. In our simulations of finite size spherical particles, the volume fraction of particles to the whole volume is at most up to 0.01. This shows the validity of applying the Einstein analytical formula $\eta_r = 1 + B \cdot \varphi$, where η_r is the ratio of the suspension viscosity to the suspending fluid viscosity (plasma), φ is the particles volume fraction, and B = 2.5 according to Einstein for the dilute suspension limit where $\varphi \leq 0.01$ [102]. This indicates that the increase of apparent viscosity due to particles addition is very small (0.025).

Due to computational time restrictions, the total number of particles in the network is limited to as shown in Table 4.1. The time cost can reach up to 9 wall clock hour/1 dimensionless time unit in network A. In the presented analysis, we scaled the number of marginated particles by the total number of supplied particles, so that the effect of varying number of supplied particles on the results is eliminated.

Table 4.1: Number of particles distributed for each size.

Diameter size (μm)	Number of particles	Number of nodes per NP	Number of elements per NP
0.5	1000	42	80
1.0	800	162	320
2.0	100	624	1280

The margination criterion in this chapter is different from that considered in chapter three. Here, we consider a particle to be marginated if any portion of its surface lies within the CFL. That is because hydrodynamic and physiological interactions between a particle surface and the wall may be initiated even if the particle centroid is not within the CFL but a portion of its surface is. Hydrodynamic interaction in Stokes flow is long-range and acts over many particle diameters. Physiologically, the ligand-receptor interaction occurs when a particle surface is a few hundred nanometers away from the wall. On the other hand, we choose specific distance to identify that a particle is likely to adhere. However, there is a numerical restriction on how close a particle can get to the vascular walls. To prevent a nanoparticle to cross over the wall, we implemented a repulsive force that is activated over two Eulerian mesh from the wall, which is about 500 nm. We found that a suitable limit to test the adhesion likelihood is 650 nm to 800 nm (2.5 to 3.0 grid size). In fact, we have tested the adhesion likelihood behavior in all network segments for various limits from 2.5 to 5.5 grid sizes; the results show that within this range of distances tested, the behavior of adhesion likelihood is not affected significantly. In the presented results which will follow, adhesion likelihood criterion is set as 650 nm (or 2.5 grid size). That is, when a particle surface comes within 650 nm off

the wall, we identify this NP as adhered. There are 24 simulations done for the analyses in this chapter in total.

4.2 Results

4.2.1 Margination and adhesion likelihood of finite-sized NCs through various segments of the networks

4.2.1.1 Margination analysis

Figures 4.1 to 4.4 present snapshots showing the distribution of RBCs and particles at a specific time instant of each simulation. Care must be taken here, as the figures show an instantaneous particle distribution at a specific time only. As noted before, particles can marginate but later leave the near-wall region.

Analysis of margination of rigid particles in these simulations shows similarity with the tracer particles discussed in chapter three. As observed for the tracer particles, the margination of finite-size particle distribution is non-uniform across different regions within the same network. For these simulations, there is a relatively higher margination observed in the venular regions while much less margination is observed in the capillary. However, there is also a similar amount of accumulation of marginated NPs in arterioles to that in the venules. Bifurcations and mergers have an intermediate amount of margination between venules and capillaries. This is clearly quantified in figure 4.5 and figure 4.6. In these two figures, particle distribution is identified in five different segments of the vasculatures, namely, arterioles, capillaries, venules, bifurcations, and mergers. Again, capillaries are defined as the terminal arteries which do not bifurcate any further.

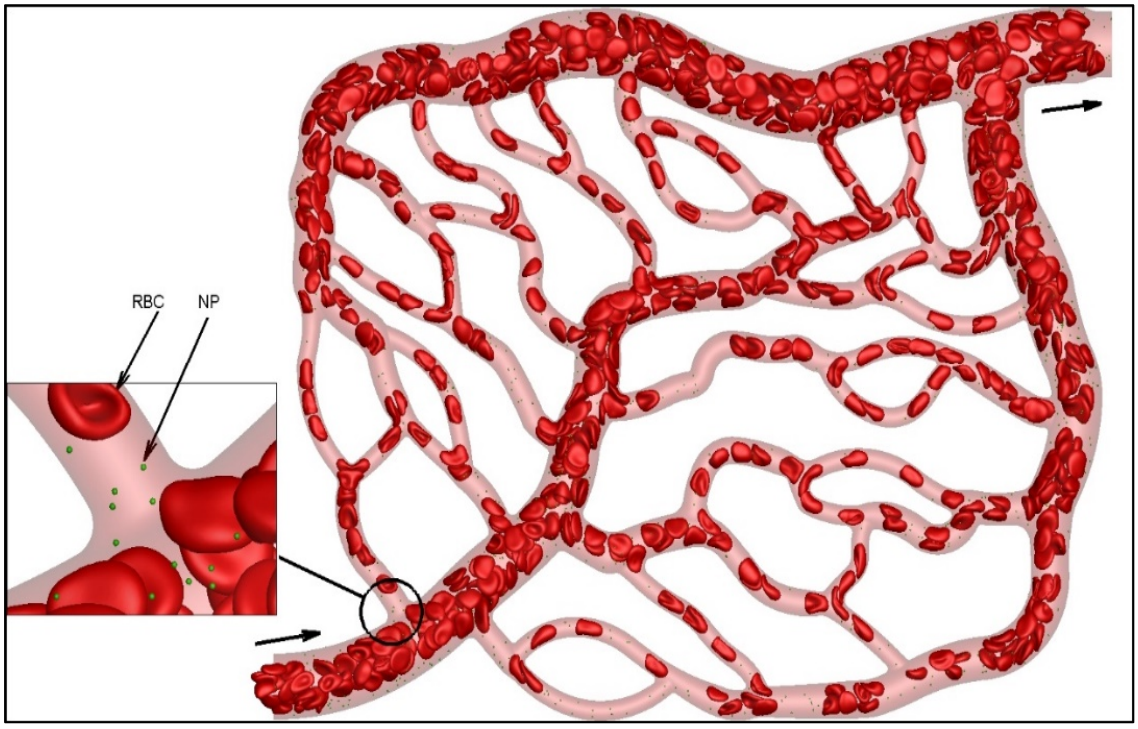

(a) d=0.5 µm

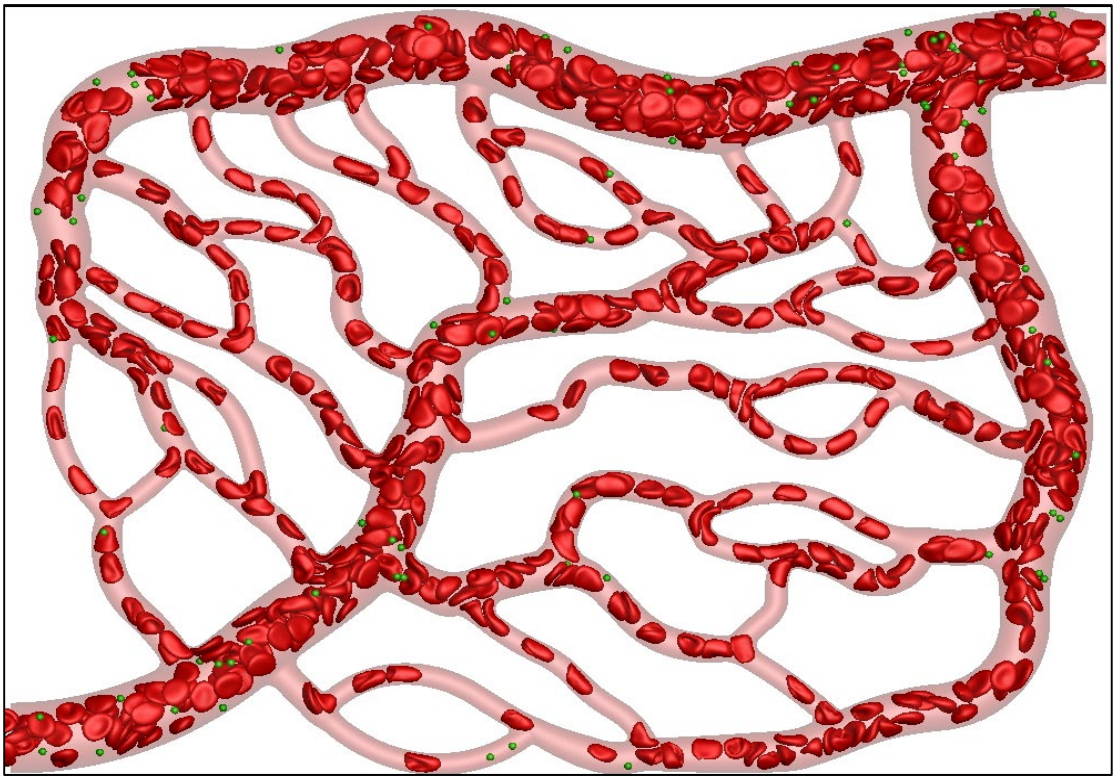

(b) d= 2.0 µm

Figure 4.1: Snapshots of the final time instant for particle size (a) 0.5µm and (b) 2.0µm simulations in the network A at Ht = 25%. Hereafter NPs are shown in green, and RBCs in red.

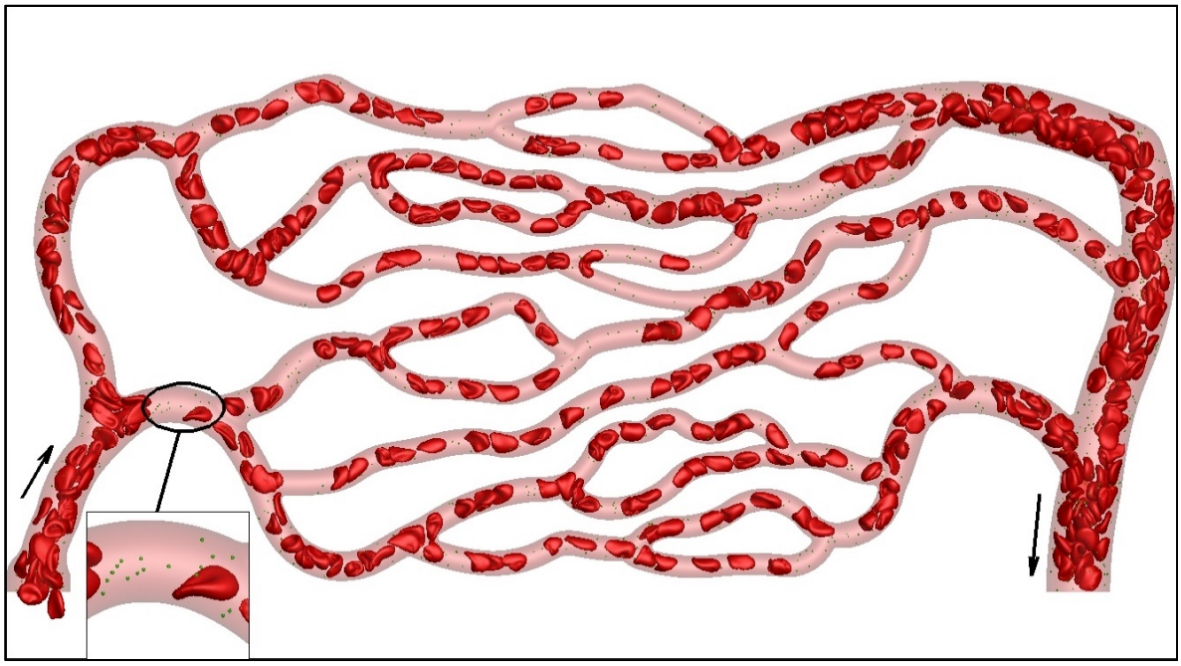

(a) d = 0.5 µm

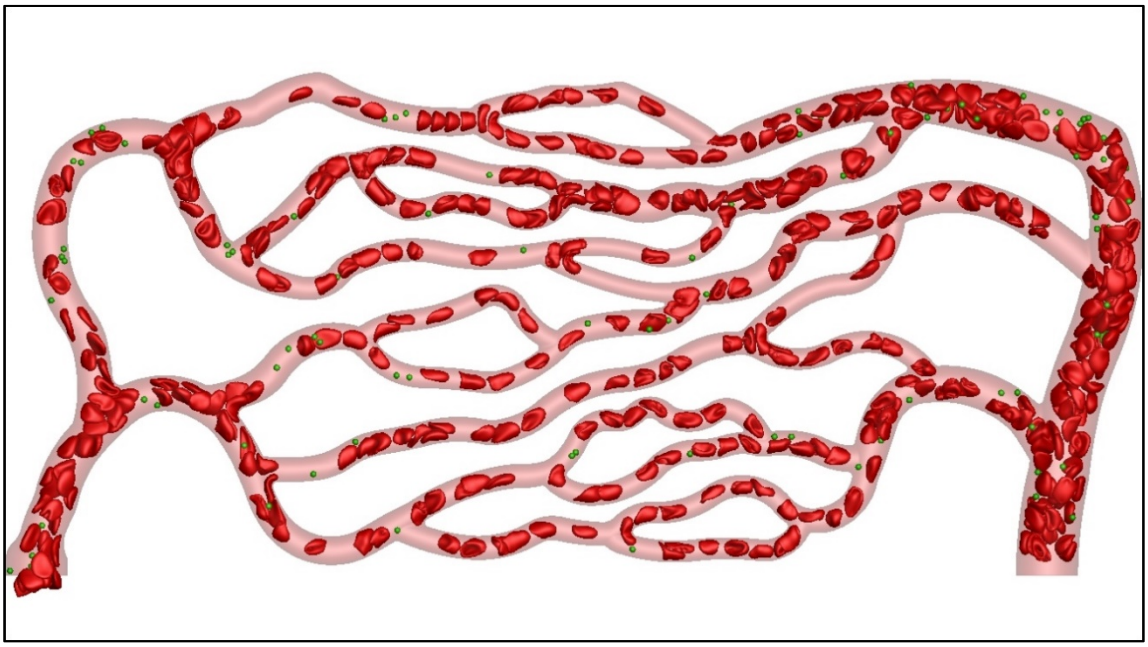

(b) d = 2.0 µm

Figure 4.2: Snapshots of the final time instant for particle size (a) 0.5µm and (b) 2.0µm simulations in then network B at Ht = 25%.

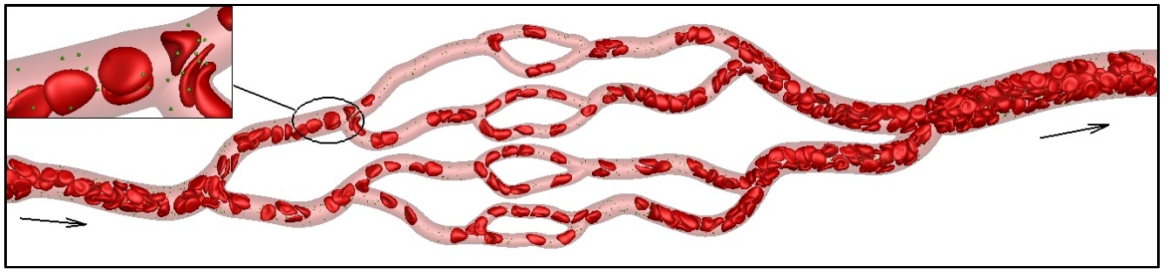

(a) d = 0.5 µm

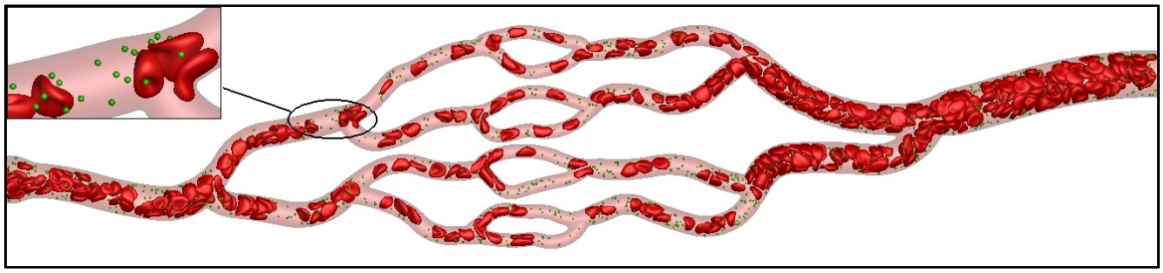

(b) (b) d = 1.0 µm

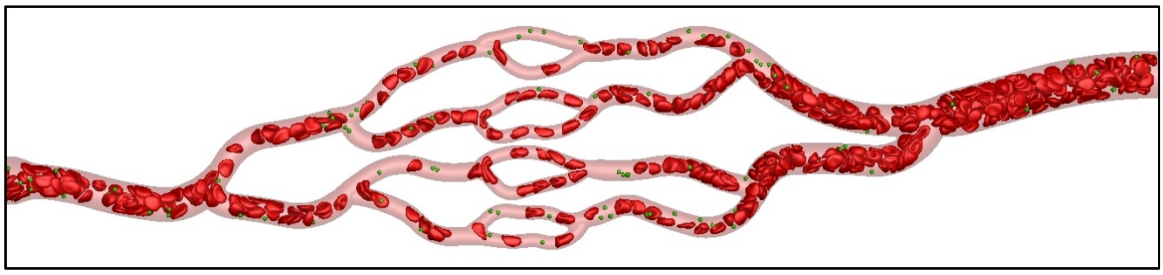

(c) d = 2.0 µm

Figure 4.3: Snapshots of the final time instant for particle size (a) 0.5µm, (b) 1.0µm, and (c) 2.0µm simulations in the network C at Ht = 25%.

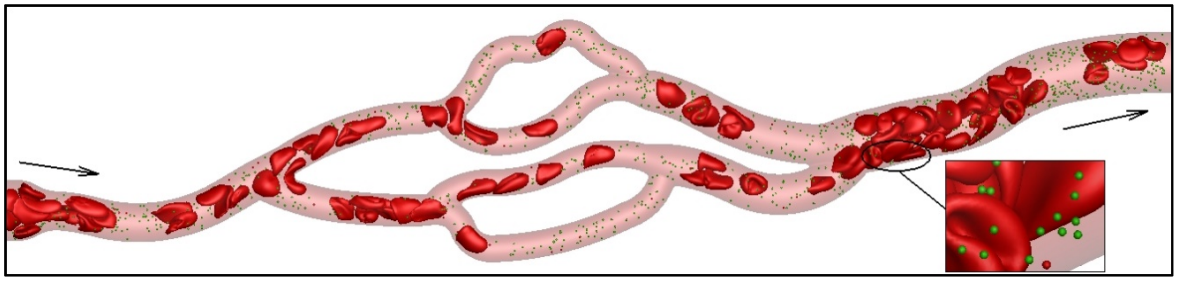

(a) d = 0.5 µm

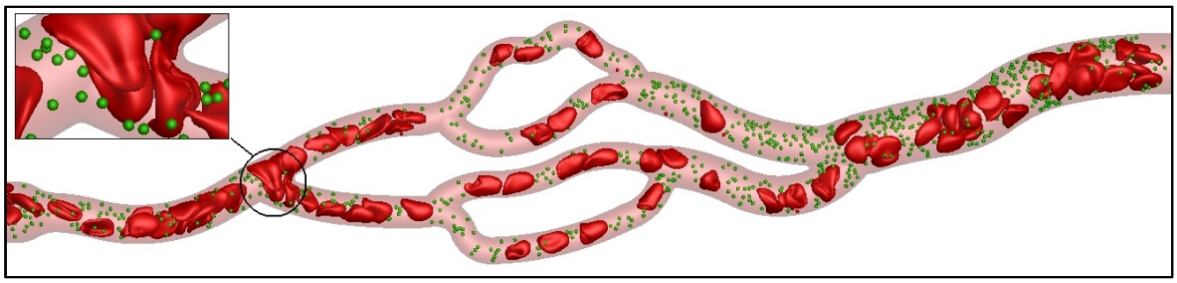

(b) d = 1.0 µm

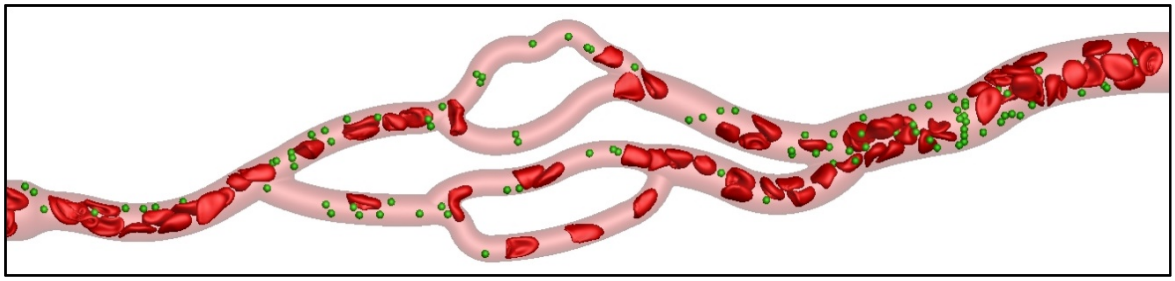

(c) d = 2.0 µm

Figure 4.4: Snapshots of the final time instant for particle size (a) 0.5µm and (b) 1.0µm, and (c) 2.0µm simulations in the network D at Ht = 25%.

Also, while presenting the data in these figures, we consider two ratios: **(i)** figure 4.5 shows the ratio of the number of marginated particles in each segment to that of the total number of particles supplied in the entire vasculature (N_m/N_s), and **(ii)** figure 4.6 shows the ratio of the number of marginated particles in each segment to the total number of marginated particles in the entire networks (N_m/N_{tm}). Note that in these plots, we do not distinguish between different generations of vessels. These margination trends are valid for all four vascular networks simulated. Since these networks have different

architectures, we conclude that the predicted non-uniformity in particle accumulation would occur in any microvasculature in vivo.

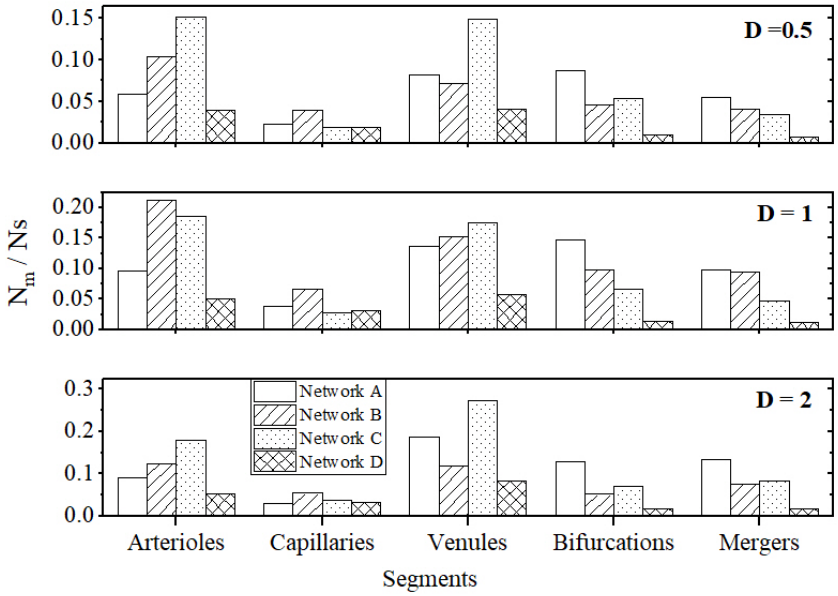

Figure 4.5: NP distribution in different segment for Ht = 25%. The ratio of the number of marginated NPs to the total number of supplied NPs (N_m/N_s) is shown.

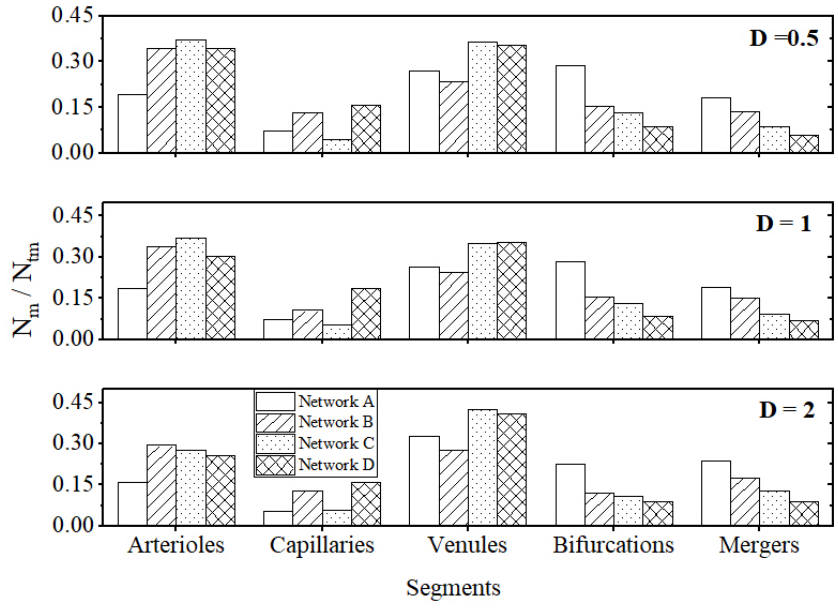

Figure 4.6: NP distribution in different segment for Ht = 25%. Shown is the ratio of the number of marginated NPs in each segment to the total number of marginated particles in the entire networks, N_m/N_{tm}.

These margination trends are valid for all four different vasculatures and particle sizes simulated; therefore, we conclude that the predicted non-uniformity is a result of network configuration. This highlights the importance of the geometry parameters within the targeted microvasculature.

In general, different segments of a network, as defined here, have different surface areas. The actual number of particles marginated will depend on the vessel or segment surface area. In figure 4.7, we scale the number of particles marginated by the surface area of each segment (i.e., N_m/A_s, where A_s is the area of each segment group). For the margination simulations of finite-size particles, the accumulation per area is more uniform, with the capillary segments have relatively less margination than others.

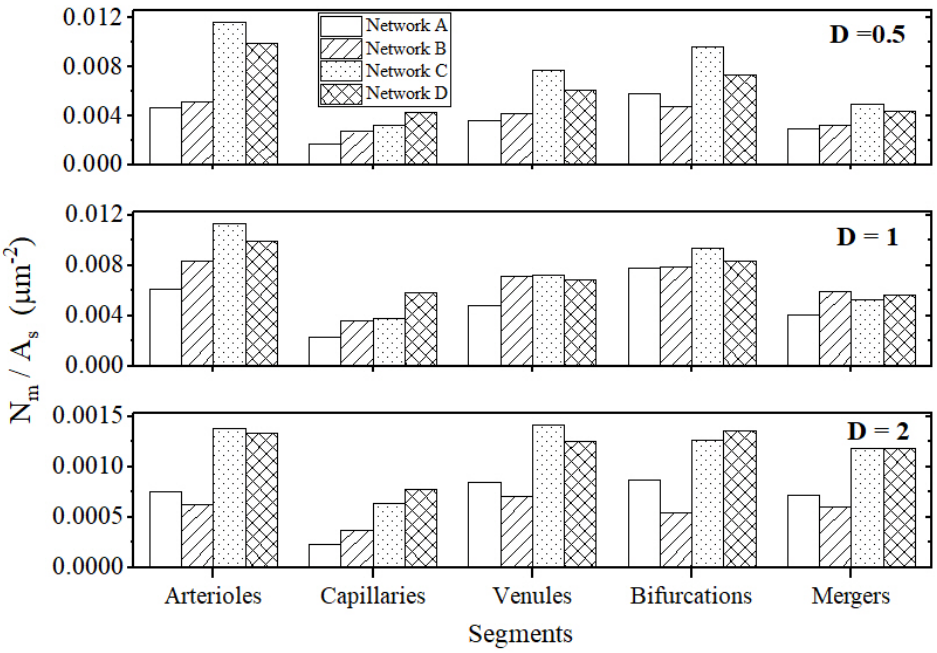

Figure 4.7: NP accumulation of marginated finite size particles per segment area (N_m/A_s) in various segments for Ht = 25%.

4.2.1.2 Adhesion likelihood analysis

Now, we will study the adhesion likelihood for finite-size particles under investigation. Figure 4.8 and figure 4.9 present the ratios N_a/N_s and N_a/N_{ta} for adhesion likelihood, respectively, where N_a/N_s is the ratio of particles likely adhered to the total supplied particles in the network, and N_a/N_{ta} is the ratio of particles likely adhered in each segment to the total number of the particles likely adhered in the network. In both figures, the behavior of d=2.0 μm is different from the others. For the lowest two sizes, the behavior is similar to the marginated particles; that is, a higher adhesion likelihood exists in the arterioles and venules. But the d=2.0 μm has the highest adhesion likelihood within bifurcation, similar to the tracer particles. However, this size has the lowest adhesion likelihood in the capillaries (not in the venules as was the case for tracers). This is a noticeable difference we observe here between NPs of different sizes.

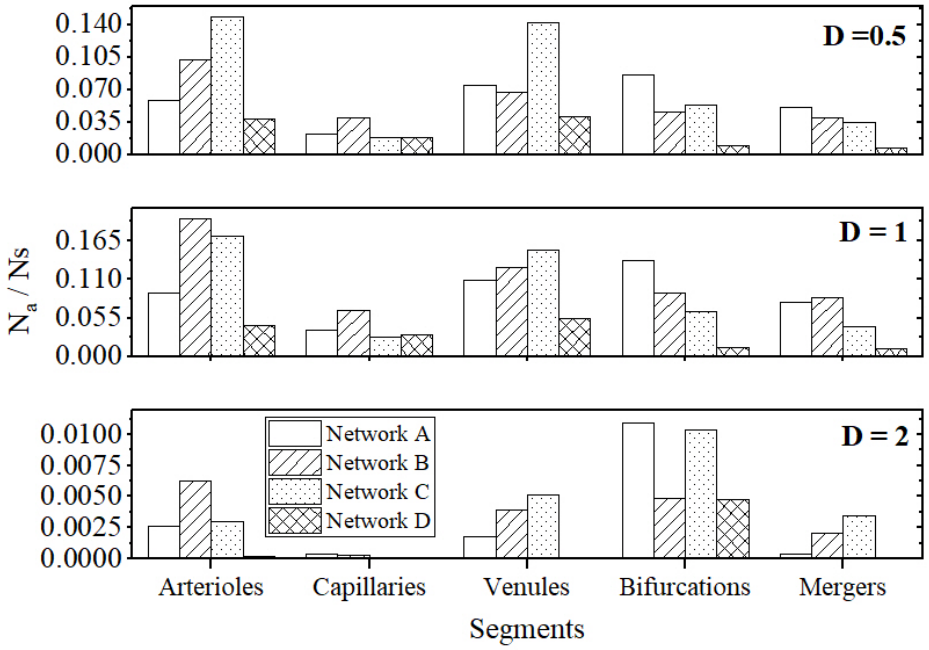

Figure 4.8: NP distribution in different segment for Ht = 25%. Rows show the ratio of the number of anticipated adhered NPs to the total number of supplied NPs (N_a/N_s).

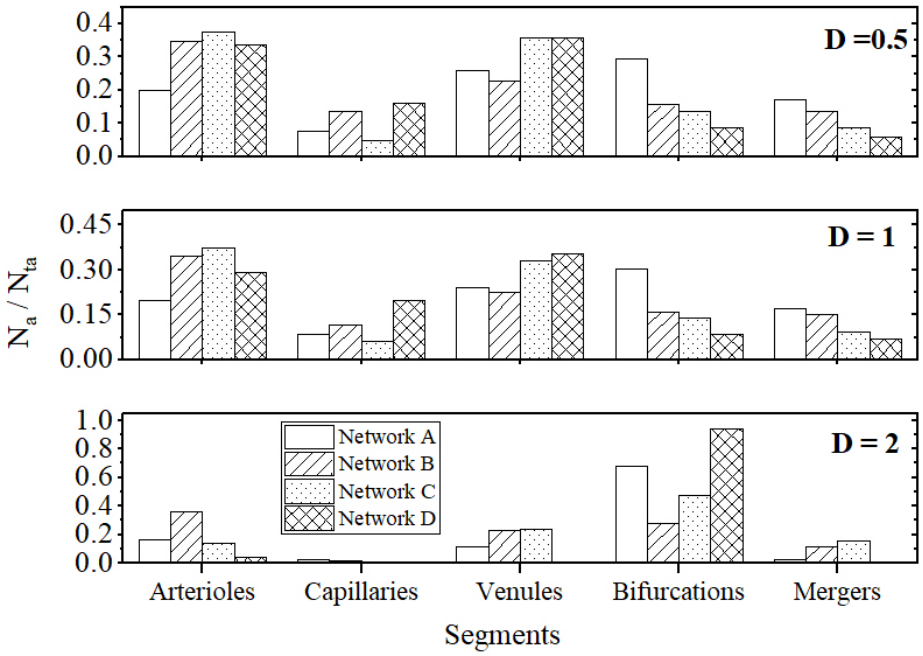

Figure 4.9: NP distribution in different segment for Ht = 25%. Rows show the ratio of the number of anticipated adhered NPs in each segment to the total number of anticipated adhered particles in the entire networks, N_a/N_{ta}.

4.2.2 Effect of geometry, hematocrit, and particle size on the margination of the NCs

The reasons behind the observed non-uniform accumulation of NPs in the previous section are investigated here. As noted before, NPs in a straight tube are marginated by the action of the RBCs. In contrast, the geometry of the network as characterized by bifurcations, vessel curvature, and mergers, may affect NPs accumulation in a network.

To separate the influence of the network geometry and that of the RBCs on the NPs margination, we simulated the flow of NPs in the four networks in the absence of any RBC (Ht = 0). The total marginated NPs as a fraction of supplied NPs (N_{tm}/N_s) over the entire network for all four networks and three tested diameters are shown in figure 4.10.

The upper chart in this figure shows that even in the absence of RBCs, there is a margination in the networks, which is not the case in the straight tube. This indicates the importance of the network topology. The lower chart in figure 4.10 shows the importance of the RBC where margination rate increases by about one order of magnitude in all networks and for all sizes in our study.

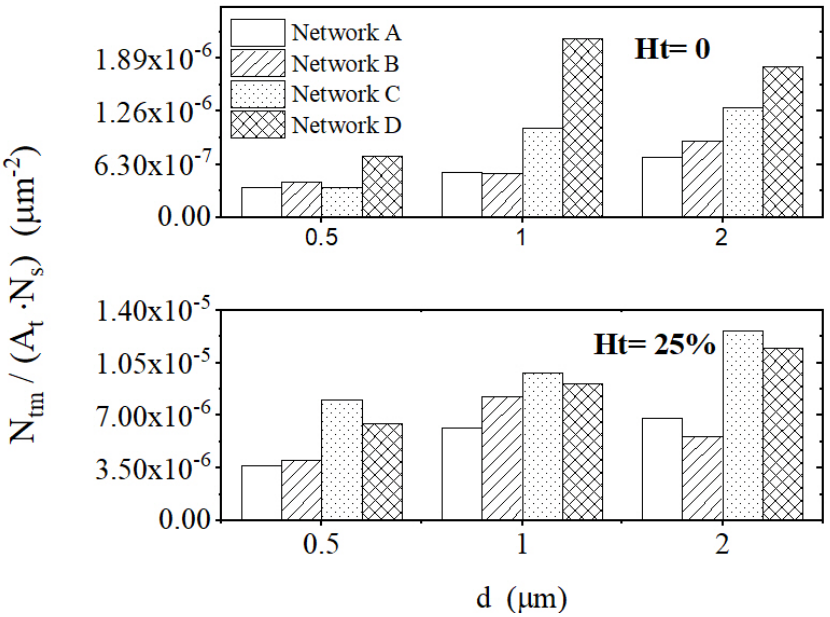

Figure 4.10: Ratio of total marginated NPs to the supplied NPs scaled by area of the network ($N_{tm}/N_s.A$) for different Ht and particle sizes.

The other main conclusion from figure 4.10 is that irrespective of the network configuration and Ht level, the accumulation of marginated particles increases with increasing particle size; the biggest particle diameter studied here (2.0 μm) shows the highest margination. This conclusion is in agreement with the previous works presented in section 1.3.1.4 (Specifically, the in vivo and in vitro works in [31], and the experimentation in tube with RBCs in [35]).

As noted before, the CFL has a higher thickness in venular segments compared to others, as shown in figure 3.15. As the RBCs come out of two feeding vessels into a venule, they usually do not fill the entire cross-section causing an increase in the cell-free layer. Besides, the increases in CFL thickness increase the possibility of NPs margination. It is very clear that the margination levels shown in figure 4.5 and figure 4.6 follow the CFL thickness distribution in figure 3.15. In capillaries, particles and RBC are observed to move in a train-carts (TC) manner, that is, a particle/cluster of particles followed by a RBC or RBCs. It is rare that particles and RBCs flow within capillaries together. This last issue is usually accompanied by the fact that RBCs push particles toward the walls within the CFL. This train-cart like phenomenon is caused by the RBCs lingering at the preceding bifurcations. Figure 4.11 illustrates this phenomenon. It is worth to mention that this phenomenon is rarely observed in precapillary arterioles or venules.

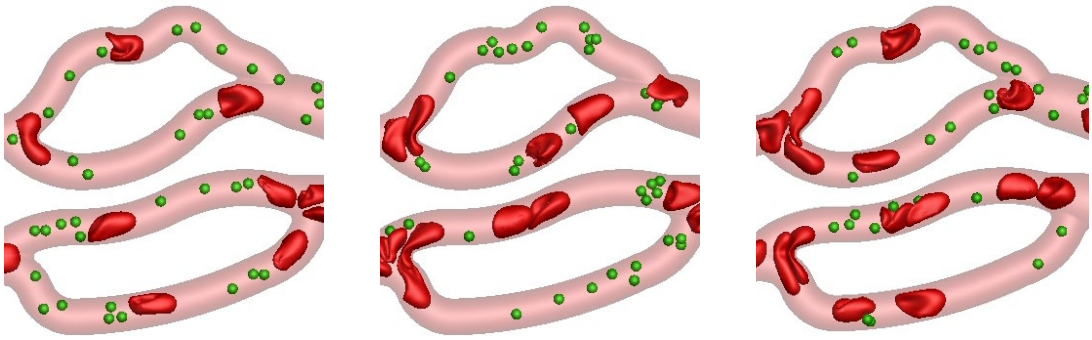

(a) (b) (c)

Figure 4.11: Motion of particles and RBCs within capillaries in a train-carts (TC) manner. Figure (a) pure TC motion; figure (b) TC motion and RBC+particle to enter a capillary; figure (c) TC motion accompanied with two occurrences of RBC+particle.

We further elaborate the geometry effect in the absence of RBCs by considering the marginated NPs distribution in different segments of a network as shown in figure 4.12, where the ratio N_m/N_s is plotted for Ht = 0. The results in this figure show that there is a strong non-uniformity in the distribution of marginated NPs even in the absence of the RBCs. The distribution of marginated particles in Ht = 0 simulations shows very low levels in the venules and mergers even the CFL thickness in the venules is the highest. However, there is no mechanism that acts to push particles within this layer. This is not observed in Ht = 25%. On the other hand, capillaries and arterioles have high levels of margination.

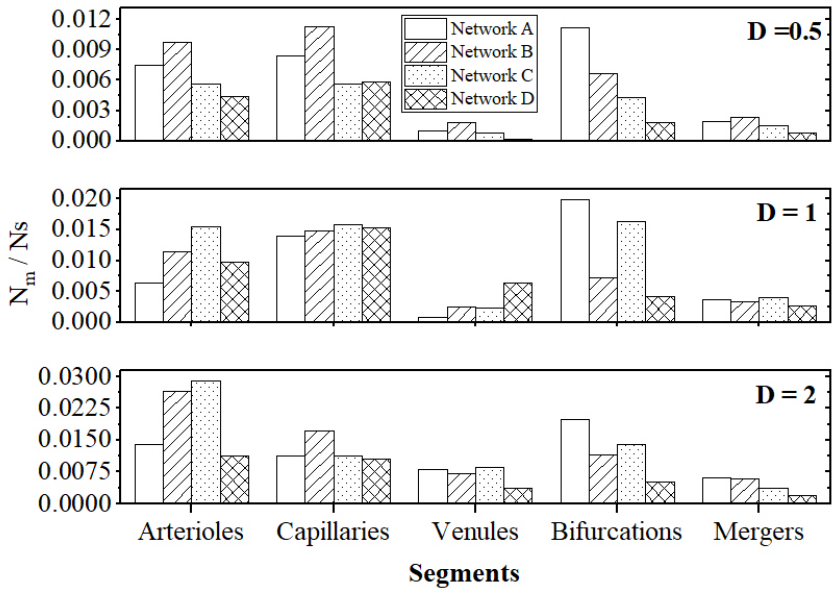

Figure 4.12: Segment-wise distribution of NPs at Ht = 0 to isolate the geometry effect. Shown are N_m/N_s.

Figure 4.13 presents the results of marginated particles in each segment scaled by the area of that segment for Ht = 0. This further confirms the observation mentioned above that in the absence of the RBCs, particle margination is also non-uniform, and has different behaviors in various segments compared to Ht = 25%. Comparing to Ht = 25%,

the bifurcation for Ht = 0 has higher margination, and this is because of the absence of RBCs. RBCs tend to push particles toward walls laterally, and the core becomes devoid of particles. As a result, very few particles are expected to marginate at the bifurcation apex for Ht = 25%.

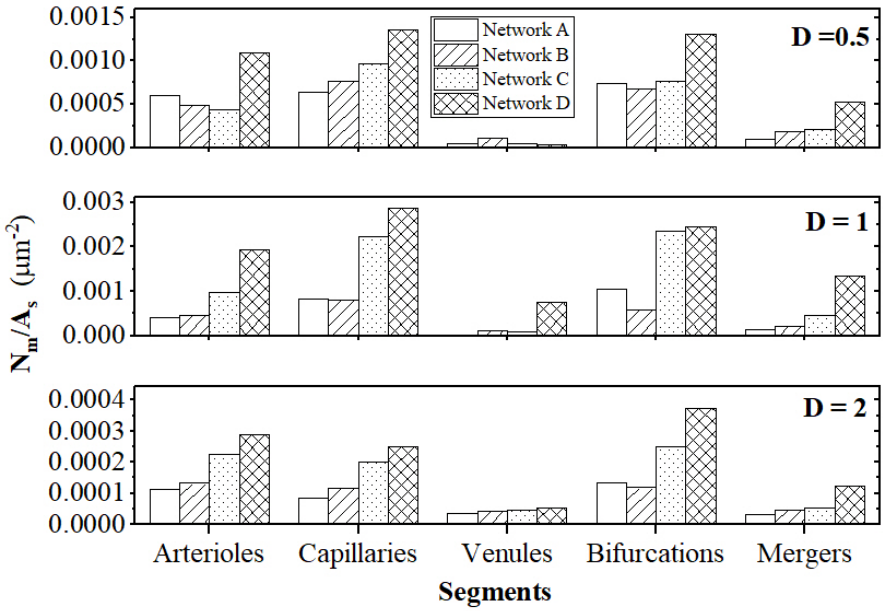

Figure 4.13: Segment-wise distribution of NPs at Ht = 0 to isolate the geometry effect. Shown are N_m/A_s.

The proportionality for the case of Ht = 0 is found to be correlated to not only the CFL thickness but also to the size of the segment (figure 4.14). The figure shows the ratio of CFL thickness divided by the radius of the segment. It is clear that the behaviors of margination in figure 4.12 and figure 4.13 are following the criteria (2 × CFL / d), where the minimum values for this ratio are in venules, and the maximum is in the capillaries.

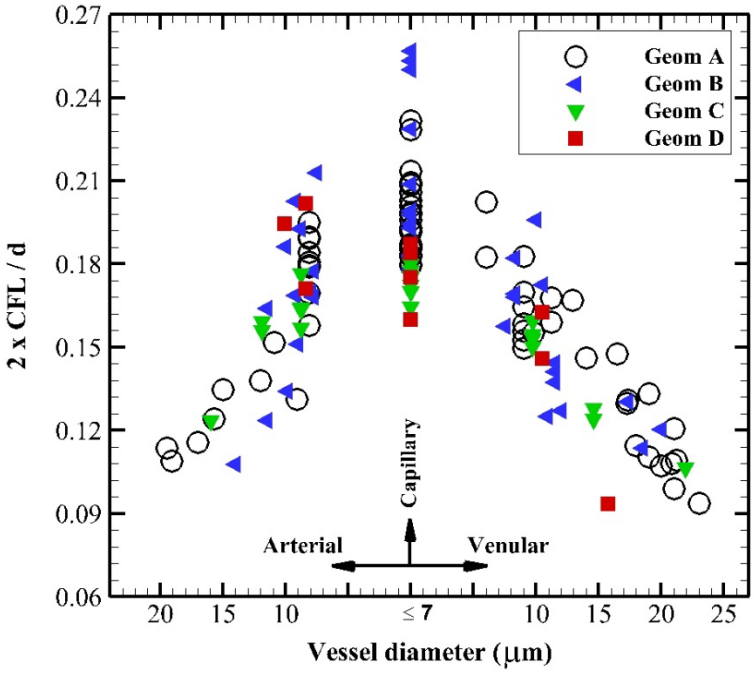

Figure 4.14: Ratio of the average thickness of the cell-free layer to the radius in the simulated networks.

4.2.3 Heterogeneity of margination and adhesion likelihood of NCs throughout various vessels and bifurcations generations

4.2.3.1 Margination analysis

The overall picture that arises in the analysis above is that margination is highly non-uniform, with the relatively higher margination in the arteriolar and venular segments and lowest in the capillaries. Within each one of the five groups discussed before, there is also a strong heterogeneity. This is shown in figure 4.15 for marginated particles where color contours represent the number of marginated particles scaled by the total number of particles for each segment. Note here that particle number density (scale by area) gives similar heterogeneity. The heterogeneous distribution is evident here as it reveals that some arterioles and venules have noticeably higher margination fractions than others.

As before, heterogeneity at segment-level is also correlated to the CFL thickness. To quantitatively show the correlation between the CFL thickness and margination, we plot these two quantities in figure 4.16 for different vessels (artery, capillary, and venule) in network C, and particle sizes under investigation. Also, figure 4.16 shows the plot of N_m/N_s versus CFL thickness. In general, N_m/N_s increases with increasing CFL thickness, thereby suggesting a positive correlation between the two. Similar positive correlation between the CFL thickness and marginated NP is also observed for bifurcations and mergers as shown in figure 4.17.

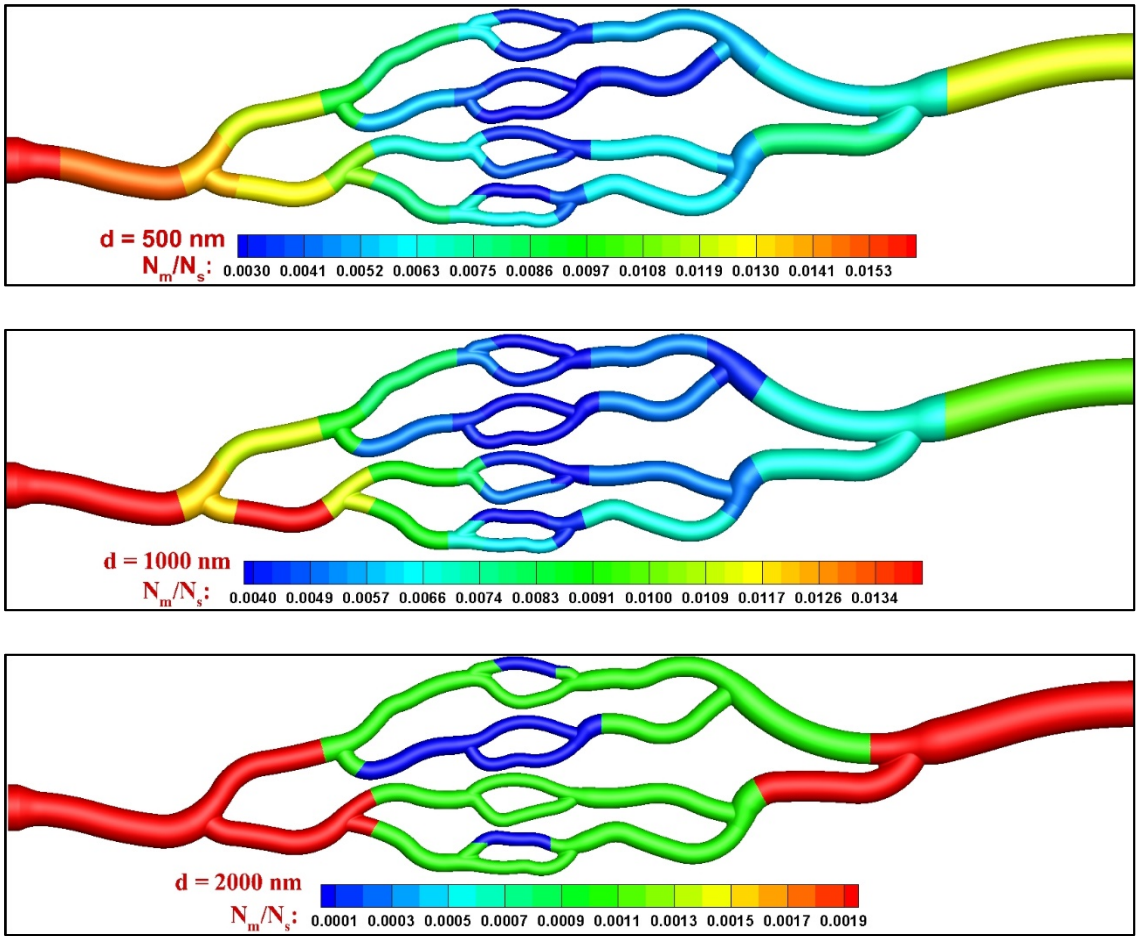

Figure 4.15: Contours of N_m/N_s in each segment in network C for the diameters under investigation.

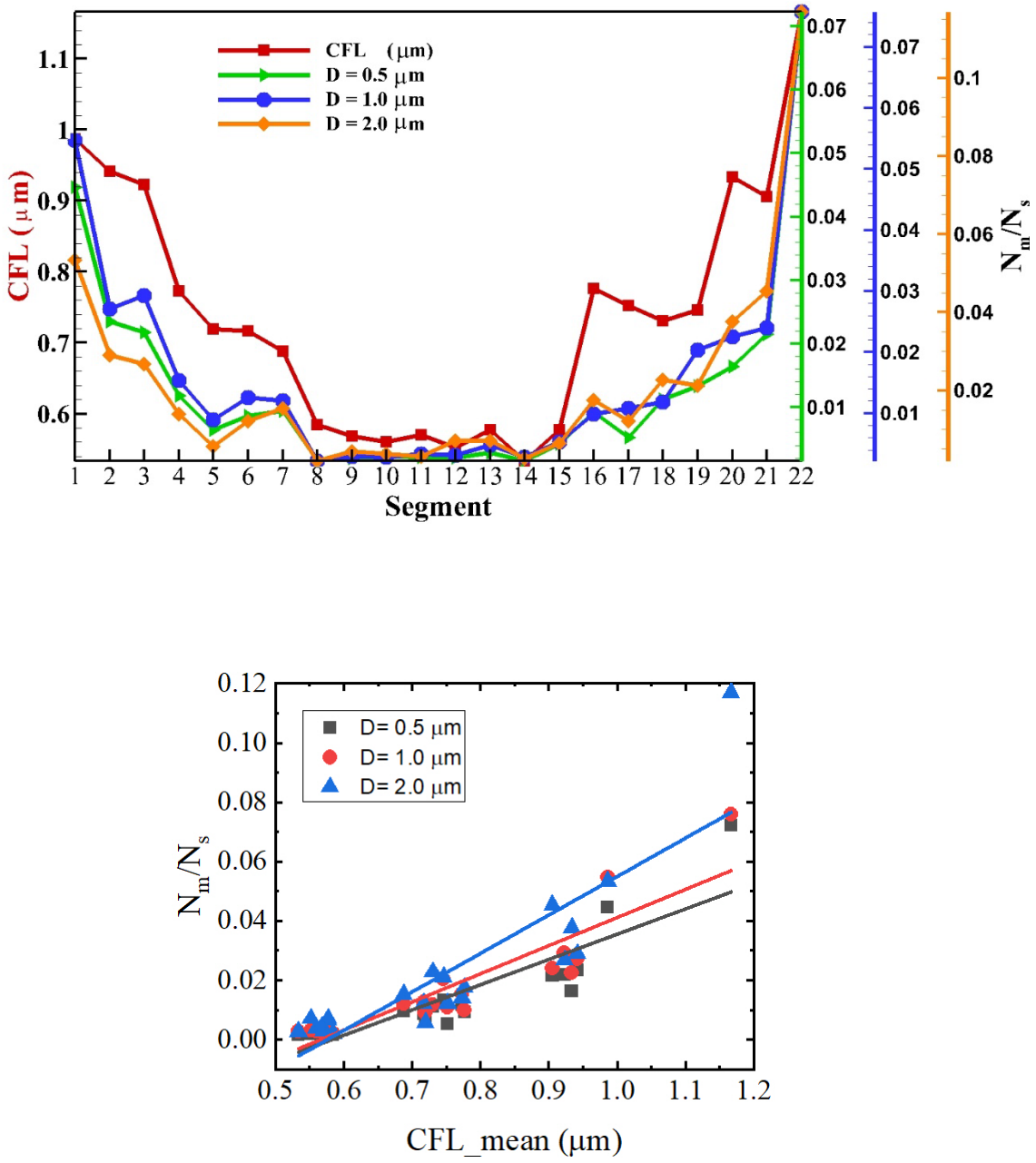

Figure 4.16: CFL thickness and margination fraction of NPs (N_m/N_s) are shown for different vessel segments in Network C (top). Also, shown CFL thickness versus N_m/N_s for the same network (bottom). The straight line is a linear fit through the data. Three lines for three diameters, d=0.5 μm (gray square), d=1.0 μm (red circle), d=2.0 μm (blue triangle).

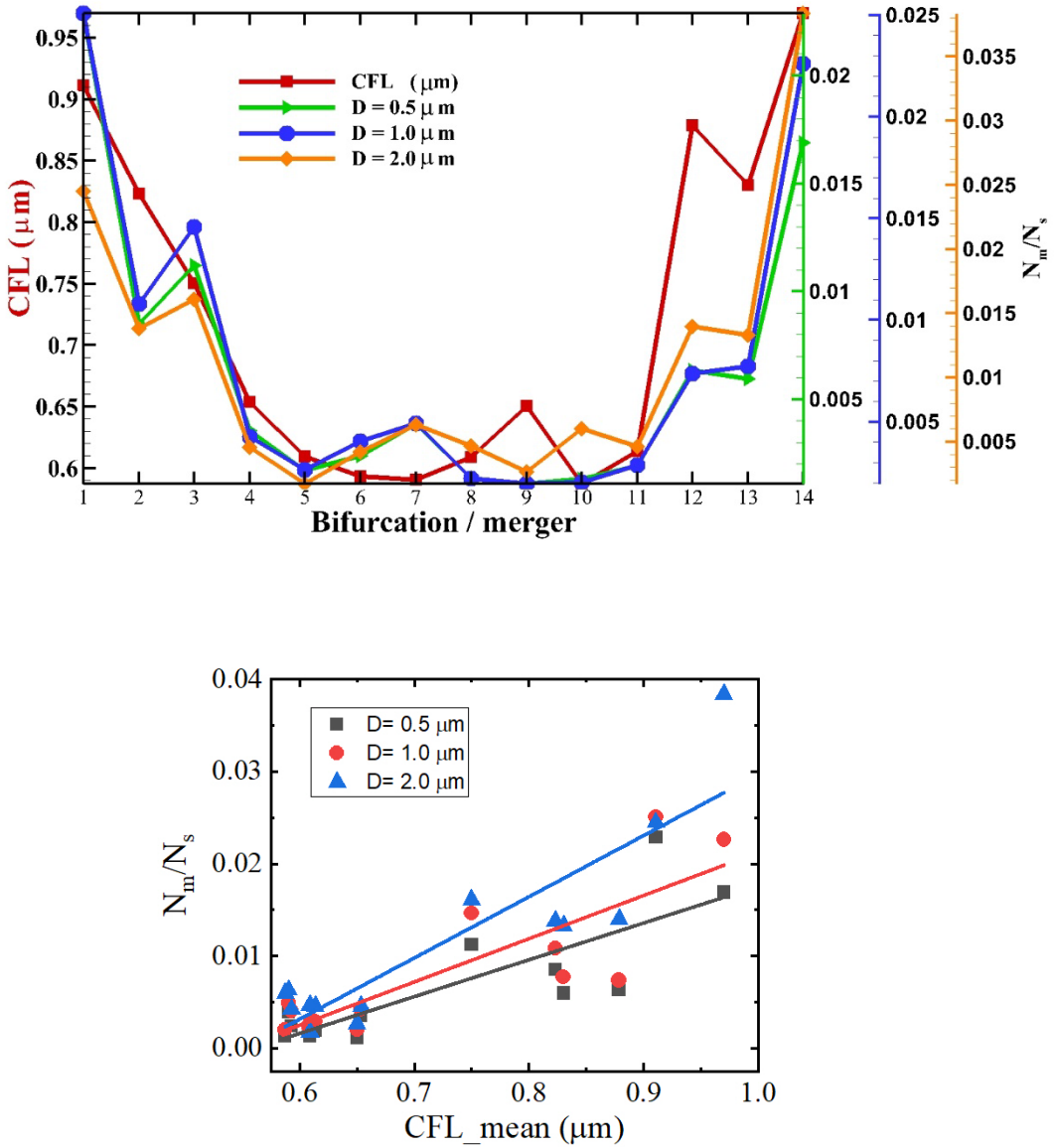

Figure 4.17: CFL thickness and margination of NPs (N_m/N_s) are shown for different bifurcation and merger segments in Network C (top). Also shown CFL thickness versus N_m/N_s for the same network (bottom). The straight line is a linear fit through the data. Three lines for three diameters, d=0.5 μm (gray square), d=1.0 μm (red circle), d=2.0 μm (blue triangle).

The other way of quantifying the heterogeneity is to consider the NP accumulation in different generations (hierarchy) of segments. For each segment type, arterioles, venules, bifurcations, and mergers, there is a generation number according to the topology of the network. See section 3.2.3 for details. Figures 4.18 to 4.20 show the surface area density of marginated NPs for networks C, B, and A respectively. The NPs accumulation increases with increasing generation number as in network C (network D behaves similarly). However, larger and more complicated geometries have a different behavior of heterogeneity. In geometries A and B, higher margination exists in the middle levels and less at the early and late levels. All of NP sizes behave similarly in a specific geometry. Also, zero hematocrit simulations show similar behaviors as of Ht = 25% (not shown). Thus, we conclude that this kind of heterogeneity is inferred by the geometry configuration itself.

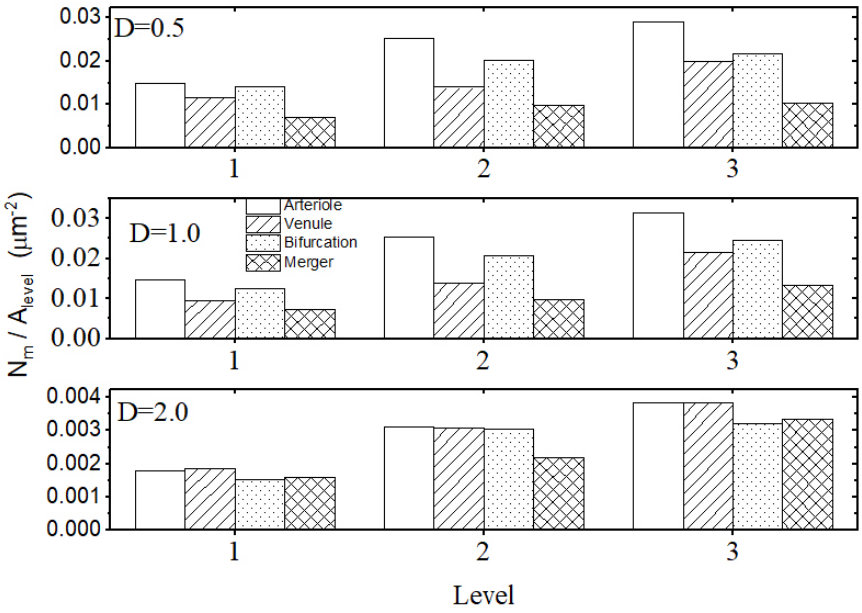

Figure 4.18: Marginated NP accumulation (per unit surface area for each level generation) presented as a function of segment generation level in network C.

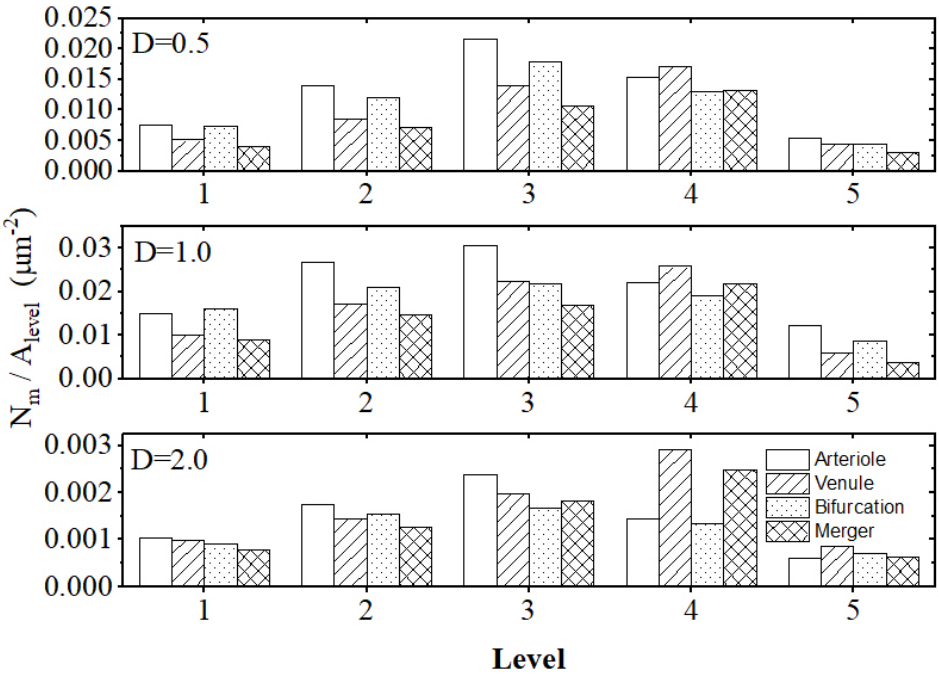

Figure 4.19: Marginated NP accumulation (per unit surface area for each level generation) presented as a function of segment generation level in network B.

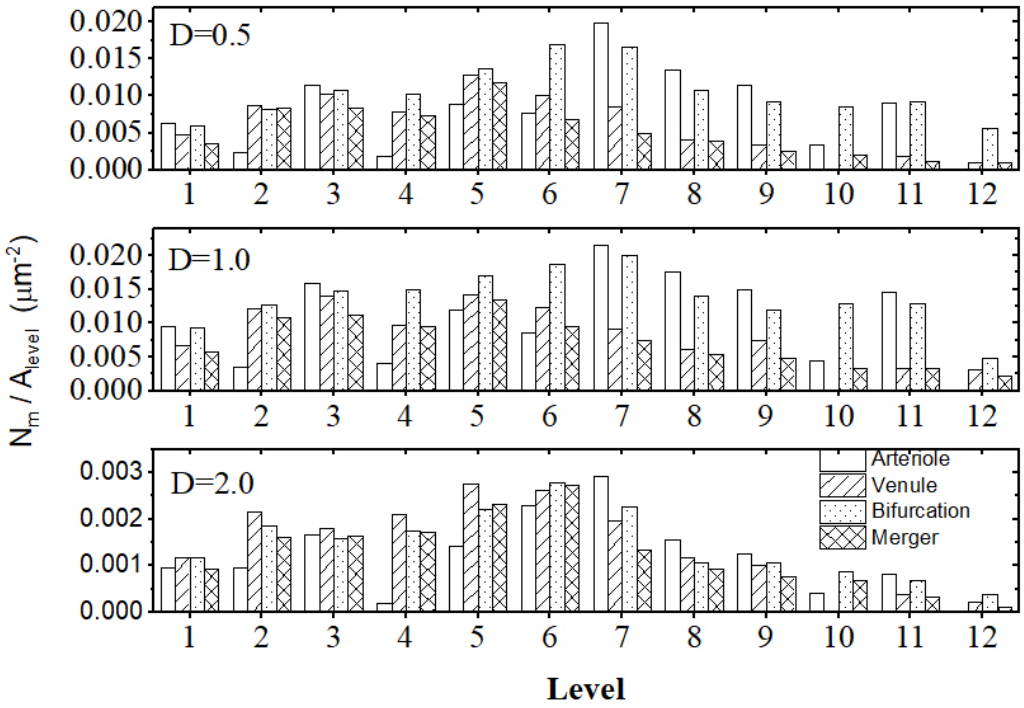

Figure 4.20: Marginated NP accumulation (per unit surface area for each level generation) presented as a function of segment generation level in network A.

4.2.3.2 Adhesion likelihood analysis

In this section, the heterogeneity of the likelihood of adhesion within several generations of a segment is presented. Figure 4.21 shows the adhesion likelihood area density of diameter 1.0 µm in network C. It is very clear that there is a variation of this density among sub-segment levels. All levels have varied adhesion likelihood starting from arterioles and bifurcations on the left, and the venules and mergers on the right of the figure. Figure 4.22 and figure 4.23 show the heterogeneity among levels in networks C and B. As we see in the margination analysis, the adhesion likelihood increases with increasing number of levels for network C where the less complicated direction of flow exists, while middle levels have higher adhesion likelihood within more complicated geometries as in B.

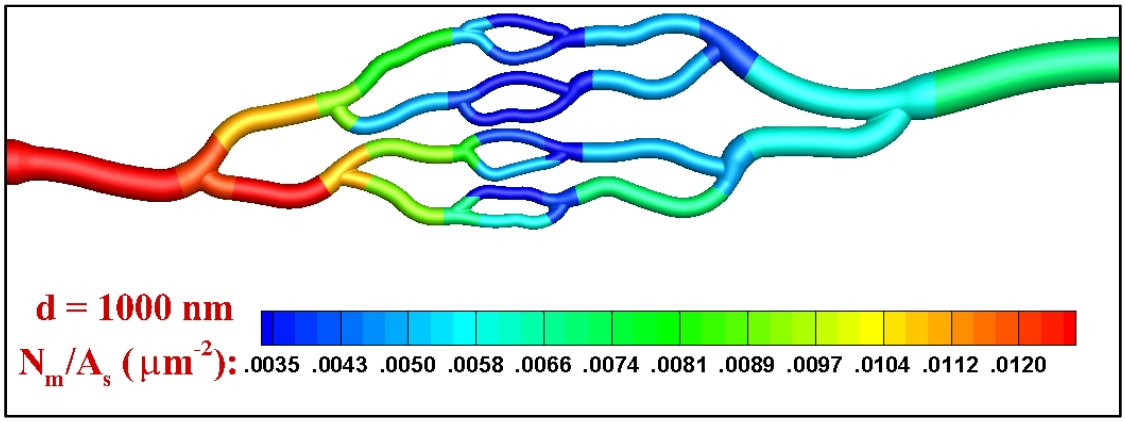

Figure 4.21: Contours of area density of adhesion likelihood (N_a/A_s) in each segment in network C for the diameter 1.0 µm.

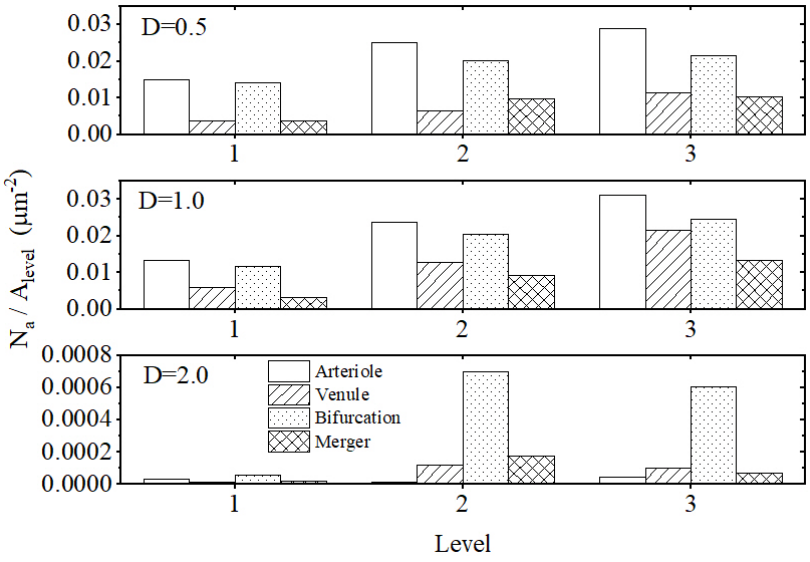

Figure 4.22: Adhesion likelihood of NPs (per unit surface area for each level generation) presented as a function of segment generation level in Network C.

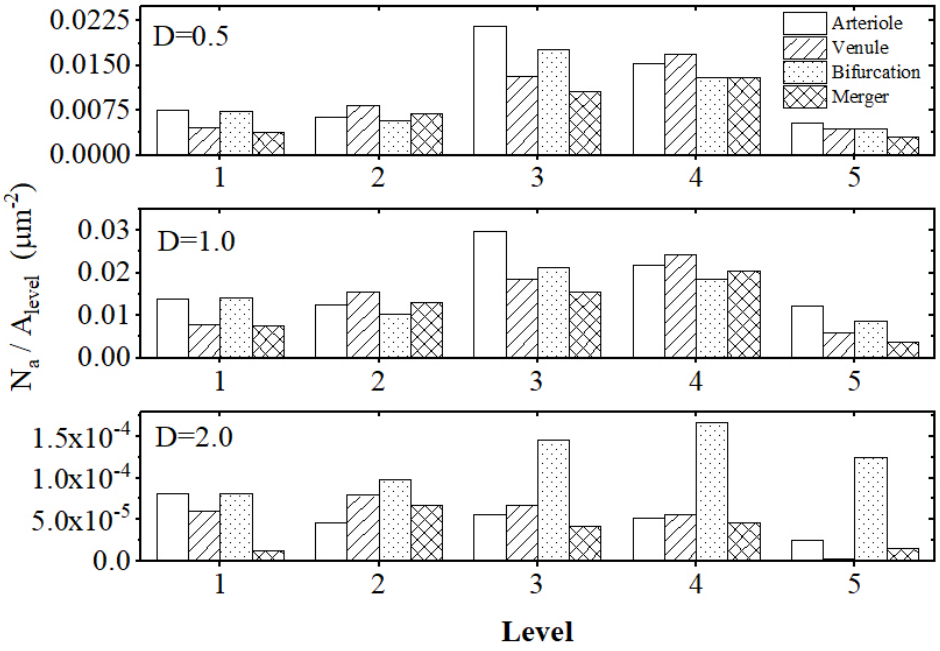

Figure 4.23: Adhesion likelihood of NPs (per unit surface area for each level generation) presented as a function of segment generation level in Network B.

4.3 Conclusions

Transport, margination, and adhesion likelihood of nanoparticles modeled as finite size rigid spherical particles are simulated in physiologically realistic microvascular networks with fully resolved flow dynamics of red blood cells. Particle sizes considered are 0.5 μm, 1.0 μm, and 2.0 μm. These particles are in two-way interaction with the flow field, boundaries, and RBCs. A particle is considered to be marginated when it has a surface portion or all of its body within the RBC-free layer. It is, however, allowed to move by the flow and can get out of the CFL. On the other hand, the particle is considered to be able to start adhesion if it comes within 650 nm from the vessel walls.

Overall, our results show that the finite-size NPs distribution is highly non-uniform across a network. This is similar to what we found in the tracer analysis. More specifically, for the margination the arteriolar and venular segments have the highest accumulation while the capillaries have the lowest. On the other hand, for the adhesion likelihood, arterioles and venules are favored over the capillaries which have the lowest. However, for the d=2.0 μm only, bifurcations show higher likelihood than the other segments. Margination is observed even when there are no RBCs, which indicates the importance of the network configuration on enhancing this phenomenon. RBCs' presence enhances the margination by about one order of magnitude. Even within each type of vascular segments, a strong heterogeneity is observed. In general, accumulation is shown to correlate with the CFL thickness as is the case for the tracer particles. Adhesion likelihood also behaves similarly to that of margination with regard to the sub-segment levels. On the other hand, for the case of Ht = 0, the margination is correlated to the ratio of CFL thickness to the segment radius. The margination and adhesion likelihood

throughout the generations of the various network segments have two different behaviors. In simple networks C and D, the accumulation increases with generation, while in more complicated network A and B, more accumulation is observed in the middle generations of a segment. This observation is for all particle sizes under study and for all Ht levels, which again, underline the role of the geometry of the network. Finally, irrespective of geometries and hematocrit, the accumulation of the marginated particles and the likelihood of adhesion both increase with increasing the size of the particle; so that, the biggest diameter studied here (2.0 μm) shows the highest margination and adhesion likelihood.

Chapter 5

Effect of Shape of Particles on their Margination and Adhesion Likelihood

5.1 Introduction

5.1.1 Objectives

In this chapter, we will study the margination and adhesion likelihood of finite size nonspherical nanoparticles (NPs) flowing with the blood in the capillary networks considered in this work. The main objective here is to understand the effect of NP shape on its margination. Margination is affected due to the way a non-spherical particle interacts with the RBCs and walls, in addition to their dynamics, while adhesion is affected due to an increased surface area and the number of ligand and receptors available on both surfaces. Ellipsoids are the most commonly studied shapes. **Oblate** and **prolate** shapes are considered in this study to understand how the deviation from the spherical shape affects margination and adhesion likelihood. The aspect ratio (AR) of the long to short diameters of the particles is chosen to equal to three. Also included in this study is the effect of hematocrit, where two levels are considered: **0%** and **25%**. Zero hematocrit case is used for isolating the effect of geometry from the effect of RBCs as we will see later in section 5.2.2. Also, as we did in chapter three for the tracer particles, it is

important to understand the effect of microvascular network geometry on the margination and adhesion likelihood of finite size ellipsoidal NPs. As we did with rigid spherical particles in chapter four, we will also investigate how the heterogeneity of particles accumulation alters when the effect of particle shape is included. Motivated by previous works, we will explore if oblate particles show increased margination over spherical and prolate particles.

5.1.2 Simulation setup

The finite sizes ellipsoidal particles considered here are in two-way interaction with the surrounding fluid. The flow regime is in Stokes flow ($Re \approx 0$) as capillary networks are considered [99]. Following the definition of the Stokes number, St, in chapter three, it is clear that this value is very small $\sim 10^{-5}$ so that NPs response time is still much faster than fluid response time. Brownian motion of these nanoparticles are also not included in the analysis since the Peclet number, Pe, is of the order of 10^3 and implies that Brownian effects are small compared with the convective effects. Similar to spherical particles in chapter four, the effects of Brownian motion and inertia on the viscosity are negligible for $Pe \approx 10^3$ and $Re = 0$, respectively [101]. Also, for such low volume fractions of particles distributed in our networks (up to 0.01), the dilute suspension relation of Einstein is also applied here with the value of Einstein coefficient B interpolated from the random initial orientation curve given in [102]. This value is about 2.8 for our used ellipsoidal particles aspect ratio which is equal to 3. This indicates that the increase of apparent viscosity due to particles addition is still very small (0.028).

Due to computational restrictions, the total number of supplied particles in the network is restricted as we discussed in chapter four when we investigated finite size spherical particles. In this chapter, we keep the total number of supplied particles inside any network considered to 100. All analyses are collected after the transient period of margination of NPs is bypassed, so that a quasi-steady-state is reached.

Here, we consider a particle to be marginated if any portion of its surface lies within the CFL. That is because hydrodynamic and physiological interactions between a particle surface and the wall may be initiated even if the particle centroid is not within the CFL, but a portion of its surface is. Hydrodynamic interaction in Stokes flow is long-range and acts over many particle diameters. Physiologically, the ligand-receptor interaction can occur when the particle surface is a few hundred nanometers away from the wall.

On the other hand, and similar to chapter four, we choose a specific distance to identify that a particle is likely to adhere. That is, if a particle surface comes within 650 nm of the wall, we identify this NP as adhered. There are 16 simulations done for the analyses in this chapter. As we mentioned in chapter three, the computational cost is at most about 9~10 hours/one dimensionless time unit.

5.2 Results

5.2.1 The behavior of margination and adhesion likelihood of ellipsoidal NCs through various segments of the networks

5.2.1.1 Margination analysis

Figures 5.1 to 5.4 present snapshots showing the distribution of RBCs and ellipsoidal particles at a specific time of each simulation. Care must be taken here, as the figures show the instantaneous particle distribution at a specific instant of the simulations only. As noted before, particles can marginate but later leave the near-wall region.

From heterogeneity point of view, analysis of margination of rigid ellipsoidal particles in these simulations shows similarity with the previous point- and finite-size spherical particles discussed in previous chapters. Figure 5.5 and figure 5.6 show marginated particle distribution in five different segments of the vasculatures (arterioles, capillaries, venules, bifurcations, and mergers). Figure 5.5 shows (N_m/N_s) ratio, while figure 5.6 shows (N_m/N_{tm}). Note that in these plots, we do not distinguish between different generations of vessels. Plots for the spherical particles of equivalent size (d=2.0 μm) is repeated here for comparison purposes.

The margination of particles distribution is non-uniform across different regions within the same network. Relatively higher margination is observed in the venular and arteriolar regions while much less margination is observed in the capillaries. Bifurcations and mergers have an intermediate amount of margination between venules and capillaries. These margination trends are valid for all four different vasculatures simulated; therefore, we conclude that the predicted non-uniformity in particle accumulation would also occur in any microvasculature in vivo.

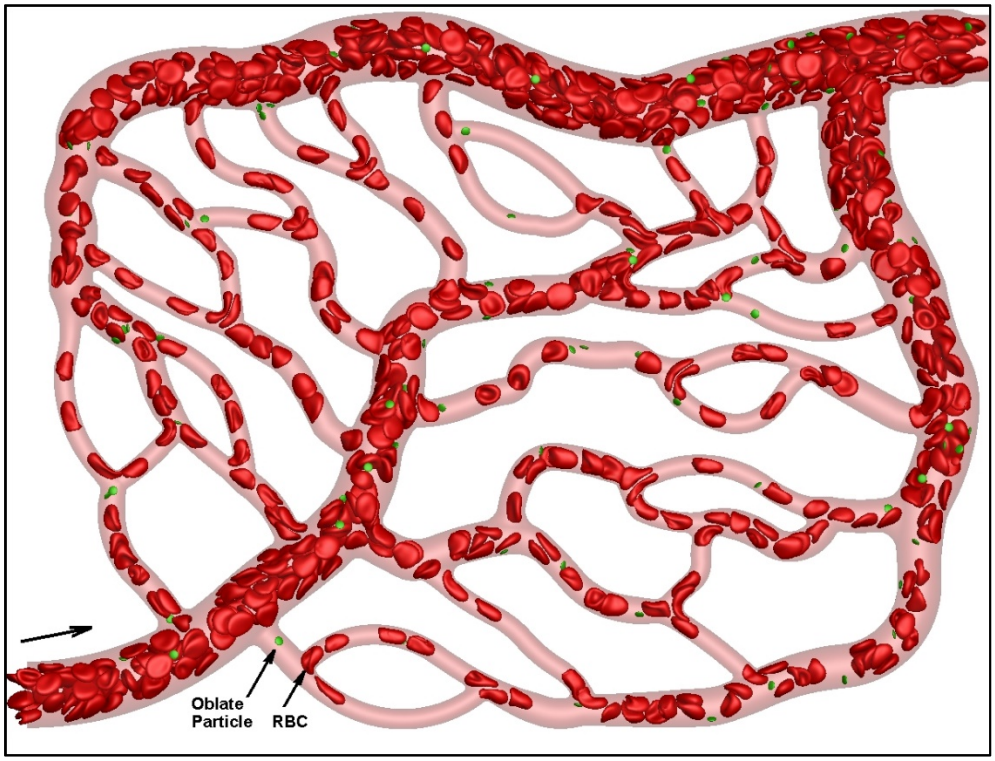

(a) Oblate

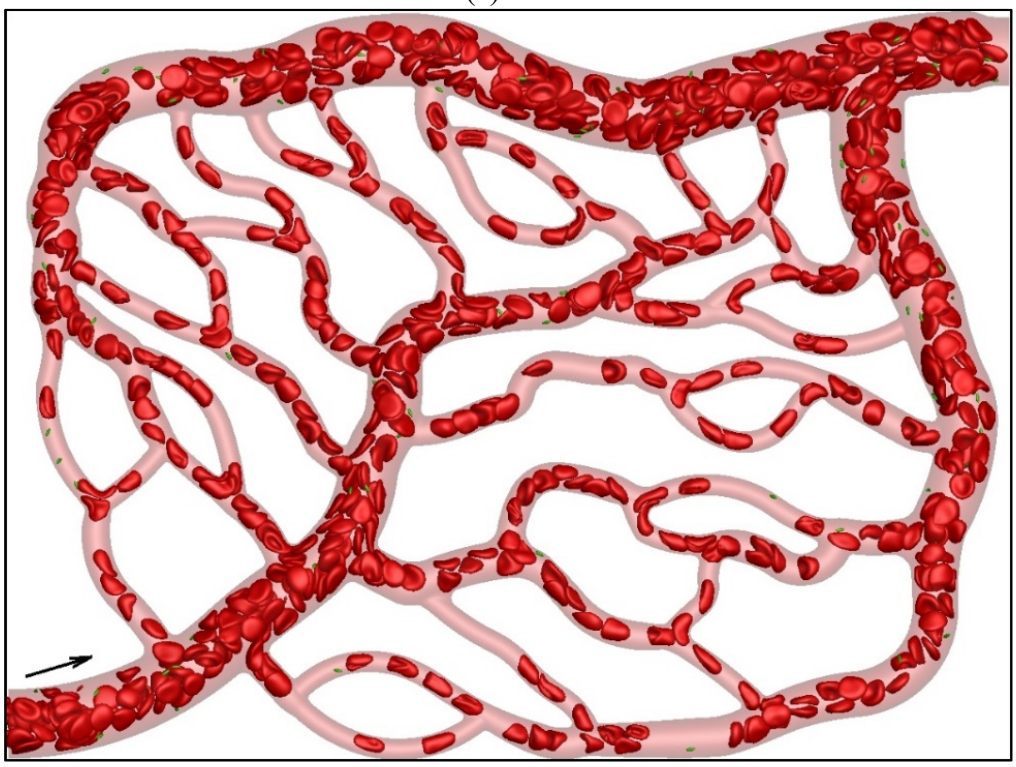

(b) Prolate

Figure 5.1: Snapshots of a time instant for particle shape (a) Oblate and (b) Prolate simulations in network A at Ht = 25%. Hereafter NPs are shown in green, and RBCs in red.

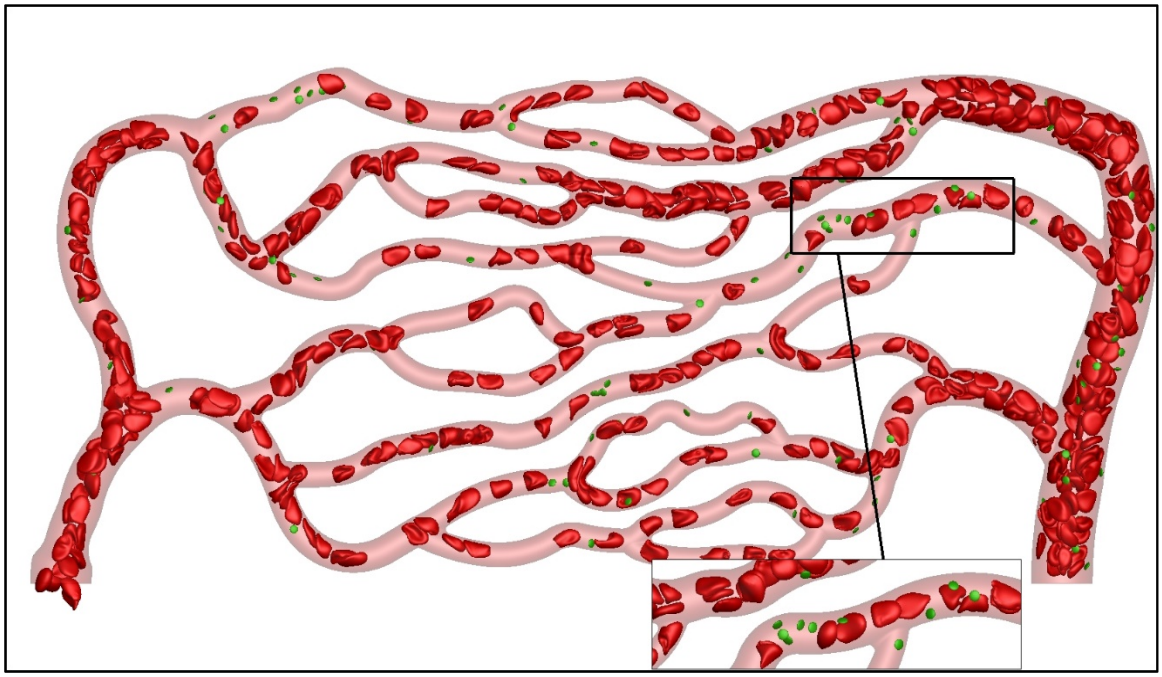

(a) Oblate

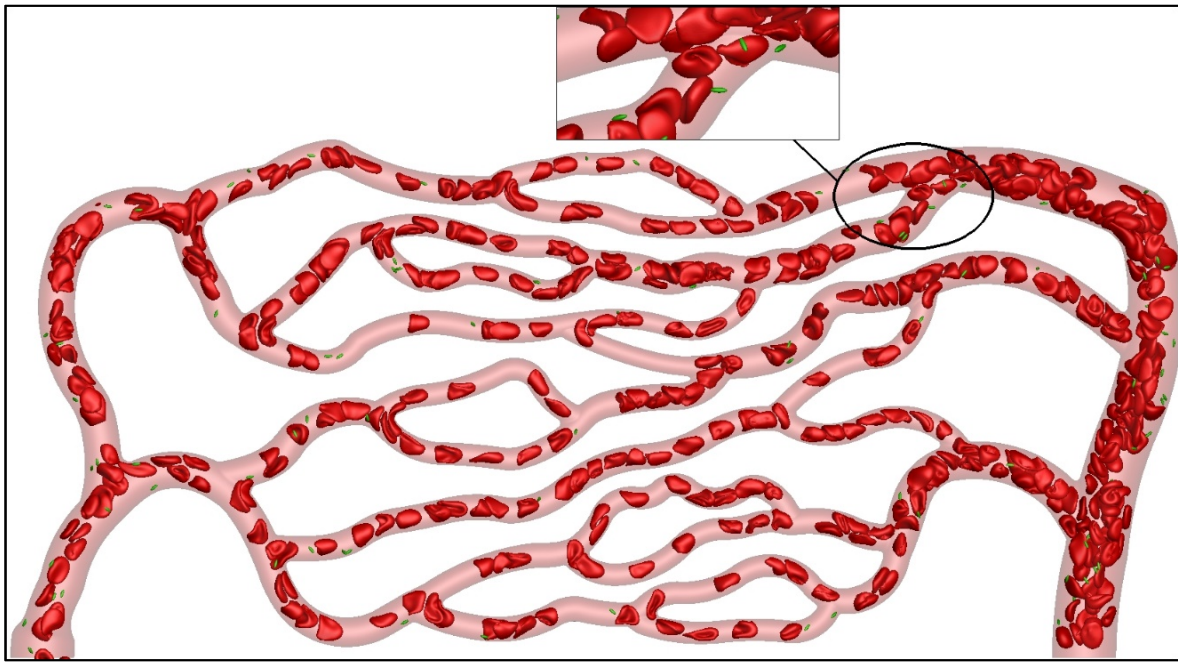

(b) Prolate

Figure 5.2: Snapshots of the final time instant for particle shape (a) Oblate and (b) Prolate simulations in network B at Ht = 25%.

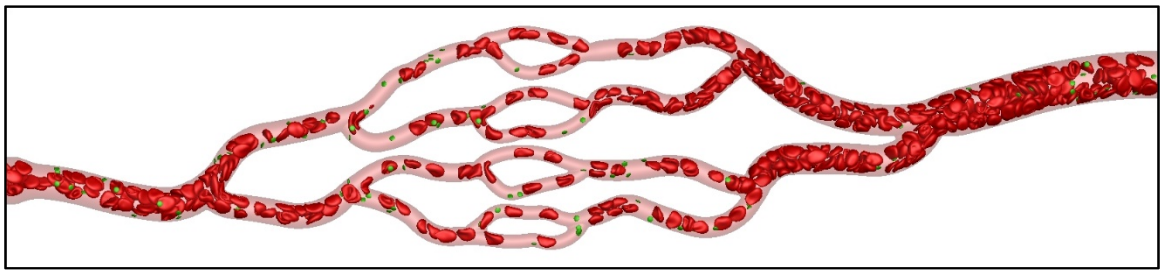

(a) Oblate

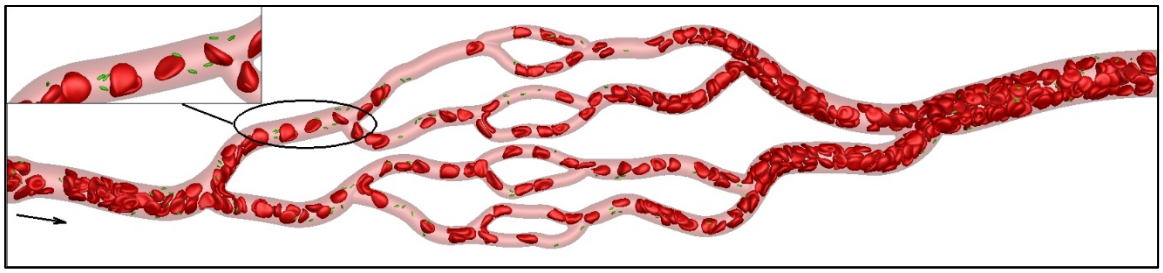

(b) Prolate

Figure 5.3: Snapshots of the final time instant for particle shape (a) Oblate and (b) Prolate simulations in network C at Ht = 25%.

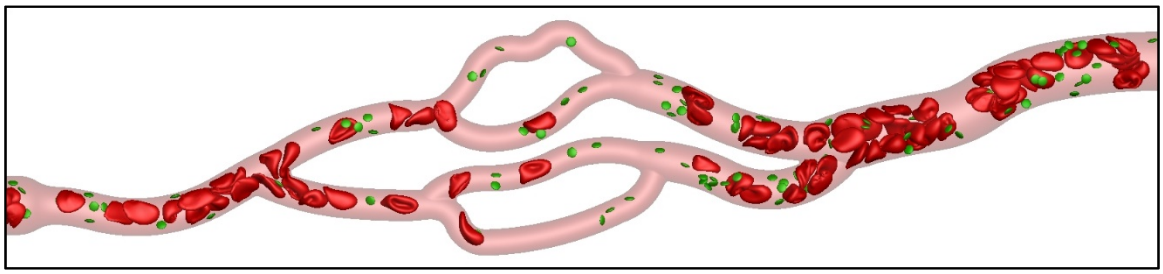

(a) Oblate

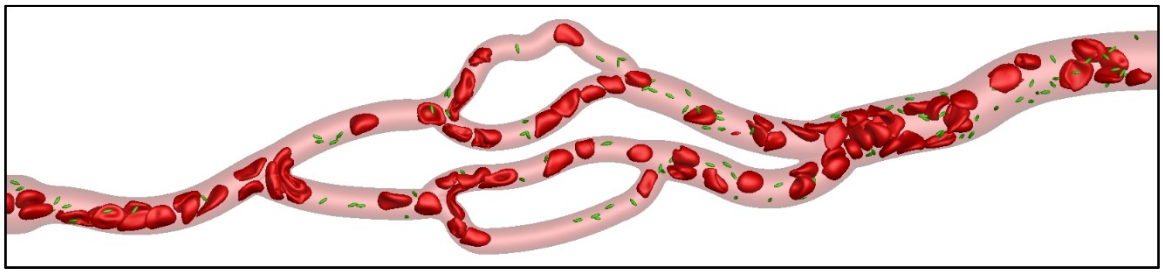

(b) (b) Prolate

Figure 5.4: Snapshots of the final time instant for particle shape (a) Oblate and (b) Prolate simulations in network D at Ht = 25%.

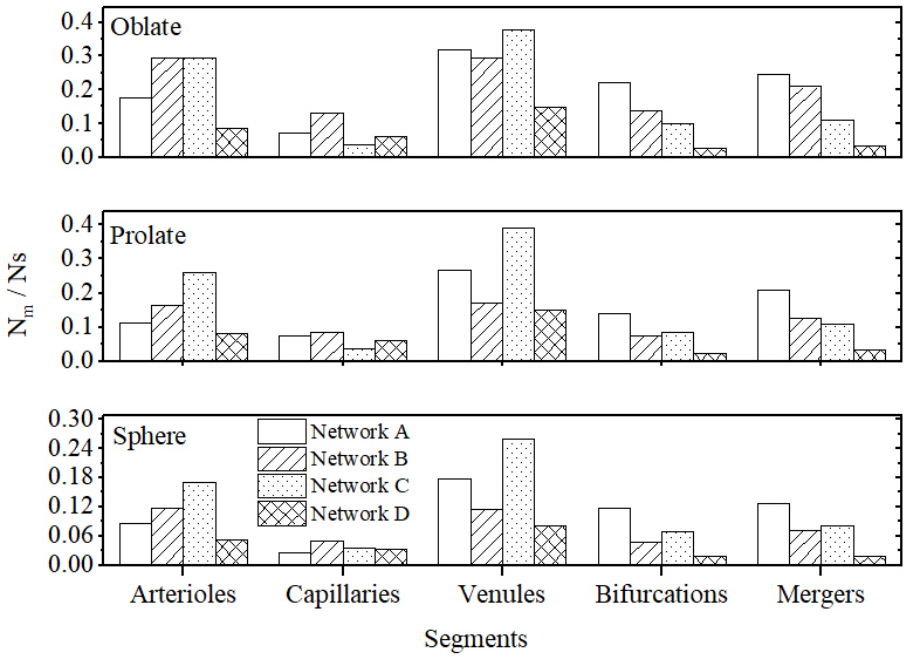

Figure 5.5: NP distribution in different segment for the three shapes, oblate, prolate, and sphere. Shown is the ratio of the number of marginated NPs to the total number of supplied NPs (N_m/N_s) for the Ht = 25% simulations.

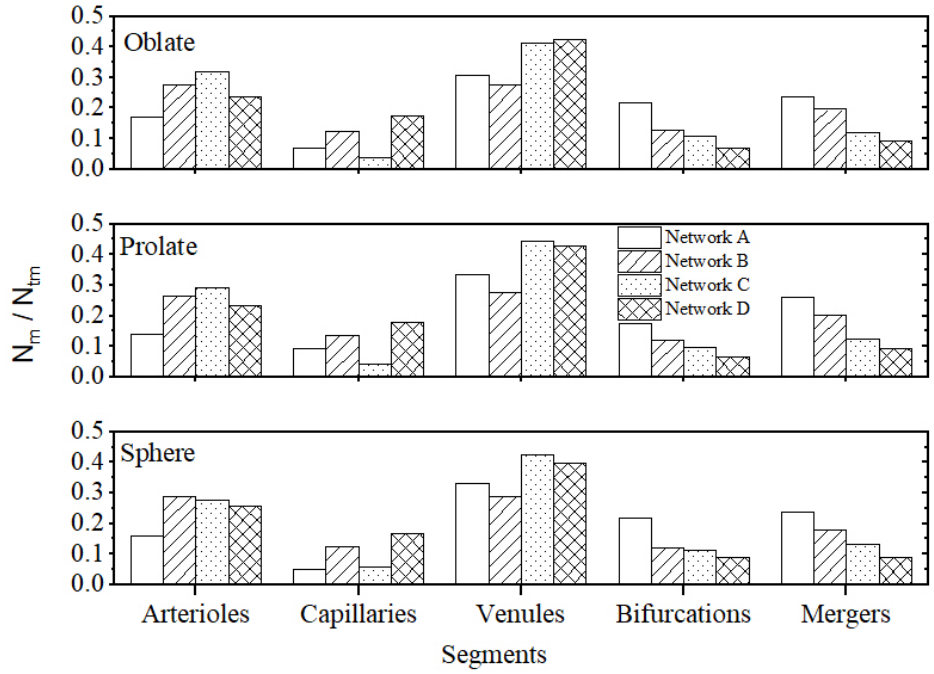

Figure 5.6: NP distribution in different segment for the three shapes, oblate, prolate, and sphere. Shown is the ratio of the number of marginated NPs in each segment to the total number of marginated particles in the entire networks, N_m/N_{tm} for the Ht=25% simulations.

This heterogeneity is also observed as in the previous analysis of tracers and rigid spherical particles across the segments of the investigated networks. Therefore, we conclude that irrespective of the size and shape of particles, and the interaction effect between particles and suspending fluid, the relative amount of margination of particles and its heterogeneity is mainly decided by the network configuration. This is not the case of straight tube/channel flow when particle characteristics play a substantial role on the margination level.

In figure 5.7, we scale the number of particles marginated by the surface area of each segment (N_m/A_s) to quantify the effect of the surface area of a network segment. The actual number of particles marginated will depend on the vessel or segment surface area. For the margination simulations of rigid ellipsoidal particles, the accumulation per area is more uniform than those in figure 5.5 and figure 5.6, with the capillary segments having relatively less margination.

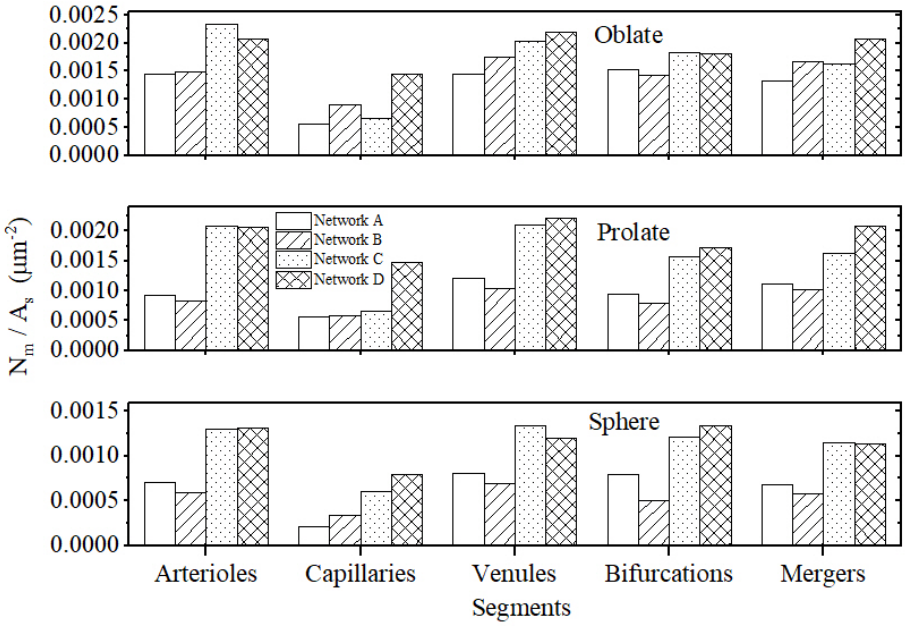

Figure 5.7: NP accumulation of marginated rigid ellipsoidal particles within various segments per segment surface area (N_m/A_s) for Ht = 25%.

5.2.1.2 Adhesion likelihood analysis

Now we analyze the adhesion likelihood for finite-size ellipsoidal rigid particles under investigation. Figure 5.8 and figure 5.9 present the ratios of N_a/N_s and N_a/N_{ta}. Here N_a/N_s is the ratio of particles likely adhered to the total supplied particles in the network, and N_a/N_{ta} is the ratio of particles likely adhered in each segment to the total number of the particles likely adhered in the network. In both figures, the behavior of the d=2.0 μm spherical particle is different from the others. For the ellipsoidal particles, the adhesion behavior is similar to the margination. That is, a higher adhesion likelihood exists in the arterioles and venules, but the 2.0 μm spherical particle has the highest adhesion likelihood within bifurcation, similar to the tracer particles as we mentioned in chapter four. This is a noticeable difference we observe here between ellipsoidal particles and their equivalent spherical ones.

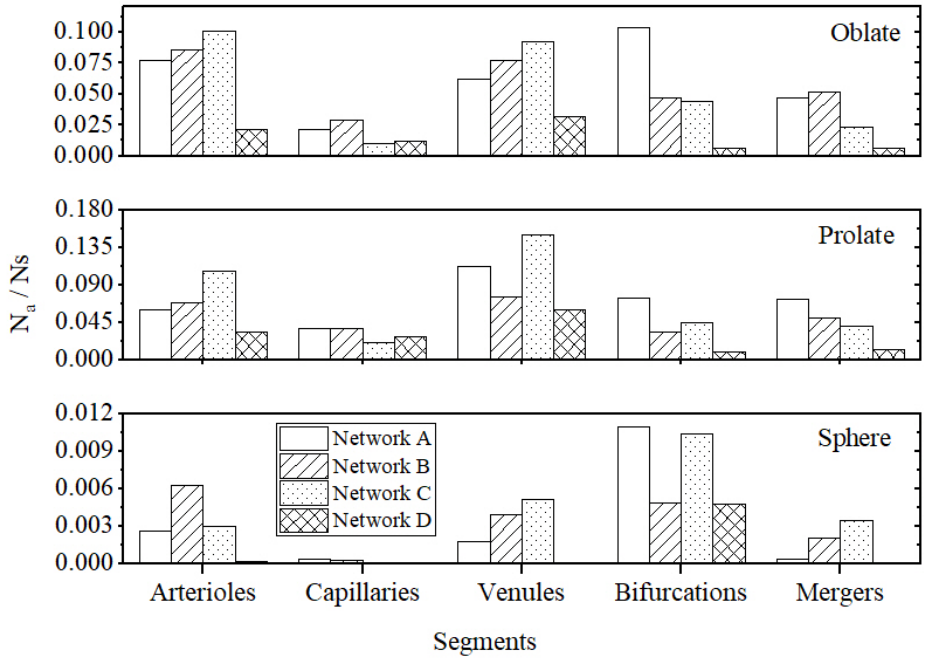

Figure 5.8: NP distribution in different segment for the Ht = 25% simulations. Shown is the ratio of the number of anticipated adhered NPs to the total number of supplied NPs (N_a/N_s).

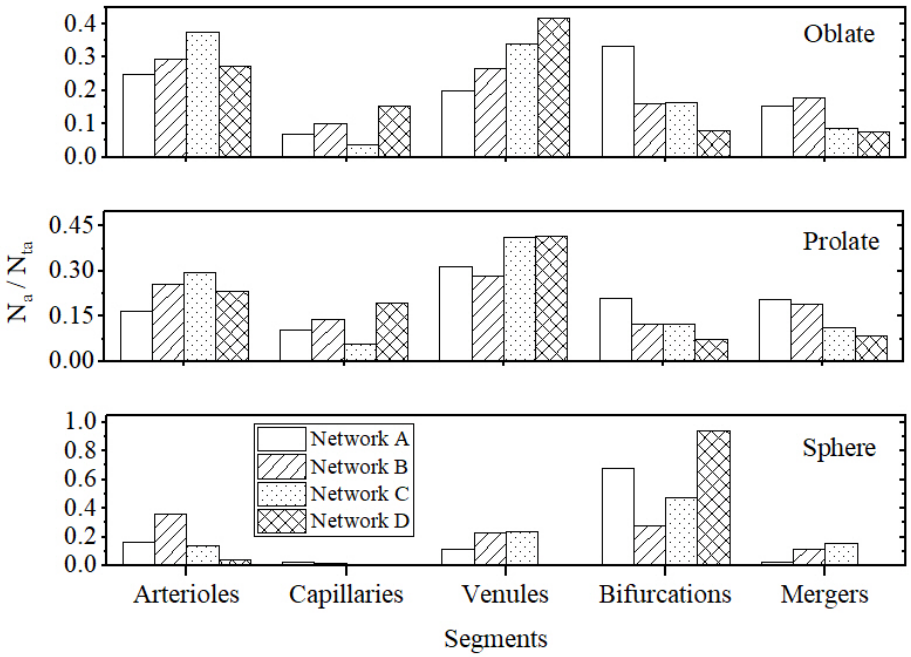

Figure 5.9: NP distribution in different segment for the Ht = 25% simulations. Shown is the ratio of the number of anticipated adhered NPs in each segment to the total number of anticipated adhered particles in the entire networks, N_a/N_{ta}.

5.2.2 Effect of geometry, hematocrit, and particle shape on the margination of NCs

We now investigate the reasons behind the observed non-uniform accumulation of ellipsoidal NPs, and the effect of geometry of the network and hematocrit.

As we did in the previous chapters, we can isolate the influence of the network geometry and that of the RBCs on the NPs margination with the simulations of Ht = 0. The total marginated NPs as a fraction of supplied NPs and scaled by area ($N_{tm}/N_s \cdot A$) over an entire network for all four networks and two tested shapes are shown in figure 5.10.

As we saw in the different size particles analysis, the top chart of this figure shows that even with the absence of RBCs, there is a margination in the networks, which is not the case in the straight tube. This indicates the importance of the network topology and morphology on ellipsoidal shapes. Previous works, see section 1.3.2, indicate that for

Ht=0, the particles will not drift to the walls but oscillate with the flow in simple straight tube configuration. The effect of RBCs is clearly shown in the lower bar chart in figure 5.10, where margination increases by about one order of magnitude in all networks and for both oblate and prolate shapes in our study.

Figure 5.10 clearly shows that irrespective of the geometry and Ht levels, the accumulation of the marginated ellipsoidal particles is better than the equivalent spherical ones, and that, the oblate shape gives the most efficient margination behavior. This is more clearly observed for more complex networks A and B. On the other hand, in simpler geometries (C and D), the effect of both oblate and prolate on enhancing margination is similar. The behavior of particle margination between complex and simple geometries suggests that there is an effect of the network topology on how ellipsoidal particles marginate. However, both shapes show enhancement over the spherical counterpart which is also observed for simpler geometries, as mentioned in previous works, section 1.3.2.

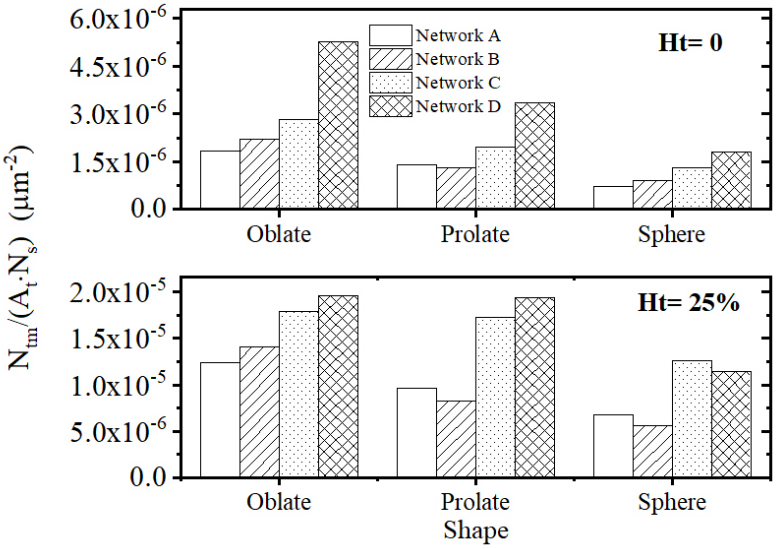

Figure 5.10: Ratio of total marginated NPs to supplied NPs scaled by area of the network ($N_{tm}/N_s.A$) for different Ht and particle sizes.

As noted before, the CFL has a higher thicknesss in venular segments compared to others, as shown in figure 3.15. As the RBCs come out of two feeding vessels into a venule, they usually do not fill the entire cross-section causing an increase in the cell-free layer, and the increased CFL thickness increases the possibility of NPs margination. It is evident that the margination levels shown in figure 5.5, and figure 5.6 follow the CFL distribution in figure 3.15. Also, as we saw for margination of rigid particles in capillaries, the train-carts manner of RBCs-NPs exist for ellipsoidal particles due to the RBCs lingering in precapillary bifurcations. That is, a particles/cluster of particles without RBC followed by RBC or RBCs. Unlike the spherical particles, the TC phenomenon is also accompanied by particles-RBCs coupling where the ellipsoidal particles are close to the wall. Figure 5.11 clarifies this phenomenon. This figure also shows another mechanism associated with elliptical particles. In this mechanism, a particle-wall interaction causes the marginated particle to rotate along the axis parallel to the wall to form a rolling motion along the wall.

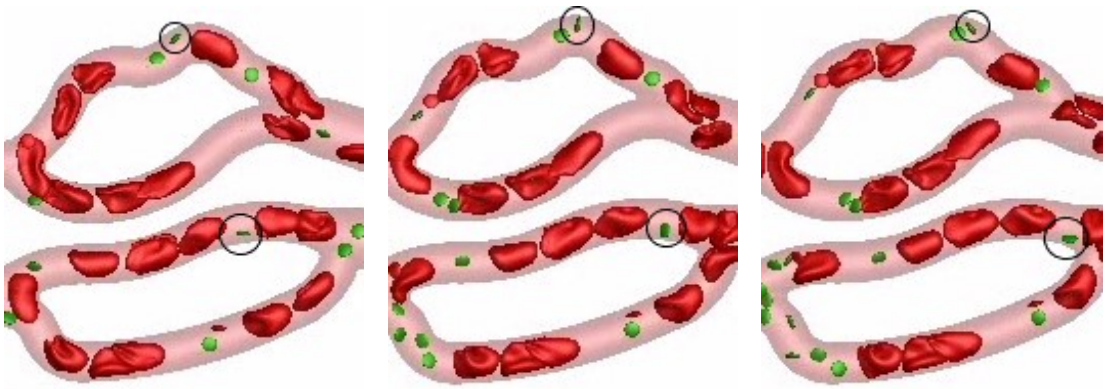

(a) (b) (c)

Figure 5.11: Motion of particles and RBCs within capillaries in a train-carts (TC) manner, with two particles experiencing rolling motion along the wall. Figures a to c are successively presented in time.

The rolling motion is different from the tumbling motion of these particles within the flow which plays an essential role to make these particles disperse and marginate faster than spherical counterparts. Together, these motions need further analysis to understand the effect of these particles dynamics on their dispersion, margination, and adhesion which is beyond the aims of the current work.

We further elaborate the geometry effect in the absence of RBCs by considering the NP distribution in different segments of a network as shown in figure 5.12, where the ratio N_m/N_s is plotted for Ht = 0. This figure shows that in the absence of the RBCs, there is a reduced non-uniformity in the distribution of marginated ellipsoidal NPs compared to spherical particles. However, the distribution of marginated ellipsoidal particles in Ht = 0 simulations shows a relatively low level in the mergers. Additionally, some vessels have higher margination than bifurcations. This is not observed in Ht = 25% for the same scaling. In figure 5.13 we present marginated particles in each segment scaled by the area of that segment for Ht = 0. Compared to figure 5.12, two observations can be drawn. First, the non-uniformity observed for Ht = 0 for different sizes also exists here for Ht =0. That is, low margination exists in venules and mergers, while higher margination exists in arterioles, capillaries, and bifurcations. Second, the two scalings (N_m/N_s) and (N_m/A_s) have now different degree of heterogeneity of ellipsoidal particles for Ht = 0. Overall, we can still say that the heterogeneity in Ht = 0 simulations based on area density is similar for both spherical and ellipsoidal particles. It is clear that the scaling N_m/N_s yields more uniformity. Accordingly, we can say that irrespective of geometry effect, the ellipsoidal particles tend to marginate in various segments with the same potential. This is not the case observed for spherical particles.

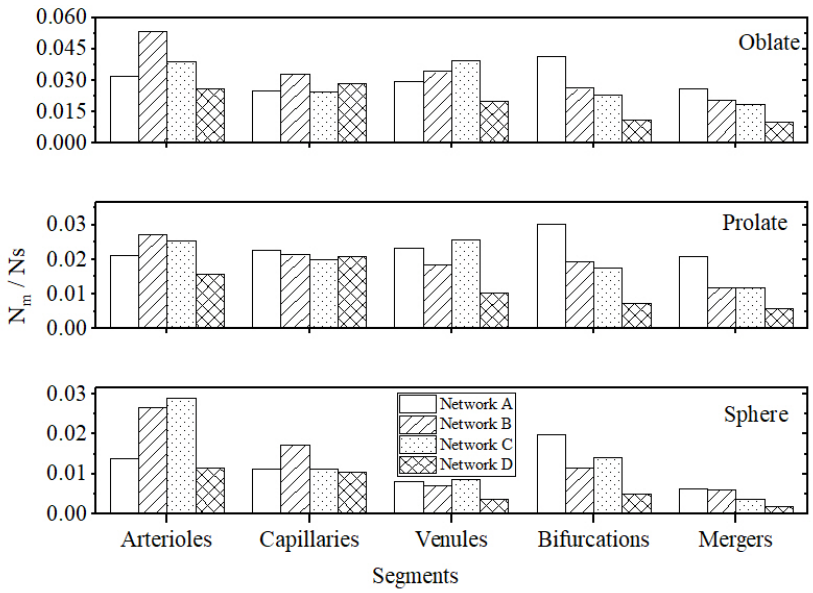

Figure 5.12: Segment-wise distribution of NPs fraction (N_m/N_s) at Ht = 0 to isolate the geometry effect.

Going back to figure 5.13, and comparing to Ht = 25% case, the bifurcation regions for Ht = 0 show higher margination. This was also observed for spherical particles also; consequently, we can say that this behavior is associated with finite size (≥ 500nm). We again refer to the mechanism that is responsible for increasing/decreasing the margination at the bifurcation. That is, RBCs tend to push particles toward walls laterally and remove them from the core. As a result, very few particles are expected to marginate at the bifurcation apex for Ht = 25% compared to Ht = 0. Therefore, for Ht = 0, particles on the core of the feeding vessel is not drift laterally and hit the bifurcation apex. The velocity of these particles near the vessel centerline is high compared to near wall velocity. Accordingly, the interaction with apex on the bifurcation is enhanced.

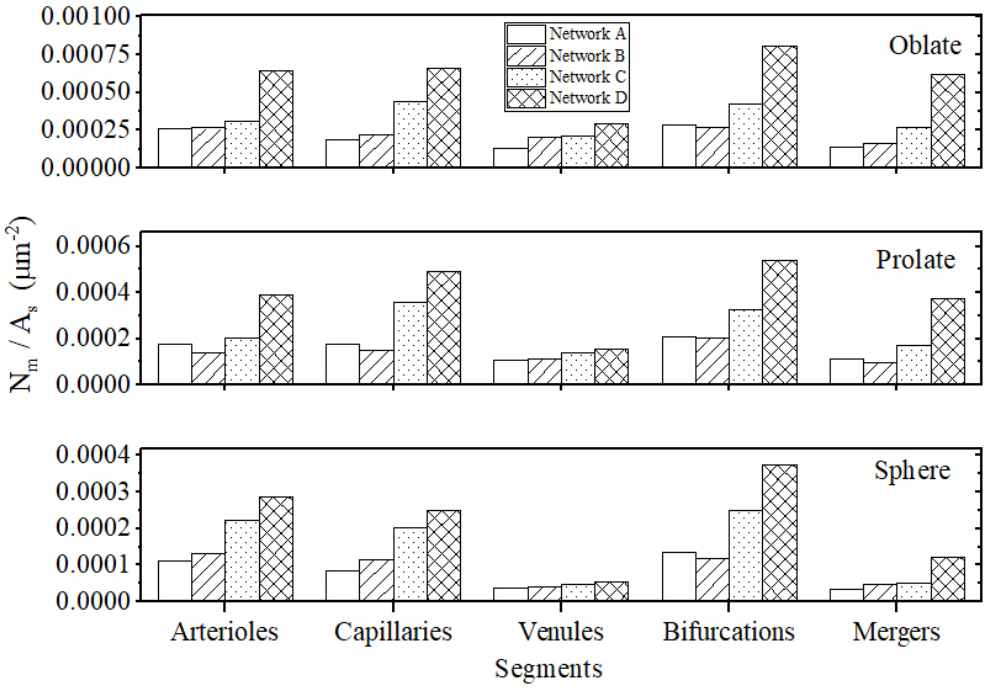

Figure 5.13: Segment-wise distribution of area density of NPs (N_m/A_s) at Ht = 0 to isolate the geometry effect.

Similar to the finite size spherical particles at Ht = 0, the proportionality of area density for margination is found to be correlated to the ratio of CFL thickness divided by the radius of the segment. It is clear that the behaviors of margination in figure 5.13 are following the criteria (2×CFL / d), where the minimum values for this ratio are in venules, and the maximum is in the capillaries.

5.2.3 Heterogeneity of margination and adhesion likelihood of ellipsoidal NCs throughout various vessels and bifurcations generations

5.2.3.1 Margination analysis

The overall picture that arises in the analysis above is that margination is highly non-uniform, with the relatively higher margination in the arteriolar and venular segments compared to lowest in the capillaries. Within each one of the five groups discussed before, there is also a strong heterogeneity when different locations in a network are considered. This is shown in figure 5.14 where color contours show the number density of marginated particles scaled by area for each segment in network A. The heterogeneous distribution is evident here for both shapes where some arterioles and venules have noticeably higher marginated particles than others.

As before, heterogeneity at segment-level is also correlated to the CFL thickness. To quantitatively show the correlation, we plot these two quantities in figure 5.15 (top) for different vessels (artery, capillary, and venule) in network A. Also, shown is a plot of N_m/A_s versus CFL thickness (bottom). In general, N_m/A_s increases with increasing CFL thickness, thereby suggesting a positive correlation between the two.

Figure 5.16 demonstrates a similar positive correlation between the CFL thickness and marginated ellipsoidal NPs in bifurcations and mergers. This again underscores the major role of network topology on the margination heterogeneity of the ellipsoidal particles among various segments.

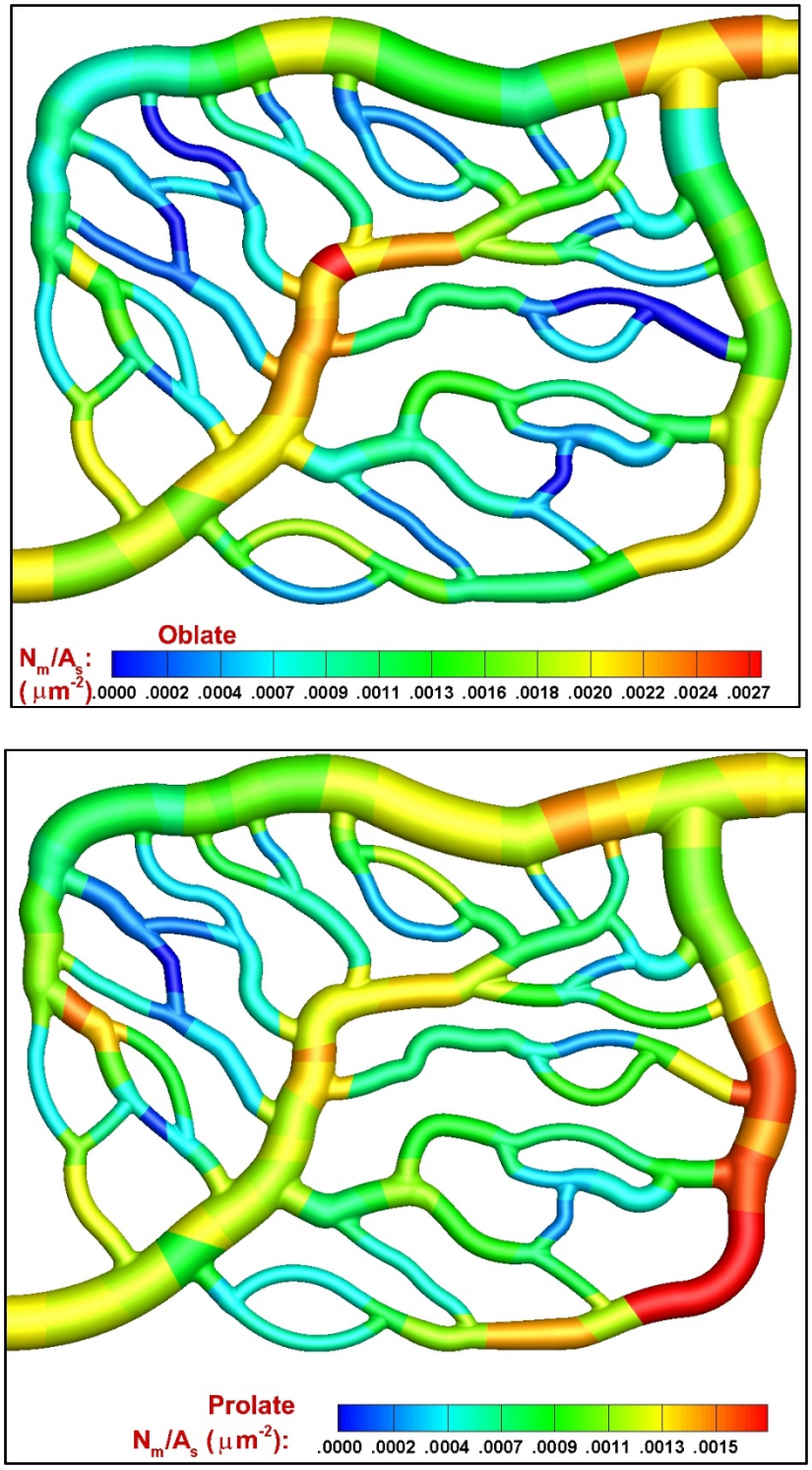

Figure 5.14: Contours of margination area density (N_m/A_s) in each segment for network A.

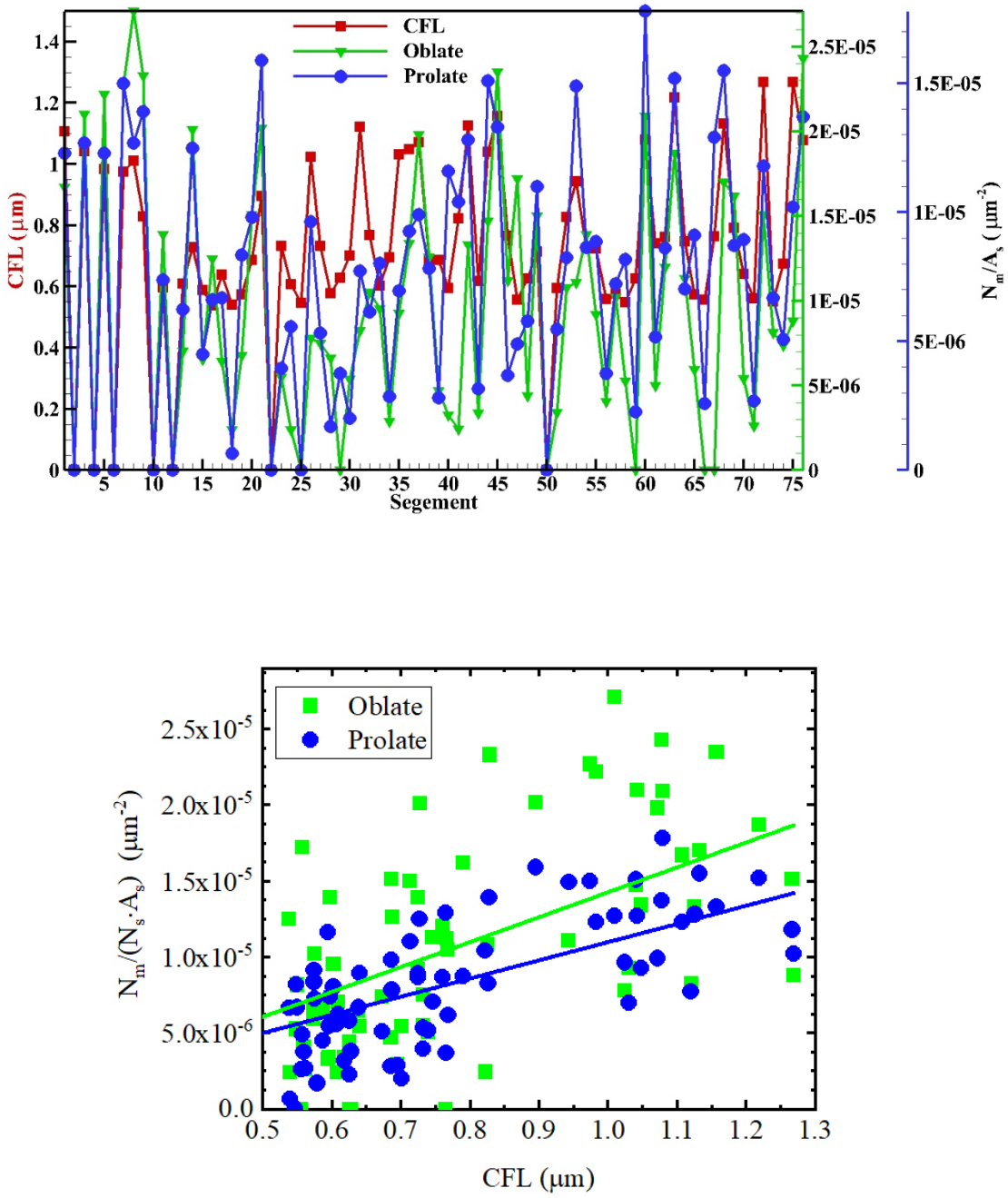

Figure 5.15: CFL thickness and area density of marginated NPs (N_m/A_s) are shown for different vessel segments for Network A (top). Also, shown CFL thickness versus N_m/A_s for the same network (bottom). The straight line is a linear fit through the data. Oblate (green square), and prolate (blue circle).

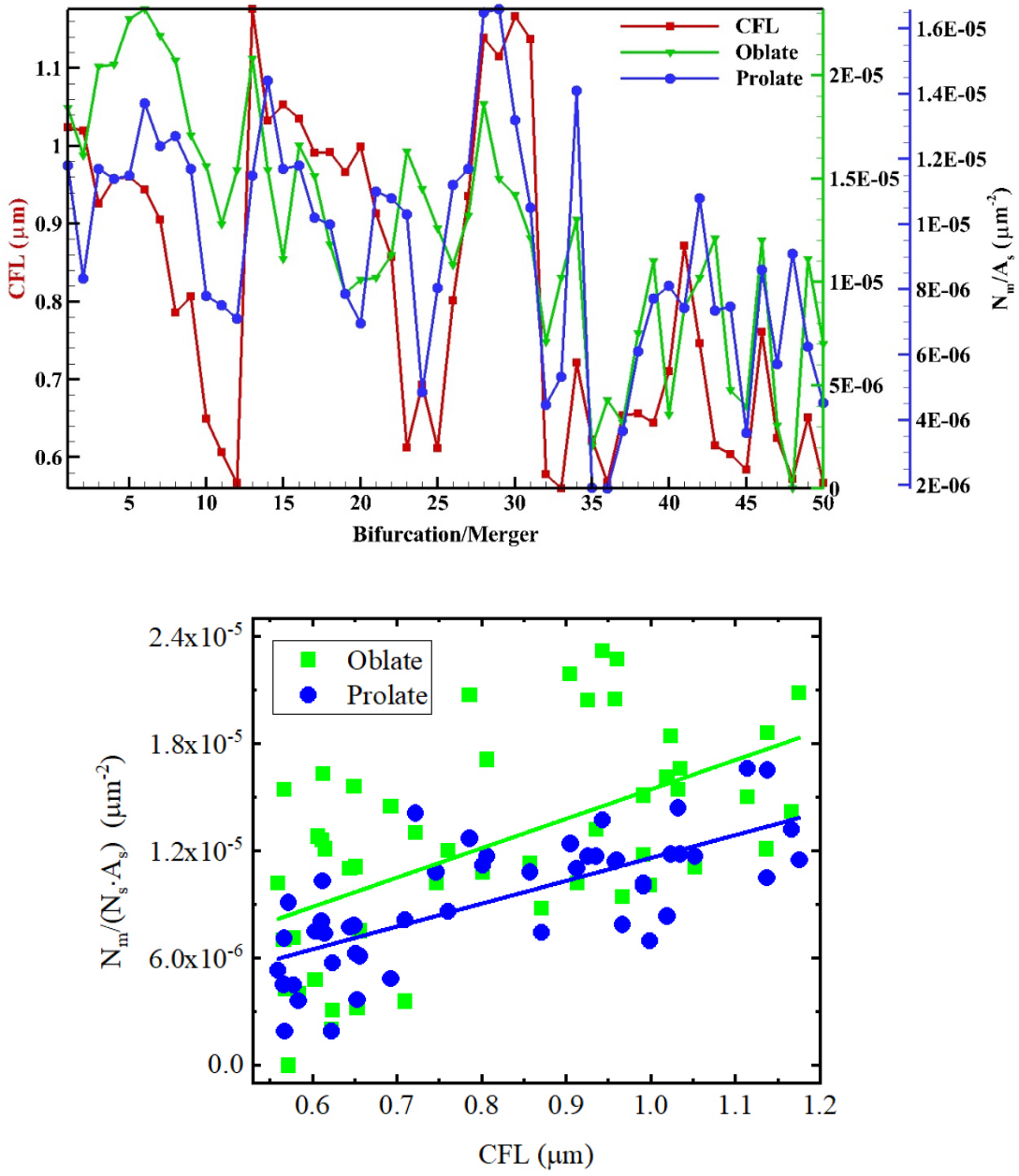

Figure 5.16: CFL thickness and area density of marginated NPs (N_m/A_s) are shown for different bifurcation and merger segments for Network A (top). Also shown CFL thickness versus N_m/A_s for the same network (bottom). The straight line is a linear fit through the data. Oblate (green square), and prolate (blue circle).

Now, we consider the heterogeneity of NPs accumulation in different generations (hierarchy) of segments. Figures 5.17 to 5.19 show the surface area density of marginated NPs for networks C, B, and A, respectively. NP accumulation increases with increasing generation number as in network C (network D behaves similarly). However, larger and more complicated geometries have a different behavior of heterogeneity. In networks A and B, higher margination exists at the mid-levels and less at the beginning and end levels. All NP sizes behave similarly in a specific geometry. Also, zero hematocrit simulations show similar behaviors of distribution among segment hierarchy of Ht = 25% (not shown). Therefore, we conclude that this kind of heterogeneity is due to the geometry configuration itself.

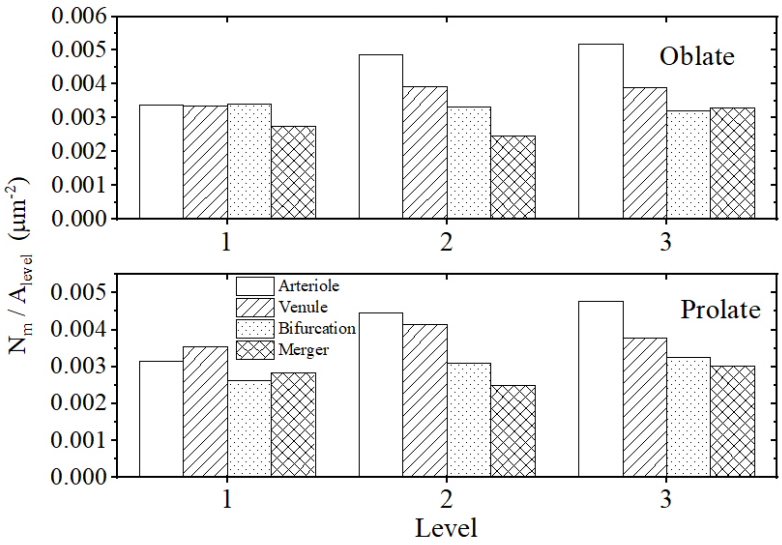

Figure 5.17: NP margination accumulation for Ht = 25% (per unit surface area for each segment group) presented as a function of segment generation level for network C.

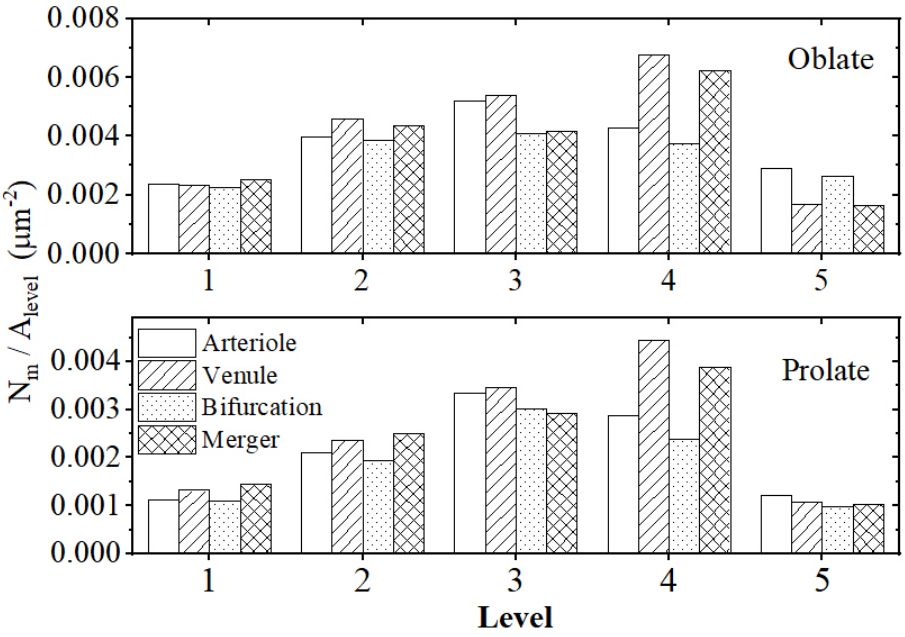

Figure 5.18: NP margination for Ht = 25% (per unit surface area for each segment group) presented as a function of segment generation level for network B.

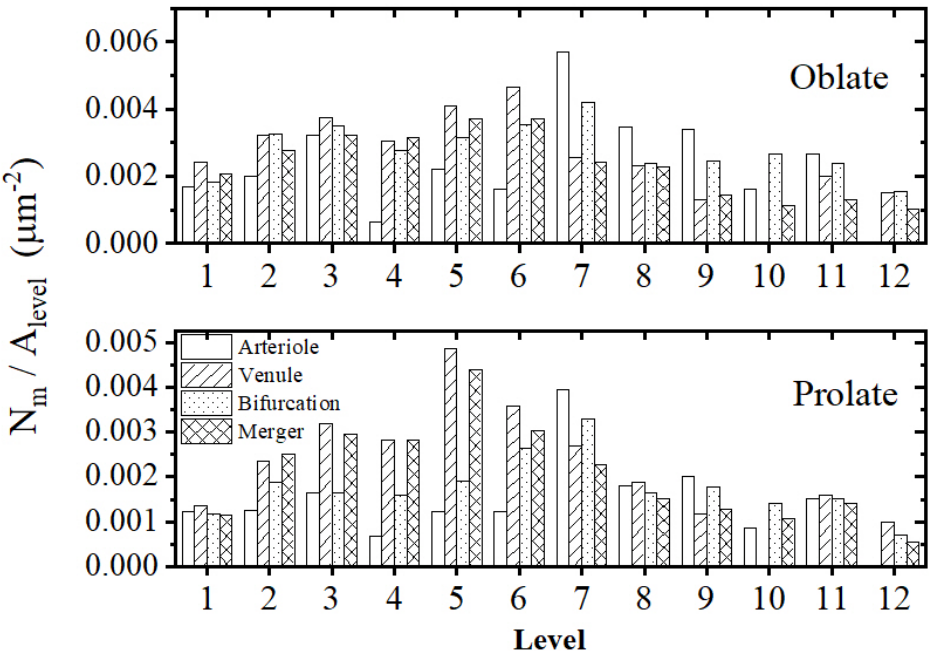

Figure 5.19: NP margination for Ht = 25% (per unit surface area for each segment group) presented as a function of segment generation level for network A.

5.2.3.2 Adhesion likelihood analysis

Next, we show that the heterogeneity within generations of a segment for finite size ellipsoidal particles is also presents in the adhesion results. Figure 5.20 shows the adhesion likelihood of both ellipsoidal shapes (based on area density). Figure 5.21 and figure 5.22 show the heterogeneity among levels in networks C and A respectively. Also, as we see in the margination analysis, the adhesion likelihood increases with increasing number of levels for network C of the less complicated direction of flow, while middle levels have higher adhesion likelihood for more complicated geometries as in network A.

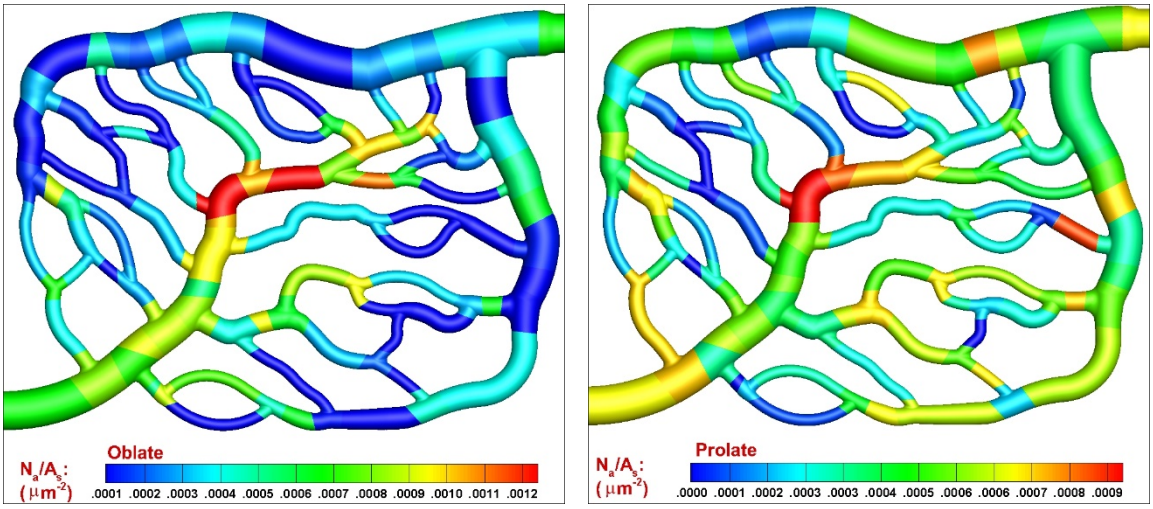

Figure 5.20: Contours of adhesion likelihood area density (N_a/A_s) in each segment in network A for both oblate and prolate ellipsoidal particles (Ht = 25%).

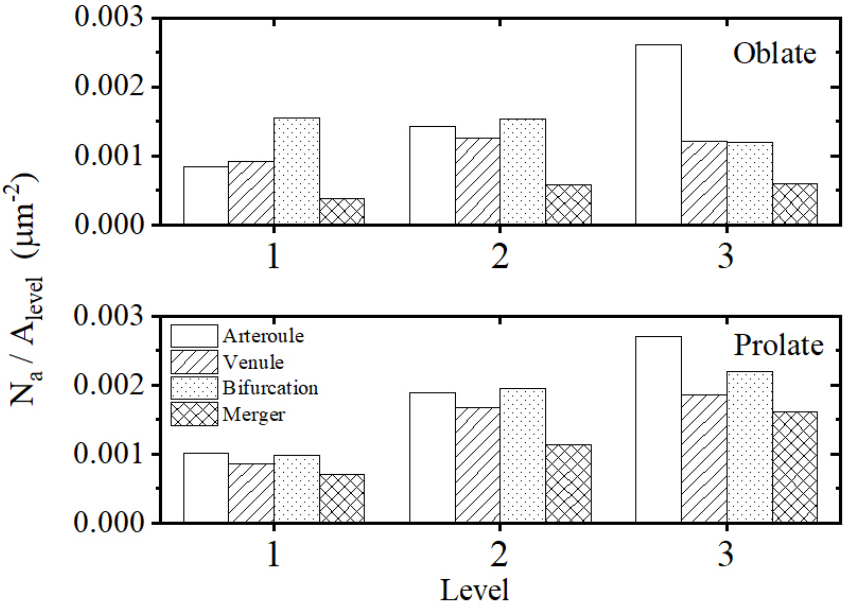

Figure 5.21: Accumulation for Ht = 25% (per unit surface area for each segment group) for likely adhered ellipsoidal NPs presented as a function of segment generation level for network C.

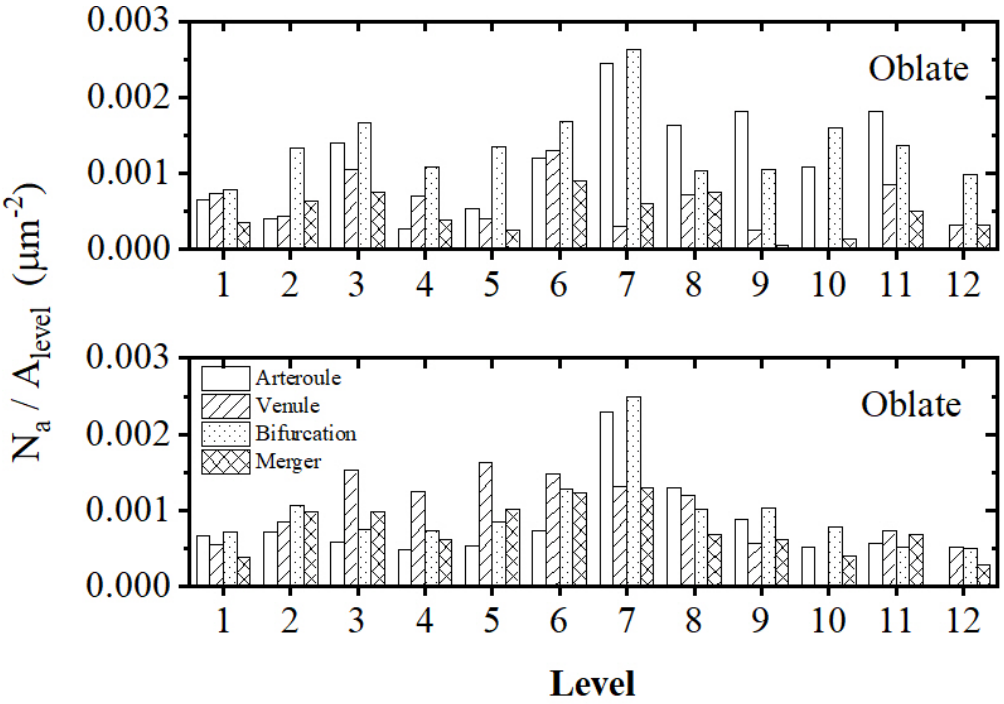

Figure 5.22: Accumulation for Ht = 25% (per unit surface area for each segment group) for likely adhered ellipsoidal NPs presented as a function of segment generation level for network A.

5.3 Conclusions

Transport, margination, and adhesion likelihood of nanoparticles modeled as finite size rigid ellipsoids (oblate and prolate) are simulated in physiologically realistic microvascular networks with fully resolved flow dynamics of red blood cells. These particles are in two-way interaction with the flow field, boundaries, and RBCs. A particle is considered to be marginated when it has a surface portion or all of its body within the RBC-free layer. It is however, allowed to move by the flow and can get out of the CFL. On the other hand, the particle is considered to be able to start adhesion if it comes within 650 nm from the vessel walls.

Similar to tracer and finite size spherical particles, heterogeneity persists among various networks. For both margination and adhesion likelihood, the arteriolar and venular segments have the highest accumulation and the capillaries the lowest. Margination is observed even when there are no RBCs. RBCs' presence enhances the margination levels by about one order of magnitude. Even within each type of vascular segments, a strong heterogeneity is observed. The dependence of margination and adhesion likelihood of ellipsoidal particles within these microvascular networks is strongly correlated to the CFL thickness. The distribution of marginated NPs and their adhesion likelihood throughout the generations of the various network segments have two different behaviors similar to what we found in varied size study in chapter four. In simple networks C and D, the accumulation increases with generation, while the accumulation in more complicated networks A and B is observed in the middle generations of a segment.

Irrespective to network configuration and hematocrit level, the accumulation of the ellipsoidal particles and the likelihood of adhesion are higher than their equivalent size

spherical particles. Oblate particles show the highest margination and adhesion likelihood compared to the prolate and spherical ones. Finally, irrespective to the effect of the geometry, the ellipsoidal particles have the potential to be uniformly distributed among various segments of a microvascular network.

Chapter 6

Conclusions and Future Work

6.1 Conclusions

Targeted delivery of therapeutic drugs to specific sites in the body is becoming a norm for treating many diseases, such as cancer. The main tool in targeted delivery is the nano-carriers (NCs) which have to deliver the therapeutic drug to the diseased sites through the blood circulation. During their journey, these NCs face several challenges to overcome in order to function efficiently. Therefore, these particles need to be engineered to be able to function in the way they are designed for.

Studies done to improve NCs' performance consider several characteristics of the particles; namely, size, shape, surface charge and biochemical characteristics, density, and rigidity. Size and shape have been found to be very effective parameters to control to improve these particles' non-active targeting. These properties are required to improve specific processes associated with targeting, namely, dispersion, margination, adhesion, and absorption.

In this work, we investigated the most dominating phenomena (margination and adhesion) which influence the transport of the NCs within physiologically-realistic microvascular networks. This is motivated by previous studies which have focused on such phenomena in simple geometries like tubes, channels, and at most, one bifurcation

and merger. On the other hand, the vascular networks are characterized by highly tortuous vessels, and frequent and hierarchical bifurcations and mergers.

In this thesis, we utilize a high-fidelity computational model of cellular-scale blood flow in physiologically-realistic microvascular networks to understand the simultaneous effects of the flowing red blood cells, complex geometry of the vasculatures, together with the particle size and shape on the margination and adhesion behaviors.

In the first part of the work, chapter three, we modeled nanoparticles as volume-less fluid particles that are simply advected by the fluid streamlines. In chapter four, we investigated the effect of the finite size of spherical particles. In chapter five, we investigated the effect of the shape considering two ellipsoidal shapes: oblate and prolate. We summarize conclusions of these studies below.

1. **Tracer particle simulation:** The results of tracer particles simulation show that the NP distribution is highly non-uniform across a network for both margination and adhesion. Specifically, for the adhesion simulations, the bifurcation regions show a significantly enhanced NP accumulation. In contrast, for the margination simulations, the venular segments show the highest accumulation. The heterogeneity also exists within each vascular segments generation. In general, the area density of the adhered NPs is observed to correlate with the segment hematocrit. As for the margination, NP accumulation is shown to correlate with the CFL thickness. Specifically, at the bifurcations, the dynamics of the RBCs as they flow intermittently in clusters is shown to enhance the adhesion.

2. **Finite-size spherical particles simulations:** The heterogeneity of margination and adhesion likelihood of finite sized spherical particles also persists in various segments of a network. For both margination and adhesion likelihood, the arteriolar and venular segments exhibit the highest accumulation and the capillaries show the lowest. Similar to tracer results, heterogeneity within each type of vascular segments is also observed for both margination and adhesion likelihood. Using the area density of the marginated NPs, accumulation is shown to correlate with the CFL thickness as is the case for the tracer particles. This also holds for the adhesion likelihood. Our simulations show that irrespective of hematocrit levels and network topology, the accumulation of the marginated particles and the likelihood of adhesion increase with increasing particle size; as such, the biggest diameter studied here, 2.0 μm, shows the most efficient margination and adhesion likelihood behaviors compared to the smaller sizes.

3. **Ellipsoidal particles simulations:** Similar to tracer and spherical particles, heterogeneity of margination and adhesion likelihood persists among various networks for ellipsoidal particles. For both margination and adhesion likelihood, the arteriolar and venular segments have the highest accumulation, and the capillaries have the lowest. Margination and adhesion likelihood of ellipsoidal particles within the studied microvascular networks are strongly correlated to the CFL thickness. Our simulations show that within all geometries, hematocrit levels, the accumulation of the ellipsoidal particles is higher that the equivalent spherical particle. The oblate-

shaped particles show the best efficient margination and adhesion likelihood behaviors over all other studied particles.

4. **Network geometry effect:** Margination and adhesion/likelihood is observed even when there are no RBCs for all of our simulations. This indicates the importance of the network configuration on the margination and adhesion phenomena. This is not the case in straight tube geometry where RBCs push them closer to the wall.

5. **Advantages and shortcoming of tracer particles simulations to predict NPs margination and adhesion behaviors:** Tracer particle simulations can give a good prediction of the NPs margination and its heterogeneity within all microvascular network segments and their generations. Also, they can efficiently predict the Ht effect on the margination and adhesion. Moreover, these simulations can predict that CFL thickness for the margination process and Ht for the adhesion process ar correlated to particle accumulation. On the other hand, tracer particles simulations cannot specify exactly the levels of margination and adhesion within network segments, nor find the effect of size and shape of the particles on their margination and adhesion for sizes > 500 nm. Additionally, tracer particles simulations cannot predict train-cart mechanism associated with the rigid particles, and the mechanism of ellipsoidal particle rolling over the wall of the geometry within the CFL.

6.2 Recommendations for the future work

1. **Geometry effect:** Still there are some questions related to the network geometry and topology which need to be answered to understand the full role of the Network geometry on drug delivery. We need to understand how the network segments curvature and size influence the margination and adhesion mechanisms. Also, how the angles of mother and daughter segments at the bifurcation/merger affect these mechanisms. Moreover, as presented in chapter one, there are various configurations of microvascular networks e.g. treelike configurations in kidney and retina, and planar networks in muscles. In this work, we considered planar type networks; therefore, it is necessary to implement similar analysis on three dimensional and tree-like configurations to fully understand the role of geometry.

2. **Other particle characteristics:** Particle deformability and density: as we mentioned in chapter one, deformable particles have higher circulation time but are less efficient in margination. The margination of these particles is strongly dependent on Ht and shear rate near the wall. However, there is still a lack of understanding of their margination and adhesion mechanisms within full microvascular networks. The density of the particles is another parameter that needs to be investigated.

3. **Particle adhesion:** Finally, more accurate model is needed for adhesion process. Close to the wall, molecular forces like Van der Waals attractive force, Electrostatic Double-Layer Interaction, and Steric Repulsive Interaction start to be influential within 50 nm. In addition, the Brownian motion will affect the closeness from the

wall and amount of detachment of ligand-receptor bounds. All these forces added together with the hydrodynamic forces will decide the ligand-receptor bond formation between a particle surface and the surface of the vascular wall.

Bibliography

1. De Jong, W.H. and P.J. Borm, *Drug delivery and nanoparticles:applications and hazards.* Int J Nanomedicine, 2008. **3**(2): p. 133-49.
2. Tan, J., A. Thomas, and Y. Liu, *Influence of Red Blood Cells on Nanoparticle Targeted Delivery in Microcirculation.* Soft Matter, 2011. **8**: p. 1934-1946.
3. Ayyaswamy, P.S., V. Muzykantov, D.M. Eckmann, and R. Radhakrishnan, *Nanocarrier Hydrodynamics and Binding in Targeted Drug Delivery: Challenges in Numerical Modeling and Experimental Validation.* J Nanotechnol Eng Med, 2013. **4**(1): p. 101011-1010115.
4. Sobczynski, D.J., M.B. Fish, C.A. Fromen, M. Carasco-Teja, R.M. Coleman, and O. Eniola-Adefeso, *Drug carrier interaction with blood: a critical aspect for high-efficient vascular-targeted drug delivery systems.* Ther Deliv, 2015. **6**(8): p. 915-34.
5. Li, Y., W. Stroberg, T.-R. Lee, H.S. Kim, H. Man, D. Ho, P. Decuzzi, and W.K. Liu, *Multiscale modeling and uncertainty quantification in nanoparticle-mediated drug/gene delivery.* Computational Mechanics, 2013. **53**(3): p. 511-537.
6. Alexis, F., E.M. Pridgen, R. Langer, and O.C. Farokhzad, *Nanoparticle technologies for cancer therapy.* Handb Exp Pharmacol, 2010(197): p. 55-86.
7. Friedmann, T., J.C. Dunlap, and S.F. Goodwin, *Advances in genetics. Volume 69*. First edition. ed. Advances in genetics,. 2010: Elsevier/Academic Press. 160 pages.

8. Sakamoto, J.H., A.L. van de Ven, B. Godin, E. Blanco, R.E. Serda, A. Grattoni, A. Ziemys, A. Bouamrani, T. Hu, S.I. Ranganathan, E. De Rosa, J.O. Martinez, C.A. Smid, R.M. Buchanan, S.Y. Lee, S. Srinivasan, M. Landry, A. Meyn, E. Tasciotti, X. Liu, P. Decuzzi, and M. Ferrari, *Enabling individualized therapy through nanotechnology.* Pharmacol Res, 2010. **62**(2): p. 57-89.

9. Bao, G., Y. Bazilevs, J.H. Chung, P. Decuzzi, H.D. Espinosa, M. Ferrari, H. Gao, S.S. Hossain, T.J. Hughes, R.D. Kamm, W.K. Liu, A. Marsden, and B. Schrefler, *USNCTAM perspectives on mechanics in medicine.* J R Soc Interface, 2014. **11**(97): p. 20140301.

10. Wang, A.Z., R. Langer, and O.C. Farokhzad, *Nanoparticle delivery of cancer drugs.* Annu Rev Med, 2012. **63**: p. 185-98.

11. Thakor, A.S. and S.S. Gambhir, *Nanooncology: the future of cancer diagnosis and therapy.* CA Cancer J Clin, 2013. **63**(6): p. 395-418.

12. Wilczewska, A.Z., K. Niemirowicz, K.H. Markiewicz, and H. Car, *Nanoparticles as drug delivery systems.* Pharmacological Reports, 2012. **64**(5): p. 1020-1037.

13. Waite, L. and J.M. Fine, *Applied biofluid mechanics*. 2007, New York: McGraw-Hill. xv, 314 p.

14. Zienkiewicz, O.C. and R.N. Taylor, P., *Biofluid Dynamics*. 2014, Swansea University, SWansea: Perumal Nithiarasu, Swansea University. 100.

15. Thiriet, M., *Biology and Mechanics of Blood Flows*. 1 ed. Vol. Part II: Mechanics and Medical Aspects. 2003, New York: Springer-Verlag New York. XII, 468.

16. Chandran, K.B., S.E. Rittgers, and A.P. Yoganathan, *Biofluid Mechanics: The Human Circulation*. 1 ed. 2007, Boca Raton: CRC/Taylor & Francis. 419.

17. Mazumdar, J., *Biofluid mechanics*. 2nd ed. 2016, New Jersey: World Scientific. xvi, 247.

18. Fung, Y.C., *Biomechanics: Mechanical Properties of Living Tissues*. 1993, New York: Springer-Verlag New York. XVIII, 568.

19. Humphrey, J.D. and S.L. O'Rourke, *An Introduction to Biomechanics: Solids and Fluids, Analysis and Design*. 2nd ed. 2015, New York: Springer-Verlag New York. XXVI, 692.

20. Caro, C., T. Pedley, R. Schroter, W. Seed, and K. Parker, *The Mechanics of the Circulation*. 2nd ed. 2011, Cambridge: Cambridge University Press. xiii, 523.

21. Thiriet, M., *Biology and mechanics of blood flows*. 1st ed. CRM series in mathematical physics. 2008, New York: Springer-Verlag New York. XIV, 658.

22. Ethier, C. and C. Simmons, *Introductory Biomechanics: From Cells to Organisms*. Cambridge Texts in Biomedical Engineering. 2007, Cambridge: Cambridge University Press.

23. Carboni, E., K. Tschudi, J. Nam, X. Lu, and A.W. Ma, *Particle margination and its implications on intravenous anticancer drug delivery.* AAPS PharmSciTech, 2014. **15**(3): p. 762-71.

24. Li, Y., Y. Lian, L.T. Zhang, S.M. Aldousari, H.S. Hedia, S.A. Asiri, and W.K. Liu, *Cell and nanoparticle transport in tumour microvasculature: the role of size, shape and surface functionality of nanoparticles.* Interface Focus, 2016. **6**(1): p. 20150086.

25. Muller, K., D.A. Fedosov, and G. Gompper, *Margination of micro- and nano-particles in blood flow and its effect on drug delivery.* Sci Rep, 2014. **4**: p. 4871.

26. Decuzzi, P., F. Gentile, A. Granaldi, A. Curcio, F. Causa, C. Indolfi, P. Netti, and M. Ferrari, *Flow chamber analysis of size effects in the adhesion of spherical particles.* Int J Nanomedicine, 2007. **2**(4): p. 689-96.

27. Decuzzi, P., B. Godin, T. Tanaka, S.Y. Lee, C. Chiappini, X. Liu, and M. Ferrari, *Size and shape effects in the biodistribution of intravascularly injected particles.* J Control Release, 2010. **141**(3): p. 320-7.

28. Lee, T.R., M. Choi, A.M. Kopacz, S.H. Yun, W.K. Liu, and P. Decuzzi, *On the near-wall accumulation of injectable particles in the microcirculation: smaller is not better.* Sci Rep, 2013. **3**: p. 2079.

29. Charoenphol, P., R.B. Huang, and O. Eniola-Adefeso, *Potential role of size and hemodynamics in the efficacy of vascular-targeted spherical drug carriers.* Biomaterials, 2010. **31**(6): p. 1392-402.

30. Li, Y., X. Zhang, and D. Cao, *Nanoparticle hardness controls the internalization pathway for drug delivery.* Nanoscale, 2015. **7**(6): p. 2758-69.

31. Muller, K., D.A. Fedosov, and G. Gompper, *Understanding particle margination in blood flow - A step toward optimized drug delivery systems.* Med Eng Phys, 2016. **38**(1): p. 2-10.

32. de Tullio, M.D., J. Singh, G. Pascazio, and P. Decuzzi, *Predicting the size-dependent tissue accumulation of agents released from vascular targeted nanoconstructs.* Computational Mechanics, 2013. **53**(3): p. 437-447.

33. Thomas, A., J. Tan, and Y. Liu, *Characterization of nanoparticle delivery in microcirculation using a microfluidic device.* Microvasc Res, 2014. **94**: p. 17-27.

34. Eckstein, E.C., A.W. Tilles, and F.J. Millero, 3rd, *Conditions for the occurrence of large near-wall excesses of small particles during blood flow.* Microvasc Res, 1988. **36**(1): p. 31-9.

35. D'Apolito, R., G. Tomaiuolo, F. Taraballi, S. Minardi, D. Kirui, X. Liu, A. Cevenini, R. Palomba, M. Ferrari, F. Salvatore, E. Tasciotti, and S. Guido, *Red blood cells affect the margination of microparticles in synthetic microcapillaries and intravital microcirculation as a function of their size and shape.* J Control Release, 2015. **217**: p. 263-72.

36. Muro, S., C. Garnacho, J.A. Champion, J. Leferovich, C. Gajewski, E.H. Schuchman, S. Mitragotri, and V.R. Muzykantov, *Control of endothelial targeting and intracellular delivery of therapeutic enzymes by modulating the size and shape of ICAM-1-targeted carriers.* Mol Ther, 2008. **16**(8): p. 1450-8.

37. Toy, R., P.M. Peiris, K.B. Ghaghada, and E. Karathanasis, *Shaping cancer nanomedicine: the effect of particle shape on the in vivo journey of nanoparticles.* Nanomedicine (Lond), 2014. **9**(1): p. 121-34.

38. Blanco, E., H. Shen, and M. Ferrari, *Principles of nanoparticle design for overcoming biological barriers to drug delivery.* Nature Biotechnology, 2015. **33**(9): p. 941-951.

39. Godin, B., C. Chiappini, S. Srinivasan, J.F. Alexander, K. Yokoi, M. Ferrari, P. Decuzzi, and X. Liu, *Discoidal Porous Silicon Particles: Fabrication and Biodistribution in Breast Cancer Bearing Mice.* Adv Funct Mater, 2012. **22**(20): p. 4225-4235.

40. Lee, S.Y., M. Ferrari, and P. Decuzzi, *Shaping nano-/micro-particles for enhanced vascular interaction in laminar flows.* Nanotechnology, 2009. **20**(49): p. 495101.

41. Lee, S.Y., M. Ferrari, and P. Decuzzi, *Design of bio-mimetic particles with enhanced vascular interaction.* J Biomech, 2009. **42**(12): p. 1885-90.

42. Toy, R., E. Hayden, C. Shoup, H. Baskaran, and E. Karathanasis, *The effects of particle size, density and shape on margination of nanoparticles in microcirculation.* Nanotechnology, 2011. **22**(11): p. 115101.

43. Gentile, F., C. Chiappini, D. Fine, R.C. Bhavane, M.S. Peluccio, M.M. Cheng, X. Liu, M. Ferrari, and P. Decuzzi, *The effect of shape on the margination dynamics of non-neutrally buoyant particles in two-dimensional shear flows.* J Biomech, 2008. **41**(10): p. 2312-8.

44. Decuzzi, P. and M. Ferrari, *The adhesive strength of non-spherical particles mediated by specific interactions.* Biomaterials, 2006. **27**(30): p. 5307-14.

45. Adriani, G., M.D. de Tullio, M. Ferrari, F. Hussain, G. Pascazio, X. Liu, and P. Decuzzi, *The preferential targeting of the diseased microvasculature by disk-like particles.* Biomaterials, 2012. **33**(22): p. 5504-13.

46. Thompson, A.J., E.M. Mastria, and O. Eniola-Adefeso, *The margination propensity of ellipsoidal micro/nanoparticles to the endothelium in human blood flow.* Biomaterials, 2013. **34**(23): p. 5863-71.

47. Doshi, N., B. Prabhakarpandian, A. Rea-Ramsey, K. Pant, S. Sundaram, and S. Mitragotri, *Flow and adhesion of drug carriers in blood vessels depend on their*

shape: a study using model synthetic microvascular networks. J Control Release, 2010. **146**(2): p. 196-200.

48. Tan, J., S. Shah, A. Thomas, H.D. Ou-Yang, and Y. Liu, *The influence of size, shape and vessel geometry on nanoparticle distribution.* Microfluid Nanofluidics, 2013. **14**(1-2): p. 77-87.

49. Shah, S., Y. Liu, W. Hu, and J. Gao, *Modeling particle shape-dependent dynamics in nanomedicine.* J Nanosci Nanotechnol, 2011. **11**(2): p. 919-28.

50. Venkataraman, S., J.L. Hedrick, Z.Y. Ong, C. Yang, P.L. Ee, P.T. Hammond, and Y.Y. Yang, *The effects of polymeric nanostructure shape on drug delivery.* Adv Drug Deliv Rev, 2011. **63**(14-15): p. 1228-46.

51. Alabrudzinski, S., M.L. Ekiel-Jezewska, D. Chehata-Gomez, and T.A. Kowalewski, *Particle clusters settling under gravity in a viscous fluid.* Physics of Fluids, 2009. **21**(7).

52. Anchordoquy, T.J., Y. Barenholz, D. Boraschi, M. Chorny, P. Decuzzi, M.A. Dobrovolskaia, Z.S. Farhangrazi, D. Farrell, A. Gabizon, H. Ghandehari, B. Godin, N.M. La-Beck, J. Ljubimova, S.M. Moghimi, L. Pagliaro, J.H. Park, D. Peer, E. Ruoslahti, N.J. Serkova, and D. Simberg, *Mechanisms and Barriers in Cancer Nanomedicine: Addressing Challenges, Looking for Solutions.* ACS Nano, 2017. **11**(1): p. 12-18.

53. Gentile, F., A. Curcio, C. Indolfi, M. Ferrari, and P. Decuzzi, *The margination propensity of spherical particles for vascular targeting in the microcirculation.* J Nanobiotechnology, 2008. **6**: p. 9.

54. Lamberti, G., Y. Tang, B. Prabhakarpandian, Y. Wang, K. Pant, M.F. Kiani, and B. Wang, *Adhesive interaction of functionalized particles and endothelium in idealized microvascular networks.* Microvasc Res, 2013. **89**: p. 107-14.

55. Sohrabi, S., J. Zheng, E.A. Finol, and Y. Liu, *Numerical simulation of particle transport and deposition in the pulmonary vasculature.* J Biomech Eng, 2014. **136**(12): p. 121010.

56. C. Bächer, L.S., and S. Gekle, *Antimargination of microparticles and platelets in the vicinity of branching vessels.* Biophys J, 2006. **91**(6): p. L66-8.

57. Prabhakarpandian, B., Y. Wang, A. Rea-Ramsey, S. Sundaram, M.F. Kiani, and K. Pant, *Bifurcations: focal points of particle adhesion in microvascular networks.* Microcirculation, 2011. **18**(5): p. 380-9.

58. Li, Y., Y. Song, L. Zhao, G. Gaidosh, A.M. Laties, and R. Wen, *Direct labeling and visualization of blood vessels with lipophilic carbocyanine dye DiI.* Nat Protoc, 2008. **3**(11): p. 1703-8.

59. Fung, Y.C., *Biomechanics: Circulation*. 2nd ed. 1997, New York: Springer-Verlag New York. XVIII, 572.

60. Fukumura, D., D.G. Duda, L.L. Munn, and R.K. Jain, *Tumor microvasculature and microenvironment: novel insights through intravital imaging in pre-clinical models.* Microcirculation, 2010. **17**(3): p. 206-25.

61. Lee, J.-S. and T.C. Skalak, *Microvascular Mechanics: Hemodynamics of Systemic and Pulmonary Microcirculation*. 1st ed. 1989, Springer-Verlag New York: Springer-Verlag New York Inc. XV, 222.

62. Mayerich, D., J. Kwon, C. Sung, L. Abbott, J. Keyser, and Y. Choe, *Fast macro-scale transmission imaging of microvascular networks using KESM.* Biomedical Optics Express, 2011. **2**(10): p. 2888-2896.

63. Secomb, T.W., R. Hsu, N.B. Beamer, and B.M. Coull, *Theoretical simulation of oxygen transport to brain by networks of microvessels: effects of oxygen supply and demand on tissue hypoxia.* Microcirculation, 2000. **7**(4): p. 237-47.

64. Sherwood, J.M., D. Holmes, E. Kaliviotis, and S. Balabani, *Spatial distributions of red blood cells significantly alter local haemodynamics.* PLoS One, 2014. **9**(6): p. e100473.

65. Pries, A.R., T.W. Secomb, T. Gessner, M.B. Sperandio, J.F. Gross, and P. Gaehtgens, *Resistance to blood flow in microvessels in vivo.* Circ Res, 1994. **75**(5): p. 904-15.

66. Kiani, M.F., A.R. Pries, L.L. Hsu, I.H. Sarelius, and G.R. Cokelet, *Fluctuations in microvascular blood flow parameters caused by hemodynamic mechanisms.* Am J Physiol, 1994. **266**(5 Pt 2): p. H1822-8.

67. Mollica, F., R.K. Jain, and P.A. Netti, *A model for temporal heterogeneities of tumor blood flow.* Microvasc Res, 2003. **65**(1): p. 56-60.

68. Davis, J.M. and C. Pozrikidis, *Numerical Simulation of Unsteady Blood Flow through Capillary Networks.* Bull Math Biol, 2011. **73**(8): p. 1857-80.

69. Geddes, J.B., R.T. Carr, N.J. Karst, and F. Wu, *The Onset of Oscillations in Microvascular Blood Flow.* SIAM Journal on Applied Dynamical Systems, 2007. **6**(4): p. 694-727.

70. Forouzan, O., X. Yang, J.M. Sosa, J.M. Burns, and S.S. Shevkoplyas, *Spontaneous oscillations of capillary blood flow in artificial microvascular networks.* Microvasc Res, 2012. **84**(2): p. 123-32.

71. Spagnolie, S.E., *Complex Fluids in Biological Systems: Experiment, Theory, and Computation*. 1st ed. 2015, New York: Springer-Verlag New York. XX, 440.

72. Hossain, S.S., T.J. Hughes, and P. Decuzzi, *Vascular deposition patterns for nanoparticles in an inflamed patient-specific arterial tree.* Biomech Model Mechanobiol, 2014. **13**(3): p. 585-97.

73. Hossain, S.S., Y.J. Zhang, X.H. Liang, F. Hussain, M. Ferrari, T.J.R. Hughes, and P. Decuzzi, *In silico vascular modeling for personalized nanoparticle delivery.* Nanomedicine, 2013. **8**(3): p. 343-357.

74. Zakrzewicz, A., T.W. Secomb, and A.R. Pries, *Angioadaptation: keeping the vascular system in shape.* News Physiol Sci, 2002. **17**: p. 197-201.

75. Benedict, K.F., G.S. Coffin, E.J. Barrett, and T.C. Skalak, *Hemodynamic systems analysis of capillary network remodeling during the progression of type 2 diabetes.* Microcirculation, 2011. **18**(1): p. 63-73.

76. Cassot, F., F. Lauwers, C. Fouard, S. Prohaska, and V. Lauwers-Cances, *A novel three-dimensional computer-assisted method for a quantitative study of microvascular networks of the human cerebral cortex.* Microcirculation, 2006. **13**(1): p. 1-18.

77. Lipowsky, H.H., S. Kovalcheck, and B.W. Zweifach, *The distribution of blood rheological parameters in the microvasculature of cat mesentery.* Circ Res, 1978. **43**(5): p. 738-49.

78. Christophe, G. and R. Jean-François, *Gmsh: A 3-D finite element mesh generator with built-in pre- and post-processing facilities.* International Journal for Numerical Methods in Engineering, 2009. **79**(11): p. 1309-1331.

79. Balogh, P. and P. Bagchi, *Direct Numerical Simulation of Cellular-Scale Blood Flow in 3D Microvascular Networks.* Biophys J, 2017. **113**(12): p. 2815-2826.

80. Ramanujan, S. and C. Pozrikidis, *Deformation of liquid capsules enclosed by elastic membranes in simple shear flow: large deformations and the effect of fluid viscosities.* Journal of Fluid Mechanics, 1998. **361**: p. 117-143.

81. Popinet, S., *GNU Triangulated Surface Library*. 2006.

82. Skalak, R., A. Tozeren, R.P. Zarda, and S. Chien, *Strain energy function of red blood cell membranes.* Biophys J, 1973. **13**(3): p. 245-64.

83. Helfrich, W., *Elastic properties of lipid bilayers: theory and possible experiments.* Z Naturforsch C, 1973. **28**(11): p. 693-703.

84. Charrier, J.M., S. Shrivastava, and R. Wu, *Free and Constrained Inflation of Elastic Membranes in Relation to Thermoforming - Non-Axisymmetric Problems.* Journal of Strain Analysis for Engineering Design, 1989. **24**(2): p. 55-74.

85. Shrivastava, S. and J. Tang, *Large Deformation Finite-Element Analysis of Nonlinear Viscoelastic Membranes with Reference to Thermoforming.* Journal of Strain Analysis for Engineering Design, 1993. **28**(1): p. 31-51.

86. Eggleton, C.D. and A.S. Popel, *Large deformation of red blood cell ghosts in a simple shear flow.* Physics of Fluids, 1998. **10**(8): p. 1834-1845.

87. Pozrikidis, C., *Numerical computation in science and engineering*. 2nd ed. Topics in chemical engineering. 2008, Oxford ; New York: Oxford University Press. xxii, 1251 p.

88. Balogh, P. and P. Bagchi, *A computational approach to modeling cellular-scale blood flow in complex geometry.* Journal of Computational Physics, 2017. **334**: p. 280-307.

89. Doddi, S.K. and P. Bagchi, *Effect of inertia on the hydrodynamic interaction between two liquid capsules in simple shear flow.* International Journal of Multiphase Flow, 2008. **34**(4): p. 375-392.

90. Doddi, S.K. and P. Bagchi, *Lateral migration of a capsule in a plane Poiseuille flow in a channel.* International Journal of Multiphase Flow, 2008. **34**(10): p. 966-986.

91. Doddi, S., *Three dimensional computational modeling and simulation of biological cells and capsules*, in *Mechanical and Aerospace Engineering Department*. 2008, Rutgers, The State University of New Jersey: ProQuest Dissertations Publishing.

92. Vahidkhah, K., *Three-dimensional computational simulation of multiscale multiphysics cellular/particulate processes in microcirculatory blood flow*, in *Mechanical and Aerospace Engineering*. 2015, Rutgers, The State University of New Jersey: ProQuest Dissertations Publishing.

93. Balogh, P. and P. Bagchi, *A computational approach to modeling cellular-scale blood flow in complex geometry.* Journal of Computational Physics, 2017. **334**: p. 280-307.

94. Allen, M.P. and D.J. Tildesley, *Computer simulation of liquids*. 2nd ed. 2017, Oxford, United Kingdom: Oxford University Press. xiv, 626.

95. Baruh, H., *Applied dynamics*. 2015, Boca Raton: CRC Press/Taylor & Frances Group. xxii, 850.

96. Shyy, W., *Computational modeling for fluid flow and interfacial transport*. Transport processes in engineering. 1994, Amsterdam ; New York: Elsevier. xvii, 504.

97. Knupp, P.M. and K. Salari, *Verification of computer codes in computational science and engineering*. Discrete mathematics and its applications. 2003, Boca Raton, Fla.: Chapman & Hall/CRC. 144.

98. Jeffery, G.B. and L.N.G. Filon, *The motion of ellipsoidal particles immersed in a viscous fluid.* Proceedings of the Royal Society of London. Series A, 1922. **102**(715): p. 161-179.

99. Ku, D.N., *Blood Flow in Arteries.* Annual Review of Fluid Mechanics, 1997. **29**(1): p. 399-434.

100. Squires, T.M. and S.R. Quake, *Microfluidics: Fluid physics at the nanoliter scale.* Reviews of Modern Physics, 2005. **77**(3): p. 977-1026.

101. Stickel, J.J. and R.L. Powell, *Fluid mechanics and rheology of dense suspensions.* Annual Review of Fluid Mechanics, 2005. **37**: p. 129-149.

102. Mueller, S., E.W. Llewellin, and H.M. Mader, *The rheology of suspensions of solid particles.* Proceedings of the Royal Society a-Mathematical Physical and Engineering Sciences, 2010. **466**(2116): p. 1201-1228.